CYCO AND SIR: NEW TOOLS FOR NUMERICAL AND EXPERIMENTAL STUDIES OF SPACE CHARGE EFFECTS IN THE ISOCHRONOUS REGIME

by

Eduard Pozdeyev

A DISSERTATION

Submitted to
Michigan State University
in partial fulfillment of the requirements
for the degree of

DOCTOR OF PHYLOSOPHY

Department of Physics and Astronomy

2003

ABSTRACT

CYCO AND SIR: NEW TOOLS FOR NUMERICAL AND EXPERIMENTAL STUDIES OF SPACE CHARGE EFFECTS IN THE ISOCHRONOUS REGIME

by

Eduard Pozdeyev

This dissertation describes two novel tools for numerical and experimental studies of space charge effects in the isochronous regime: the code CYCO and the Small Isochronous Ring (SIR).

CYCO is a multi-particle code capable of simulating intense beam in isochronous cyclotrons in an acceptably short period of time without using powerful multi-processor computers. While developing the code, we paid special attention to having realistic models: The code calculates trajectories of macro-particles in a three-dimensional calculated or measured magnetic field map, using the complete system of the equations of motion. It uses the particle-to-mesh method to calculate the space charge field of the beam.

When used for calculating the beam dynamics in the low energy part of the PSI Injector 2, CYCO yielded results similar to those predicted by the code PICN [1]. The code was used to simulate the beam dynamics in the SIR. We intend to validate the code, comparing the results of the simulations to the experimental results that

will be obtained later in the ring.

SIR is a small-scale, low energy isochronous ring. The ring provides a unique opportunity to perform accurate experiments on space charge effects that are difficult to conduct in large-scale accelerators because of resolution and power limitations imposed on beam diagnostics. The opportunity to do accurate measurements of beam parameters allows the ring to be used for code benchmarking. The results of the experiments will also have applications to isochronous cyclotrons and synchrotrons at the transition gamma.

The ring has been assembled and commissioned. The first experiments with the beam in the ring show that the ring parameters are close to the design values. The observed behavior of the 20 μA beam indicates a fast growth of the energy spread within the beam due to space charge effects. The corresponding growth of the radial beam size is similar to that predicted by CYCO.

ACKNOWLEDGMENTS

I would like to express my sincere gratitude to my thesis adviser **Felix Marti** for formulating the problem for my dissertation and for navigating me through the dissertation work. His broad experience and knowledge of many areas of science were extremely helpful. His energetic personality was inspirational. I would like also to mention his excellent personal qualities. Working with Felix was a pleasant and exciting experience.

I want to thank **Alberto Rodriguez** who worked with me on the ring. We spent many days and evenings together developing and assembling parts and systems of the project. SIR would have never existed if Alberto had not joined the project.

I would like to thank **Richard York**. The moral and financial support provided by Prof. York were vital to SIR. His help in critical moments has expedited the work on the project.

I would like to express my sincere gratitude to **Henry Blosser**, my first professor who I started working with when I came to MSU. He introduced me to the world of cyclotrons and their applications. I would like to thank Dr. **Mort Gordon**. Our frequent discussions at the initial stages of the my dissertation work were very helpful. He gave me an insight into the specifics of the space charge effects in isochronous cyclotrons.

I would like to thank **Renan Fontus**, **Roger Zink**, and **John Bierwagen** for designing parts of the SIR project and preparing drawings of the hardware. Their work was critical for the project. I would like also to thank **Don Lawton** for his

studied as an undergraduate student. They infected me with a passion for physics and mathematics. I would like to express my gratitude to the **personnel of the Lab 11 (VEPP-2M) of the Budker Institute of Nuclear Physics, Novosibirsk**. While working there from 1992 to 1997, I gained practical knowledge of accelerators. Skills gained in Novosibirsk helped me to design and develop the small isochronous ring.

I am thankful to my wife, **Dali Georgobiani**, for her love and support. Her understanding and care were so important to me in my work and every-day life.

I am eternally grateful to my parents for their love and care, for everything what they have done for me in my life.

TABLE OF CONTENTS

LIST OF TABLES

LIST OF FIGURES

Chapter 1

INTRODUCTION

In recent years, there has been an increased interest in space charge effects in isochronous cyclotrons. Inspired by the successful high-current operation of the Ring Cyclotron at PSI, several authors have proposed an isochronous cyclotron as a driver for a number of applications including radioactive waste transmutation, energy production with accelerator driven nuclear reactors, and generation of neutrons and other secondary particles [2],[3],[4]. Tentative designs of such a machine have a maximum beam energy of 1 GeV and a beam current of 10 mA, yielding a total beam power of 10 MW.

Successful operation of a 10 MW cyclotron would be impossible without a deep understanding of space charge effects in the isochronous regime. In this work we describe a code and a small isochronous ring that can be used to enhance our knowledge of the dynamics of intense beams in the isochronous regime.

1.1 Classification of space charge effects in isochronous cyclotrons

Space-charge effects in isochronous cyclotrons can be separated into two groups: incoherent transverse and coherent longitudinal-radial.

1.1.1 Incoherent transverse space charge effects

The transverse space charge force effectively decreases the transverse focusing and lowers the betatron tunes. The effect is dominant in the central region of cyclotrons, where beam energy is low and vertical focusing can be weak. The intensity limit is reached when the vertical size of the beam reaches the vertical aperture limit. The transverse space charge effect is less dangerous in separated-sector machines with external injection, where beam energy is higher and transverse focusing is stronger.

1.1.2 Coherent longitudinal-radial space charge effects

The energy-phase motion of particles within the beam vanishes in the isochronous regime. This leads to a fast growth of the energy spread within beam bunches. The effect was first mentioned by T. Welton in [5] and later studied in detail by M. Gordon [6] and W. Joho [7]. As shown by M. Gordon, the longitudinal space charge force induces a vortex motion in the beam. The vortex motion induces a tilt of the bunches within the beam and tends to destroy turn separation. This leads to beam losses and extraction deflector overheating and activation.

It is worth noting that the same vortex motion can limit the growth of the energy

spread and beam size if the bunches are short. As shown in S. Adam's simulations [1], the vortex motion deforms a single bunch in the PSI Injector II into a circular distribution within several turns. After the circular distribution has formed, it changes little afterwards. This result was later confirmed experimentally in the PSI Injector II [8].

1.2 CYCO: a realistic 3D code for simulation of dynamics of intense beams in isochronous cyclotrons

Analytical treatment of the space charge in isochronous cyclotrons is difficult because of the complicated shape of the beam and the vacuum chamber. Thus, one has to proceed using numerical and/or experimental methods. In this section, we describe the code CYCO that was developed for simulating the beam dynamics of intense beams in cyclotrons. The next section contains a description of SIR, a small storage ring, that can be used for experimental studies of space charge effects.

There are several programs available for space charge simulations in isochronous cyclotrons. The program LSC [9] is based on an approach proposed by M. Gordon in [6] and treats the longitudinal-radial space charge effect as a perturbation. The code simulates the energy-phase motion of beam particles. It ignores the betatron motion and assumes operation in a regime where transverse focusing is strong. The code calculates only the longitudinal component of the field and ignores the transverse components. To simplify the field calculation LSC ignores the radial turn structure of the beam and replaces the microscopic charge density by its average value for

a given radius. Because the code neglects both the radial component of the space charge force and the betatron motion, it cannot simulate the vortex motion within the beam. Therefore, the code accurately estimates the energy spread within a bunch for "low" and "intermediate" beam intensities, when the bunch tilt angle due to the space charge is small, and overestimates the energy spread for high beam intensity.

The program PICN [1] is suitable for space charge simulations in cyclotrons with strong vertical focusing. It treats the beam as a set of needles of a fixed height that move in the median plane. In calculating the space charge field the code simulates the effect of image charges induced on a vacuum chamber multiplying the field of each needle by a function that causes the field to decrease faster at large distances. PICN also simulates an effect of neighboring turns assuming periodicity in radial direction. In calculating particle trajectories the program uses a set of simplified equations and the smooth-acceleration approximation, omitting the effect of the phase compression which was described in [10], [11] and [12].

Approximations made in LSC and PICN increase the calculational speed but decrease the accuracy of the simulations and limit their range of applicability. To provide a more complete tool for space charge simulations, we have developed a new multi-particle, 3D Particle-in-Cell code. The code, named CYCO, is capable of simulating intense beams in isochronous cyclotrons in an acceptably short period of time without using powerful multi-processor computers. The code calculates particle trajectories in a realistic 3D field map, solving a full, unsimplified system of six equations of motion of an ion in a 3D electro-magnetic field. The code uses the

classical 4th order Runge-Kutta integration method to numerically solve the system. CYCO assumes an abrupt change of the particle energy at each gap crossing with the approximation of infinitely thin accelerating gaps. In addition to an energy change at each gap crossing, the program includes a radial impulse due to the RF magnetic field that is responsible for the effect of phase compression. The space charge field of the beam is calculated by a fast field solver developed by the author. The solver is based on Fast Fourier Transforms and convolution technique described in [13]. In calculating the space charge field, the program includes the field of bunches of neighboring turns.

It is worth noting that CYCO can be also used for simulation of single- and multi-particle dynamics in circular accelerators other than cyclotrons. For example, CYCO is suitable for simulations of the beam dynamics in a small synchrotron. The shape of the vacuum chamber and the RF acceleration system adopted in the program, both specific to cyclotrons, are the only factors that limit application of the code to other types of accelerators.

1.3   SIR: a Small Isochronous Ring for experimental studies of space charge effects in the isochronous regime

The Small Isochronous Ring (SIR) [14],[15] is a small-scale experiment that needs low beam intensities to simulate the dynamics of intense ion beams in large scale accelerators. It provides a unique opportunity to perform precise experiments on the effects of space charge that are difficult to conduct in large-scale accelerators because of power and timing limitations imposed on beam diagnostics as well as programmatic

demands. The two main objectives of the ring are the experimental study of space charge effects in the isochronous regime and the validation of multi-particle codes used for space charge simulations. The important experimental issues that can be addressed by the ring are the space charge induced vortex motion specific to the isochronous regime, the longitudinal break-up of long bunches, the formation of the self-consistent stable charge distribution by short bunches, and the formation of weak beam tails and beam halo. The results of the experiments will have applications to high-current isochronous cyclotrons and synchrotrons at the transition gamma. The possibility of accurate beam parameter measurements also allows SIR to be used as a tool for benchmarking of multi-particle codes used for space charge simulations.

The ring is designed to run low energy light-ion beams. This choice of beam parameters simplifies the ring design and minimizes the cost of the project. The low beam energy yields a low velocity of ions. Because the space charge effect scales as $1/\beta^3$ [19], only low intensity beam is required to reach the interesting space charge regime. The low particle velocity also relaxes the timing requirements on the diagnostics and on the injection-extraction system. The low beam energy allows us to use low-field magnetic elements of simple design.

The University of Maryland Electron Ring (UMER) group [16] plans to use a low energy electron beam to simulate space charge effects in large-scale high-intensity accelerators. Both rings SIR and UMER are designed for approximately the same beam energy range: tens of keV. However, the H_2^+ beam in SIR is approximately 60 times slower than the electron beam of the same energy in UMER. This allows us to

use less expensive diagnostics to measure the longitudinal beam distribution with a high spacial resolution. The magnetic rigidity of the ion beam is 60 times larger than that of the electron beam of the same energy. This makes the ion beam significantly less sensitive to stray magnetic fields and virtually eliminates the problem of the earth magnetic field.

SIR consists of four 90°, flat-field magnets with edge focusing. The edge focusing provides both the vertical focusing and the isochronism in the ring. Figure 1.1 shows a schematic view of SIR. Table 1.1 gives the main parameters of the ring. An H_2^+ or deuteron beam is produced by a multi-cusp ion source, that can be biased up to 30 kV. An analyzing magnet located under the ion source provides charge-to-mass state selection and steers the beam towards the ring. The selected beam is chopped by a chopper and matched to the ring by a triplet of electrostatic quadrupoles in the injection line. The bunch length can be changed from 100 nanoseconds to 4 microseconds. and beam current varied from 0 to several hundred microamperes. The beam is injected into the ring with a help of a fast pulsed electrostatic inflector. After injection, the bunch coasts in the ring. After a chosen number of turns, the bunch is deflected towards a Fast coaxial Faraday Cup (FFC). The Faraday Cup measures the longitudinal beam profile of the beam with a time resolution of 1 ns corresponding to a spatial resolution of 1.5 mm for 20 keV deuterons and H_2^+ and 2 mm for H^+. Using this procedure, we can take "snapshots" of the longitudinal beam profile after a different number of turns. Analysis of the data will provide better insight in space charge effects in the isochronous regime. A more detailed description

7

of SIR and its subsystems can be found in Chapter 4.

From simulations presented in Section 3.1.3, a 23 keV, 100 μA deuteron beam has a Laslett tune shift of approximately 0.2-0.23 (20%). For comparison, the tune shift is approximately 0.04 (3%) in the injection region of PSI Injector II and will be approximately 0.15 (3%) in the SNS ring. (For more details on the scaling law for the Laslett tune shift in isochronous cyclotrons see Appendix A).

Because SIR operates in the isochronous regime, the longitudinal perviance and other values related to the longitudinal focusing are not appropriate metrics for comparison of longitudinal space charge effects. In this instance, a better measure is the rate of the vortex motion induced by the longitudinal and radial components of the space charge force.

As shown in Appendix A the particle radius changes under the influence of the longitudinal space charge force with a rate given by

$$\frac{dx}{d\theta} = 2\pi g_{\parallel} \frac{qI}{\gamma^5 m h \omega^3} \tag{1.1}$$

where θ is the generalized azimuth angle, q and m are the particle charge and mass respectively, γ is the relativistic factor, h is the RF harmonic number, ω is rotational angular frequency, and I is the beam current. The geometrical factor, $g_{\parallel}$, is a function of the beam shape, charge distribution, and position of the particle in the beam.

The transverse component of the space charge force breaks the condition of the isochronism and causes the particle to slip longitudinally with a rate of

Plan view

1 meter

Q

Q

FFC

Deflector

D

Q

Inflector

Chopper

D

Ion Source

Q

Quadrupole
Triplet

Mass-state
separator magnet

Side view
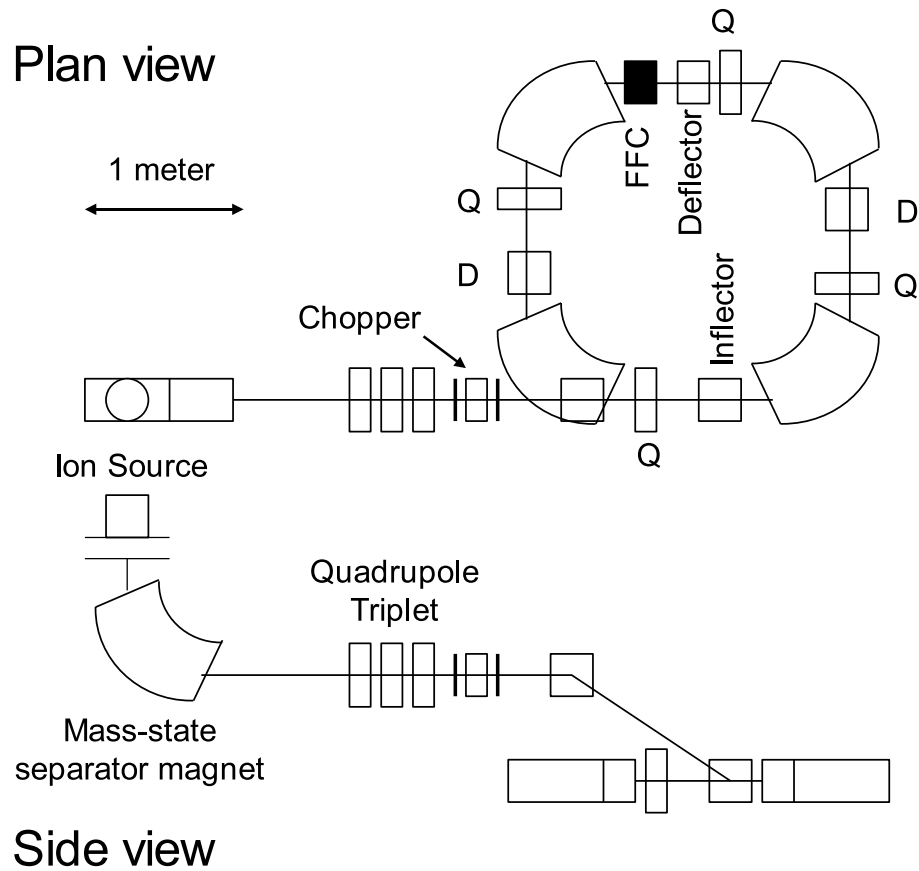
Figure 1.1: A schematic view of the SIR project

Table 1.1: Main beam and machine parameters

Particles	H^+, H_2^+ or deuterons
Energy	0-30 keV
Peak beam current	100 μA
Max.Magnetic field	800 Gauss
Injection-extraction	Pulsed electrostatic kickers
Diagnostics	Fast Faraday cup
Circumference	6.58 m

$$\frac{ds}{d\theta} = 2\pi g_\perp \frac{qI}{\gamma^3 \nu^2 m h \omega^3} \tag{1.2}$$

where ν is the radial betatron tune, and $g_\perp$ is a geometrical factor depending on the beam shape, charge distribution and position of the particle in the beam. For isochronous cyclotrons, the radial betatron tune is approximately equal to the relativistic factor γ. Substituting γ for ν we obtain

$$\frac{ds}{d\theta} \approx 2\pi g_\perp \frac{qI}{\gamma^5 m h \omega^3} \tag{1.3}$$

As one can see from Equations 1.1 and 1.3, the vortex motion depends on the beam shape and the ratio

$$\frac{qI}{\gamma^5 m h \omega^3} \tag{1.4}$$

It weakly depends on the machine optics and geometry. Thus, two bunches similar in shape in two different cyclotrons behave alike (per turn) if expression 1.4 yields the same value for both bunches. The Laslett tune shift will also be the same for both bunches.

The peak beam current can be written as

$$\hat{I} = \frac{I}{h} \frac{2\pi R}{\delta l} \tag{1.5}$$

where R is the average radius of the beam trajectory, h is the harmonic number, δl is the bunch effective length, and I is total beam current.

The ratio of peak current in two different machines will be

$$\frac{\hat{I}_2}{\hat{I}_1} = \frac{I_2 h_1}{I_1 h_2} \frac{R_2}{R_1} \tag{1.6}$$

where symbols 1 and 2 distinguish parameters related to different cyclotrons. Using Equation 1.4 we can rewrite Equation 1.6 as

$$\frac{\hat{I}_2}{\hat{I}_1} = \left(\frac{\gamma_2}{\gamma_1}\right)^5 \frac{q_1 m_2}{q_2 m_1} \left(\frac{\omega_2}{\omega_1}\right)^3 \frac{R_2}{R_1} \tag{1.7}$$

Plugging in numbers for a 20 keV deuteron beam in SIR and the proton beam in the injection region of PSI Injector II, we find that

$$\frac{\hat{I}_{Inj.2}}{\hat{I}_{SIR}} = 2.3 \cdot 10^3; \tag{1.8}$$

Thus, a peak current of 100 μA in SIR is equivalent to 230 mA peak current in the injection region of PSI Injector II. Assuming that the bunch length, δl, in the Injector II is 1.5 cm and the average radius of the trajectory, R, is 0.41 m we find that a peak current of 230 mA corresponds to a total current of

$$I_{Inj.2} = \hat{I}_{Inj.2} \frac{\delta l \, h}{2\pi R} = 13.5 \text{mA} \tag{1.9}$$

This current exceeds the maximum accelerated current in PSI Injector II by a factor of approximately 7. For the last few turns in PSI Injector II, the equivalent total current increases to 19.4 mA.

1.4 A short description of contents of the following chapters

In the second chapter of this dissertation, we describe the multi-particle code CYCO. We also give details of the particle tracking in the code and describe the space charge field solver. This chapter also contains some details of the code structure.

Chapters 3, 4, and 5 describe the Small Isochronous Ring project that was developed at NSCL. Chapter 3 presents results of analytical estimates and simulations of the beam dynamics in the ring. The first section of the third chapter contains results obtained within the hard-edge approximation used for the dipole magnets of the ring. The second section of the chapter describes the POISSON and TOSCA models used to calculate the magnetic field of the ring dipoles. It also presents results of beam dynamics simulations in the 3D field map generated by TOSCA.

Chapter 4 contains description of ring subsystems: dipole magnets, steering and quadrupole correctors, injection-extraction system, diagnostics, and vacuum system. It also presents results of measurements of the magnetic field of the ring dipoles.

Chapter 5 describes the first experiments with the beam in the ring. It presents results of measurement of the betatron frequencies and beam life time. The chapter also describes experiments with the 20 μA H_2^+ beam that indicate a fast energy growth within the beam due to the space charge effects.

Chapter 2

CYCO

2.1 Tracking particles

2.1.1 Macro-particles

The code uses macro-particles to simulate behavior of intense beams in accelerators. In an ideal case, the number of macro-particles in the program would be equal to the number of particles in the beam. The charge of the macro-particles in the program, in this case, would be equal to the charge of the particles in the beam. The average number of particles in each bunch of the beam can reach 10^9 in high intensity cyclotrons. Simulation of the collective dynamics of this large number of particles is very difficult even in the most powerful modern computers because of enormous number of calculations and computer memory requirements. A solution is to decrease the number of particles and increase their charge proportionally, leaving the total charge of each bunch the same. The maximum number of macro-particles in CYCO is limited by the available computer memory. If we limit the choice of computers to modern PCs or single-processor workstations and limit the computation time to a day per run, the number of particles will be between $10^5 - 10^7$, depending on the required accuracy of

the simulations and the number of simulated turns.

2.1.2 Magnetic field map

The code calculates trajectories of macro-particles in a 3D magnetic field map. The field map imported from an external file contains the field components, B_r, B_θ, and B_z on a polar, uniform grid. If an accelerator geometry has an azimuthal symmetry (periods), the field needs only be provided for a sub-period of a machine. It is assumed in the code that the field is symmetric with respect to the median plane and the field is given only for positive values of z.

To interpolate the field between the grid points a double-three point interpolation scheme is used. In the 1D case, the scheme uses the function value in four grid points to obtain the field and its first derivative between the second and the third grid points.

2.1.3 Equations of Motion

The code calculates trajectories of macro-particles in the magnetic field, solving a complete, unsimplified system of the equations of motion. It uses the classical 4th-order Runge-Kutta (RK) method to solve the system. The azimuthal angle, θ, is used as the independent variable. The azimuthal angle of a macro-particle can have only discrete values equal to angles of the nodes of the magnetic field grid. The angle increment per a complete RK step is equal to double the angular separation between the $r-z$ planes of the magnetic field grid. In the RK mid-steps, the particle falls into the $r-z$ plane which is in between the initial and the final planes. An exception is made when a macro-particle crosses an accelerating gap. In this case the

particle makes two complete RK steps to reach the second plane. Assuming that the intersection between the particle trajectory and an acceleration gap is between the jth and $j+2^{th}$ $r-z$ planes, first, the particle advances from the jth plane to the point of the intersection and then, with modified momenta, from the intersection point to the $j+2^{th}$ plane. Because the particle now falls between $r-z$ planes of the magnetic field grid, the magnetic field has to be interpolated in the azimuthal direction. This scheme almost completely eliminates the need to interpolate the magnetic field azimuthally and mostly requires 2D interpolation of the magnetic field in $r-z$ planes. This decreases the amount of calculations related to the field interpolation by almost a factor of four.

In developing the tracking part of CYCO, including RF acceleration, we have adopted many ideas used in the code SPIRALGAP [17], [18]. The implementation of the ideas, however, is different in our code. We developed CYCO using C++ instead of FORTRAN, the language that was used for programming SPIRALGAP. The two languages have substantially different approaches to programming and handling data. This made transferring the relevant code from SPIRALGAP to CYCO rather difficult.

The code uses the following parameters and notations:

- ω_0 is a parameter that has units of frequency and is provided by a user. If no RF system is used, ω_0 provides a time scale for the code. A natural choice, in this case, would be ω_0 equal to the angular revolution frequency of the beam.

  If the beam is accelerated, ω_0 is the angular frequency of the main RF divided by its harmonic number and is close to the revolution frequency. Angular frequency

of all the RF systems (main, flat-top, and so on) must be equal to $h\omega_0$, where h is a positive integer number. For restrictions on possible values of h see sections 2.1.4 and 2.2. The parameter ω_0 is also used to simplify the equations of motion in the code.

- a is the cyclotron length unit equal to c/ω_0, where c is the speed of light.

- $\tilde{p} = p/(m\omega_0)$ is the modified particle momentum in units of length. $\tilde{p}$ can be expressed via the relativistic factor γ and the first derivatives of the particle trajectory $\alpha_r = dr/(r\ d\theta)$ and $\alpha_z = dz/(r\ d\theta)$ in the horizontal and vertical planes by formulas:

$$\tilde{p}_\theta = a\sqrt{\frac{\gamma^2 - 1.0}{1.0 + \alpha_r^2 + \alpha_z^2}}$$

$$\tilde{p}_r = \alpha_r \tilde{p}_\theta \tag{2.1}$$

$$\tilde{p}_z = \alpha_z \tilde{p}_\theta$$

The system of the equations of motion, as programmed in the code, is

$$\frac{dr}{d\theta} = r\frac{\tilde{p}_r}{\tilde{p}_\theta} \tag{2.2}$$

$$\frac{d\tilde{p}_r}{d\theta} = \frac{\gamma r a \mathcal{E}_r + r(\tilde{p}_\theta B_z - \tilde{p}_z B_r)}{\tilde{p}_\theta B_0} + \tilde{p}_\theta \tag{2.3}$$

$$\frac{dz}{d\theta} = r\frac{\tilde{p}_z}{\tilde{p}_\theta} \tag{2.4}$$

$$\frac{d\tilde{p}_z}{d\theta} = \frac{\gamma r a \mathcal{E}_z + r(\tilde{p}_r B_\theta - \tilde{p}_\theta B_r)}{\tilde{p}_\theta B_0} \tag{2.5}$$

$$\frac{d(\omega_0 t)}{d\theta} = \frac{\gamma r}{\tilde{p}_\theta} \tag{2.6}$$

$$\frac{dE}{d\theta} = E_0\,\frac{r}{a}\,\frac{\vec{\tilde{p}}\cdot\vec{\mathcal{E}}}{\tilde{p}_\theta B_0} \tag{2.7}$$

16

where E is a kinetic energy of an ion, E_0 is the rest mass of the ion, $\gamma = 1 + E/E_0$, B_0 is a field parameter related to the frequency ω_0 as $\omega_0 = qB_0/mc$.

2.1.4 Acceleration

CYCO assumes that accelerating gaps are infinitely thin and the particle energy abruptly changes at each gap crossing. The number of acceleration gaps is not limited. Each acceleration gap can have its own shape that is given by the user in an external file as a tabulated function $\theta(r)$. Each acceleration gap can also have its own voltage, DEE-voltage profile, frequency, and phase shift.

Frequencies of all the RF systems must satisfy the equations:

$$\omega_1 = h_1 \omega_0 \tag{2.8}$$

$$\omega_2 = h_2 \, \omega_1$$

$$\dots \tag{2.9}$$

$$\omega_n = h_n \, \omega_1$$

where ω_1 is the frequency of the main RF.

The energy of the particle crossing the $n-th$ gap changes as $qV_n(r)\cos(\omega_n t + \phi_{n0})$. The momentum of the particle changes according to

$$\delta p_r = |\delta\vec{p}| \sin(\alpha) + \delta p_{\,b}$$

$$\delta p_\theta = |\delta\vec{p}| \cos(\alpha) \tag{2.10}$$

$$\delta p_z = 0$$

where $\vec{p}$ is the impulse provided by the gap and α is the gap angle. In addition to the energy change at each gap crossing, the program includes a radial impulse, δp_b, due to the RF magnetic field arising from the time derivative of the acceleration field $\partial \mathcal{E}/\partial t$.

2.2 Effect of neighboring turns

A beam in an isochronous cyclotron consists of many bunches that are accelerated simultaneously. Interference between bunches of neighboring turns, especially those that belong to the same branch, can have a significant impact on the beam dynamics and must be taken into account.

The code calculates the trajectories of macro-particles of a bunch, which we will call the "main" bunch. Propagating the macro-particles of the main bunch, the code calculates the coordinates of the macro-particles at time moments described by the formula

$$T_k = \frac{2\pi}{\omega_0 N_e} k \tag{2.11}$$

and saves them in the computer memory that yields the distribution of trailing neighboring bunches. In the last formula, ω_0 is the angular frequency parameter described in section 2.1.3, k is an integer number, and N_e is an integer number provided by the user.

Because leading neighbors represent the future of the main bunch, the distribution of the leading neighbors is unknown. To predict the distribution of the leading

bunches, CYCO creates a copy of the main bunch, which we will call the "auxiliary" bunch (see also picture 2.1). The total charge of the auxiliary bunch is the same as that of the main bunch. The number of macro-particles in the auxiliary bunch can be smaller than the number of macro-particles in the main bunch. In this case, the particles are randomly chosen from the main bunch. Tracking the macro-particles of the auxiliary bunch, the code saves the distribution of the bunch at time moments T_{k+1}, T_{k+2}, and so on, assuming that the auxiliary bunch was created at the moment T_k. This yields the predicted distribution of the leading neighbors. The code runs the auxiliary bunch for a time interval of

$$\delta T = \frac{2\pi}{\omega_0}(N_{nt} + N_s) \tag{2.12}$$

where N_{nt} is the number of neighboring turn bunches whose field is included each time the field affecting the main bunch is calculated. N_s is an integer provided by the user that defines how frequently the distribution of neighboring bunches is recalculated. When the code tracks the auxiliary bunch it calculates only the self-field of the bunch. The field of other bunches is neglected. Therefore, the shape of the auxiliary bunch slowly deviates from the self-consistent solution. To keep the error small the distribution of the leading neighboring bunches has to be periodically recalculated.

After the code finishes predicting the distribution of bunches of neighboring turns, it resumes tracking the main bunch. The space charge field affecting the macro-particles of the main bunch that includes the field of $2 \cdot N_{nt}$ neighboring turn bunches

i+2

Leading neighbors
(future)

i+1

i copy Main bunch

i-1

Trailing neighbors
(past)

i-2
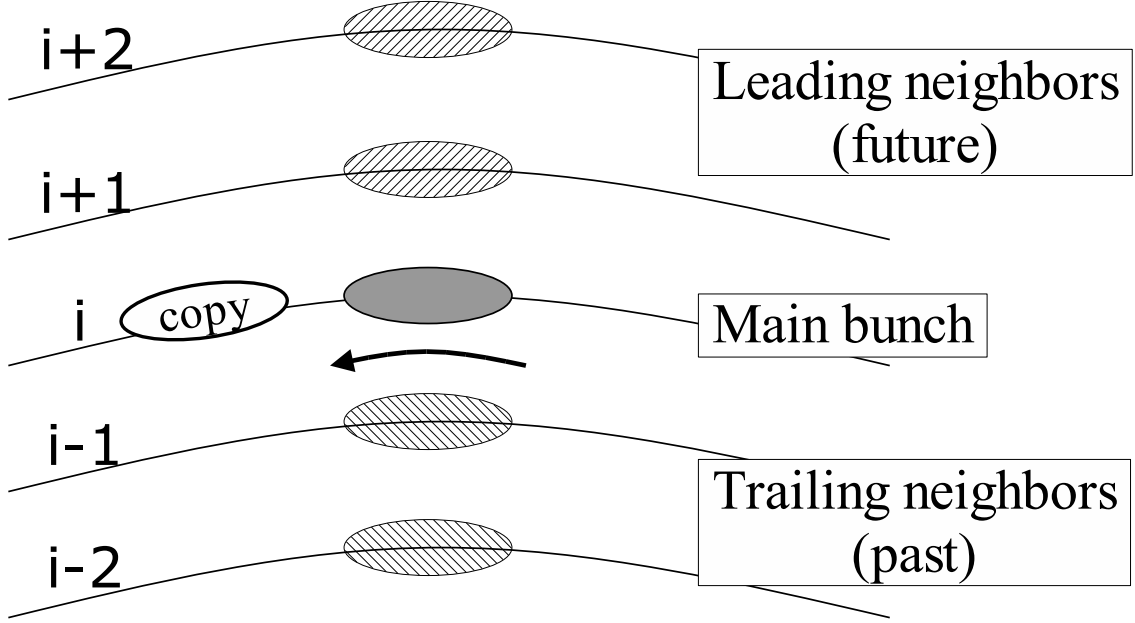
Figure 2.1: Propagating the main bunch, the code periodically saves coordinates of the macro-particles of the main bunch. This yields the distribution of the trailing neighbors. To predict the distribution of the leading neighbors, the code creates a copy of the main bunch and runs it ahead.

is calculated at time moments T_{k+1}, T_{k+2}, and so on. The code runs the main bunch

for a time interval of

$$\delta T = \frac{2\pi}{\omega_0} N_s \tag{2.13}$$

Then, the distribution of the leading bunches is recalculated. The whole procedure

repeats until the main bunch reaches the maximum radius or the integration time

exceeds the maximum allowed value. Both values are given by the user.

The code calculates three components of the space charge field: parallel to the

average horizontal velocity of the main bunch, perpendicular (horizontal) to the hor-

izontal velocity of the bunch, and the vertical components. The three components

of the field are assumed constant in the frame moving with the main bunch between

20

field calculations (see figure 2.2 for detailed explanation.) The frequency of the field calculations, defined by N_e, is chosen by the user and can be as high as once per each RK step. The same procedure is used to calculate the self-field of the auxiliary bunch.

If the number of neighboring turn N_{nt} is zero, then no neighbor is created. The field affecting the main bunch is only the self-field.

If there is no RF system in a simulated machine or its voltage is zero, the code cannot create the neighboring turns and tracks the main bunch alone. The self-field of the main bunch is calculated N_e times per time interval $2\pi/\omega_0$. In this case, ω_0 sets a time scale in the code and has no other physical meaning. The natural choice, of course, is ω_0 equal to the revolution frequency of the main bunch.

2.3 Calculation of the space charge field

The field solver calculates the electric field of a given beam charge distribution. To calculate the field the code uses the Particle-to-Mesh method. The charge of the beam particles is distributed over a 3D uniform rectangular grid. The Poisson equation is solved on the grid. In calculating the potential, the code assumes that the beam is contained between two horizontal, infinitely conducting planes, representing the walls of the vacuum chamber. Numerical differentiation of the potential yields the field at the grid nodes. The field is then interpolated back to the particles using the same distribution law that was used for the charge assignment.
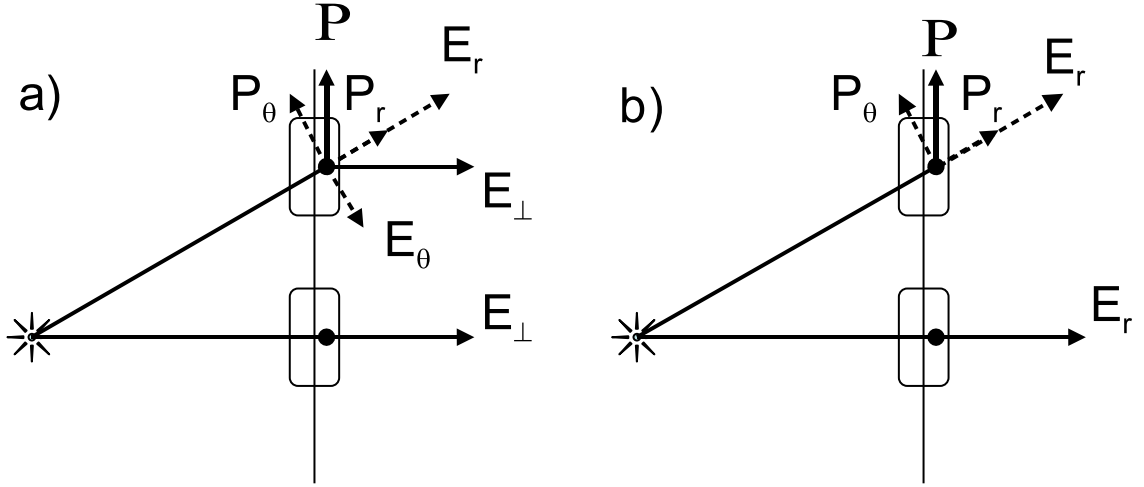
Figure 2.2: The code calculates the field components parallel and transverse to the horizontal bunch velocity. It assumes the components are constant between field calculations. Figure a) shows a bunch moving along a straight line from bottom to top of the picture. A particle in the middle of the bunch experiences only the transverse component. When the bunch is at zero angle (lower position) the transverse field is equal to the radial component. After the bunch moves, the transverse component is still the same as at $\theta = 0$. The transverse field, when projected on, r and θ directions yield the positive $\mathcal{E}_r$ and negative $\mathcal{E}_\theta$. The energy variation, which is proportional to the product $p_r \mathcal{E}_r + p_\theta \mathcal{E}_\theta$, is zero, in this case. If the code calculated $\mathcal{E}_r$ and $\mathcal{E}_\theta$ as shown in figure b) and kept them constant between field calculations, the product $p_r \mathcal{E}_r + p_\theta \mathcal{E}_\theta$ would not be zero. This would lead to an artificial particle energy growth.

2.3.1 Choice of grid parameters

The height of the grid, h_g, is equal to the distance between the conducting planes, representing the vacuum chamber. The number of horizontal layers in the grid, N_z, is provided by the user and does not change during execution of the code. N_z must be a multiple of 2.

Two vertical sides of the grid are placed parallel to the horizontal projection of the vector of the average velocity of the beam particles. The other two sides are perpendicular to the vector of the average horizontal velocity. The horizontal dimensions of the grid and the separation between the grid points depend on the beam size and the required resolution.

To understand how the code defines horizontal dimensions of the grid let's chose the direction parallel to the horizontal velocity and call it x. Let's call the other horizontal direction normal to x as y. The initial guess for the physical grid length is the maximum distance between the particles multiplied by a coefficient given by the user. By default, this coefficient is 1.3. This margin lets the code store Fourier transforms of the Green's function and use them for several field calculations without recalculating. (For more details on the Green's function see Section 2.3.3.) Then, the code doubles the size of the grid or adds the width of the Green function, whichever change is smaller. This is done to eliminate the wrap-around effect related to the intrinsic periodicity of the Fourier transformations. For a detailed discussion of this problem, see [13] and [20].

The third guess is based on a desirable resolution of the field calculations. The

user sets a desirable separation between the nodes of the grid, d_{xy}. The size of the

grid at the third step can be expressed via the separation between the nodes as

$$size\_at\_3d\_step = d_{xy} \, 2^{nx} \geq size\_at\_2nd\_step \tag{2.14}$$

where nx is the smallest possible integer that satisfies the non-equality. The same

algorithm is used to define the box size in the perpendicular direction, y. The sepa-

ration d_{xy} is the same in both directions x and y. If the product $2^{nx} \cdot 2^{ny}$ is smaller

then the maximum allowed value provided by the user, let's call it as $NXNY$, then,

the code proceeds to the calculation of the electric field. If the product is larger than

$NXNY$, the step between the nodes, d_{xy} is multiplied by 2 and both nx and ny are

decremented by one. If $2^{nx} \cdot 2^{ny}$ is still larger than $NXNY$, the last step is repeated

until $2^{nx} \cdot 2^{ny} \leq NXNY$. The procedure described above is done every time the space

charge field is calculated. The separation between the nodes is reset to the original

requested value. Thus, the size of the grid follows changes of the beam size.

The number of the nodes of the grid that will be used for the field calculations

is $N_z \cdot 2^{nx} \cdot 2^{ny} = Nx \cdot Ny \cdot Ny$, where we use notations N_x and N_y for 2^{nx} and 2^{ny}

respectively. An array that keeps the grid is allocated only once at the beginning

of code execution. The size of the array is equal to $N_z \cdot NXNY$. If the number of

nodes in the grid is smaller than the physical size of the array, only a part of the

array is used. If the requested number of nodes is too large, then, the code limits the

resolution: It increases the separation between the nodes but decreases the number

of requested nodes. Thus, the number of grid nodes is always smaller than or equal

to the physical size of the data array.

2.3.2 Charge assignment and field-interpolation scheme

The charge of a particle with coordinates (x,y,z) is divided between the 8 closest

points $(i, j, k)...(i + 1, j + 1, k + 1)$ according to the linear law:

$$w_{i,j,k} = \frac{q}{dz} \left(1 - \frac{\delta x}{d_{xy}}\right) \left(1 - \frac{\delta y}{d_{xy}}\right) \left(1 - \frac{\delta z}{dz}\right)$$

$$w_{i+1,j,k} = \frac{q}{dz} \frac{\delta x}{d_{xy}} \left(1 - \frac{\delta y}{d_{xy}}\right) \left(1 - \frac{\delta z}{dz}\right)$$

$$w_{i,j+1,k} = \frac{q}{dz} \left(1 - \frac{\delta x}{d_{xy}}\right) \frac{\delta y}{d_{xy}} \left(1 - \frac{\delta z}{dz}\right) \tag{2.15}$$

$$\cdots$$

$$w_{i+1,j+1,k+1} = \frac{q}{dz} \frac{\delta x}{d_{xy}} \frac{\delta y}{d_{xy}} \frac{\delta z}{dz}$$

where w is the grid array and δ_x, δ_y, and δ_z are distances along x, y, and z between

the particle and the node (i, j, k).

After the electric field has been calculated on the grid nodes it is interpolated

back to the location of each beam particle from the closest 8 nodes with the same

weights as in 2.15.

2.3.3 Poisson equation solver

Solution of the Poisson equation

To begin, let's calculate the potential created by charges on a single vertical meshline

of the grid. The charges of the column have the same x and y and are equidistantly

separated in the vertical direction. The field produced by the charges is a superposition of the field of the charges themselves and the field of image charges induced on the conducting planes at the top and bottom of the grid. The images can be arranged in an infinitely long chain of charges with a period equal to $2h_g$. The odd-numbered images have the charge opposite to the original charges while even-numbered images have the same charge. The infinite chain of charges that includes the original charges on the grid nodes can be represented as an infinite sum of sine functions

$$\rho = \sum \lambda_\gamma \sin\left(\gamma \frac{\pi z}{h_g}\right) \tag{2.16}$$

where γ is a positive integer. Coefficients λ_γ are sine Fourier harmonics of the linear charge density. Thus, calculation of the field of a column of point-like charges is reduced to the calculation of the field of a set of infinitely thin charged threads with the sinusoidal linear charge density. The charge density of each thread is zero everywhere except the line $r = 0$, where r is the distance (radius) from the column. To calculate the potential of each charged thread, we solve the Laplace equation in free space. We assume the potential produced by the $\gamma - th$ harmonic in the form of

$$\phi = \sin\left(\gamma \frac{\pi z}{h_g}\right) f_\gamma(r) \tag{2.17}$$

The Laplace equation in the cylindrical coordinates

$$\frac{1}{r}\frac{\partial}{\partial r}\left(r\frac{\partial \phi}{\partial r}\right) + \frac{1}{r^2}\frac{\partial^2 \phi}{\partial \theta^2} + \frac{\partial^2 \phi}{\partial z^2} = 0$$

yields for the $\gamma - th$ harmonic

26

$$\frac{d^2 f_\gamma}{dr^2} + \frac{1}{r}\frac{df_\gamma}{dr} - \frac{\gamma^2 \pi^2}{h_g^2} f_\gamma = 0 \qquad (2.18)$$

The acceptable solution of the equation 2.18 is the modified Bessel function $K_0(\gamma \pi r / h_g)$. The potential created by the $\gamma - th$ harmonic can be written in the form

$$\phi = \phi_\gamma \sin\left(\gamma \frac{\pi z}{h_g}\right) K_0\left(\gamma \frac{\pi r}{h_g}\right) \qquad (2.19)$$

The normalization constant ϕ_γ depends on λ_γ and is a "link" between the potential, which is a solution of the Laplace equation, and the Poisson equation. To find λ_γ let's choose a point at the height of any maximum of the charge density and assume its coordinate, z', be equal to zero. Then, the potential at a distance r and $z' = 0$ can be calculated as

$$\phi(z' = 0) = \int_{-\infty}^{\infty} \frac{\lambda_\gamma \cos(\gamma \pi z'/h_g)dz'}{\sqrt{r^2 + z'^2}} = 2\lambda_\gamma \int_0^\infty \frac{\cos(\gamma \pi z'/h_g)dz'}{\sqrt{r^2 + z'^2}} \qquad (2.20)$$

The integral can be found, for example, in the reference [21] and is equal to

$$\phi(z' = 0) = 2\lambda_\gamma K_0\left(\gamma \frac{\pi r}{h_g}\right) \qquad (2.21)$$

Comparing 2.21 with 2.19 one can easily conclude that $\phi_\gamma = 2\lambda_\gamma$. Thus, the potential created by the $\gamma - th$ harmonic is equal to

$$\phi = 2\lambda_\gamma \sin\left(\gamma \frac{\pi z}{h_g}\right) K_0\left(\gamma \frac{\pi r}{h_g}\right) \qquad (2.22)$$

Using formula 2.22, we can calculate the potential created by the column of charges as

$$\phi = 2\sum_{\gamma}\lambda_{\gamma}\sin\left(\gamma\frac{\pi z}{h_g}\right)K_0\left(\gamma\frac{\pi r}{h_g}\right) \tag{2.23}$$

The potential at a given grid node with coordinates (x, y, z) produced by the whole grid can be calculated as

$$\phi_{i,j,k} = 2\sum_{\gamma}\sin\left(\gamma\frac{\pi z}{h_g}\right)\sum_{\xi,\eta}\lambda_{\gamma}(\xi,\eta)K_0\left(\gamma\frac{\pi\sqrt{(x-\xi)^2+(y-\eta)^2}}{h_g}\right) \tag{2.24}$$

where ξ and η are horizontal coordinates of columns of the 3D grid.

Convolution method

A direct summation of the second sum in Equation 2.24 can be time consuming if the number of vertical columns in the grid is large. The time required to calculate the sum for all the grid nodes grows quadratically with the number of columns if the sum is calculated by simple addition. A faster way to calculate sums similar to 2.24 is to use the convolution theorem and the Fast Fourier Transformations (FFT). A general description of the convolution method can be found in [13]. Mathematical details of the convolution method and FFT are discussed in [20]. Here we present only details related to the implementation of the method in the code.

First, the code constructs N_z two-dimensional Green's functions, as follows:

$$G_{i,j,\gamma} = \begin{cases} 2\, d_{xy}\, K_1\left(\gamma\dfrac{\pi d_{xy}}{h_g}\right)\dfrac{\gamma\pi}{h_g} + K_0\left(\gamma\dfrac{\pi 2 d_{xy}}{h_g}\right) & : & i,j = 0 \\[2ex] 2\, K_0\left(\gamma\dfrac{\pi r_{i,j}}{h_g}\right) & : & 1 \le i,j \le \dfrac{N_x}{2}, \dfrac{N_y}{2} \text{ and } r_{i,j} \le arg_{max} \\[2ex] 2\, K_0(arg_{max}) & : & 1 \le i,j \le \dfrac{N_x}{2}, \dfrac{N_y}{2} \text{ and } r_{i,j} > arg_{max} \end{cases} \tag{2.25}$$

$$G_{N_x-i,j,\gamma} = G_{i,N_y-j,\gamma} = G_{N_x-i,N_y-j,\gamma} = G_{i,j,\gamma} \tag{2.26}$$

where K_1 is the modified Bessel function of the first order. Recalling that $K_0'(x) = -K_1(x)$, one can easily see that this choice of $G_{0,0}$ gives the correct electric field at the nodes one step away from the origin if the differentiation formulas

$$\begin{aligned} \mathcal{E}_{x\,i} &= -\frac{\phi_{i+1} - \phi_{i-1}}{2 d_{xy}} \\[2ex] \mathcal{E}_{y\,j} &= -\frac{\phi_{j-1} - \phi_{j-1}}{2 d_{xy}} \end{aligned} \tag{2.27}$$

are used. (Irrelevant indexes are omitted in this formulas.)

The code limits the width, that is the maximum argument, of the Bessel function. The modified Bessel function $K_0(\xi)$ can be approximated by the formula $exp(-\xi)/\sqrt{\xi}$ for large ξ. Thus, K_0 decays very quickly with r, especially for large vertical wave numbers γ. The code calculates the modified Bessel function only for the argument of the function, $\gamma\pi r/h_g$, smaller than a given maximum value, arg_{max}, provided by the user. For all points with the argument larger than arg_{max} the true value of $K_0(\gamma\pi r/h_g)$ is substituted by $K_0(arg_{max})$. With this choice, the first derivative of the Green function is a monotonous function of its argument, decaying to zero at arg_{max}. If K_0 were padded with zeros beyond arg_{max}, the electric field would have a bump at arg_{max}.

The calculated values of the Green's functions are stored in an array in the computer memory. The 2D Fourier transform is calculated in the xy plane for each Green's function, that is for each vertical wave number γ, and stored in the same array overriding the calculated Green's function values. The stored harmonics are used until the size of the grid changes.

After the charge of the beam particles has been assigned to the nodes of the 3D grid the sine FFT is performed for each vertical column of the grid. After this procedure, each horizontal xy plane of the grid contains the horizontal distribution of λ_γ for a given γ.

To calculate the second sum in the formula 2.24 for a given γ the code performs the two-dimensional FFT for $\gamma-th$ plane of the main grid. This gives Fourier harmonics of the horizontal distribution of λ_γ. The Fourier transforms of the horizontal distribution of λ_γ are multiplied by the Fourier transforms of the corresponding Green's function stored in the auxiliary array. The product of the Fourier transforms is the Fourier transform of the the second sum in Equation 2.24

$$\text{SUM}_{\alpha,\beta,\gamma} = \lambda_{\alpha,\beta,\gamma} G_{\alpha,\beta,\gamma} \tag{2.28}$$

The 2D inverse Fourier transform yields the sum for a given vertical wave number. This procedure is performed for all the layers of the grid. At last, the code performs the inverse sine Fourier transform in the vertical direction yielding the potential given by the formula 2.24 for all the nodes of the grid.

2.3.4 Field solver test

The field solver was used to calculate the electric field of the point charges distributed over nodes of a 3D uniform grid. The field of two charge distributions were simulated: a uniformly charged sphere and a long segment of a uniformly charged rod. The field calculated by the field solver was compared to the field calculated by a direct summation of the field of the nodes and their images. In the case of the sphere the field created by a uniformly charged sphere and its images was also calculated analytically. This comparison gives an idea how well the discrete charged-node model represents the continuous 3D charge density.

Sphere

The electric field produced by a uniformly charged sphere of a radius of 10 mm was calculated by the field solver. The field of the sphere was calculated on the nodes of a grid that was 64 mm long, 128 mm wide, and 50 tall. The grid had $N_x \cdot N_y \cdot N_z = 64 \cdot 128 \cdot 64$ nodes. The distance between the nodes was 1 mm in the horizontal directions and 0.78125 mm in the vertical one. The (0,0,0) node had the coordinates (x,y,z)=(0,0,0). The center of the sphere was at (x_c,y_c,z_c)=(20,20,25). Each grid node with coordinates x,y and z satisfying the inequality

$$\sqrt{(x - x_c)^2 + (y - y_c)^2 + (z - z_c)^2} \leq 10 \text{ mm} \qquad (2.29)$$

was assigned a unit charge. Thus, the solver actually calculated the field of a set of unit charges with coordinates satisfying the inequality 2.29.

The field calculated by the solver was compared to the field calculated by a simple summation over the mesh nodes and their images

$$\vec{\mathcal{E}}_i = \sum_j \sum_{k=-K}^{k=K} \frac{(-1)^k q_j}{r_{i,j,k}^3} \vec{r}_{i,j,k} \quad k \neq 0 \tag{2.30}$$

where the second summation includes the image charges. The number of image charges K was set to 10, giving the total number of image charges equal to 20. The outermost charges had a half-charge, $0.5 \cdot q_j$, to keep the total charge equal to 0.

The field produced by the sphere and its twenty closest images was also calculated analytically and then compared to the fields calculated by the field solver and the field calculated by a summation over the node charges.

Figure 2.3.a shows $\mathcal{E}_x$ calculated by all the three methods along the x-axis of the sphere. The figure 2.3.b shows the difference of the first two fields (the field calculated by the solver and the field calculated by a summation over the nodes) from the field calculated analytically.

As follows from the figures 2.3.a and 2.3.b the difference between the field calculated by the field solver and the field calculated by the summation over all the nodes and their images is small inside and outside the sphere. The difference reaches its maximum value of approximately 1% at the edge of the sphere. This difference is mostly caused by the fact that the field solver calculates the potential and then differentiates the potential according to

$$\mathcal{E}_i = -\frac{\phi_{i+1} - \phi_{i-1}}{2h}$$

If we calculate both fields from the potential using the differentiation formula,

32
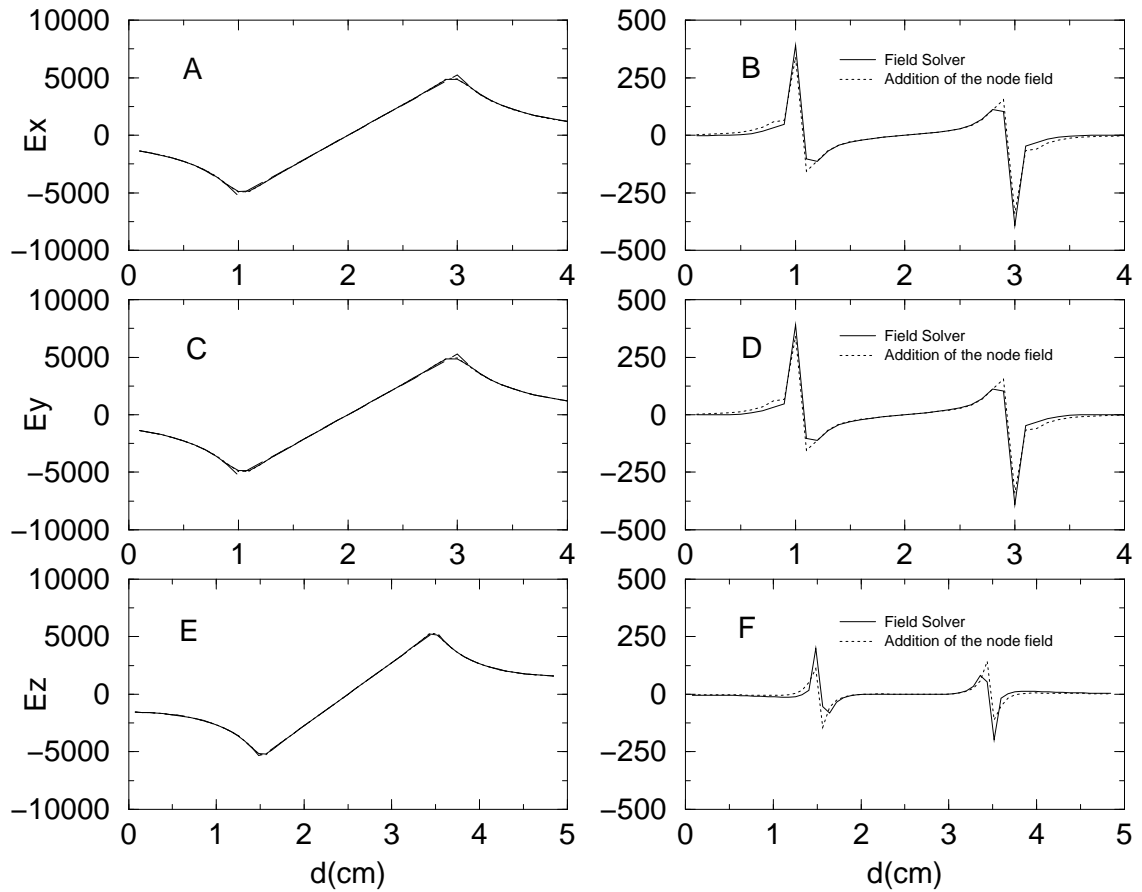
Figure 2.3: a) $\mathcal{E}_x$ calculated along the x-axis of the sphere vs. x. The figure shows the field calculated by three methods: field solver, direct summation of the electric field of the nodes, and the field of the uniformly charged sphere and its images, calculated analytically. All three curves almost completely overlap. b) The difference of the two first fields (see explanations for a.) from the field calculated analytically. Figures c), d), e), and f) are similar to a) and b) but show the other components of the field.

then, the error decreases to 0.35% . The residual error decreases if the number

vertical grid nodes increases. This indicates that the residual error is, most probably,

due to the finite number of the vertical harmonics used in the field solver.

The difference of the field produced by the grid nodes from the field of the uni-

formly charged sphere and its images calculated analytically is very little inside and

outside the sphere but reaches approximately 7% at the edge of the sphere. This fact

means that the discrete node model created as described above (see Eq.2.3) does not

work extremely well at the edges of the sphere. Note that we have not used the charge

assignment scheme described in 2.3.2 that would smooth the edge of the model.

Figures 2.3.c and 2.3.d show results similar to those shown in 2.3.a and 2.3.b for

$\mathcal{E}_y$ calculated along the y-axis of the sphere. Although the y size of the box is twice

as large as that in the x direction, the step size in y-direction is the same as that in

the x direction and equal to 1 mm.

The difference between the models becomes smaller for the $\mathcal{E}_z$ component calcu-

lated along the z-axis of sphere (figures 2.3.e and 2.3.f). The step size in the vertical

direction is also smaller: 0.78125 cm instead of 1 mm in x and y directions.

Uniformly charged rod

To check the solver we have also calculated the field produced by a segment of uni-

formly charged rod. The radius of the rod was 10 mm and the length of the rod was

200 mm. All the grid nodes that satisfied the following two conditions

$$\sqrt{(x - x_c)^2 + (y - y_c)^2} \leq 10 \text{ mm}$$

$$20 \leq y \leq 220 \text{ mm}$$

were assigned a unit charge. The axis of the rod had the coordinates $x_c = 20$ mm and $z_c = 25$ mm. The grid size was $d_x \cdot d_y \cdot d_z = 64 \cdot 512 \cdot 50$ mm^3. The number of mesh nodes was $64 \cdot 256 \cdot 64$, yielding the step size of 1 mm in x and y directions and 0.78125 mm in the z-direction.

The field produced by the nodes was calculated by the field solver and then compared to the field calculated by a simple summation of the field of the nodes and their images. In calculating the latter field we have included 10 images from each side, assuming a charge of 0.5 for the two outermost images. Figures 2.4.a, 2.4.c, and 2.4.e show the $\mathcal{E}_x$, $\mathcal{E}_y$ and $\mathcal{E}_z$ components of the electric field calculated by the field solver and calculated by the direct summation of the field produced by the grid nodes. Figures 2.4.c and 2.4.d show also the field of a uniformly charged rod calculated analytically in the assumption that the rod is infinite and in a free space (no image charge is included). Figures 2.4.b, 2.4.d, and 2.4.f show the difference between the field calculated by the field solver and the field calculated by the summation over the nodes. As in the case of the sphere, the difference between these two fields is very little inside and outside of the charged region. The difference reaches its maximum value of approximately 1% at the edges of the rod.
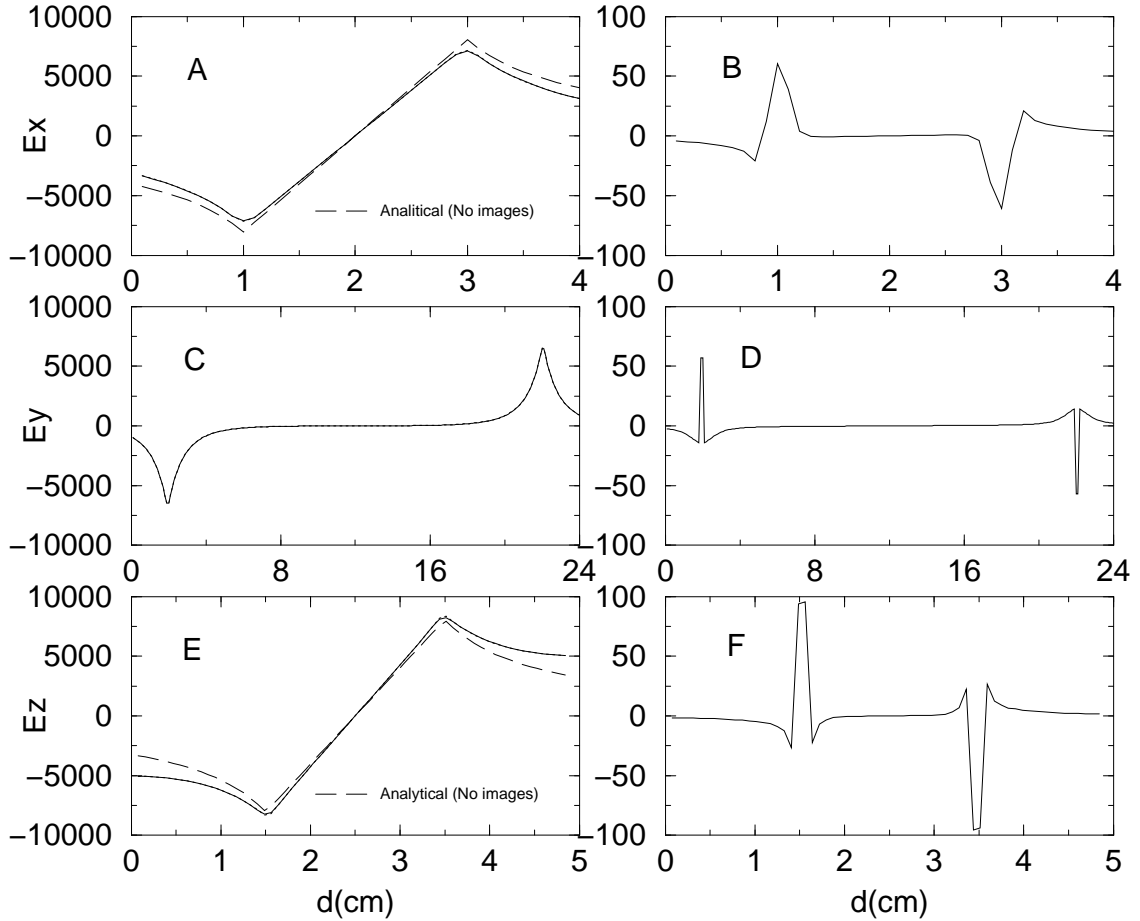
Figure 2.4: a) $\mathcal{E}_x$ calculated along the x-axis of the rod, in the middle of the rod, vs. x. The figure shows the field calculated by two methods: field solver and direct summation of the electric field of the nodes their images. The two curves almost completely overlap. The figure also shows the electric field of an infinite, uniformly charged rod, calculated analytically. In this case, no image charges were included. b) The difference of the two first two fields (calculated by the solver and by direct summation) from each other. Figures c), d), e), and f) are similar to a) and b) but show the y and z components of the field. The y component was calculated along the long (y) axis of the rod.

Summary of the field solver test

The results presented show that the field solver accurately calculates the field created by the charged nodes. The accuracy of the field calculation is lower in the regions of abrupt variation of the charge density. This is mostly caused by the accuracy of the differentiation scheme employed.

The results of the test also show that the effect of discretization of the continuous charge density can limit the accuracy of simulations in regions of abrupt variation of the charge density. Further simulations (not presented here) show that this effect decreases as the separation between the grid nodes decreases.

2.4 Beam distribution input-output

The code obtains the initial distribution from an external file provided by the user. The file must contain the distribution of the test bunch at the time $t = 0$. Each line of the file defines the initial coordinates of a main bunch macro-particle including the radius, r_i, the first derivative of the particle trajectory in the horizontal plane, $\alpha_r = dr/(r \, d\theta)$, a vertical displacement from the median plane, z_i, the first derivative of the trajectory in the vertical plane, $\alpha_z = dz/(r \, d\theta)$, the kinetic energy, E_i, and the initial angle θ_i. The initial azimuthal angle of particles θ can have any value and does not have to be equal to the angle of any $r - z$ plane of the field grid.

The code output has two modes: output at a given angle and output after a given turn number. In the first case, the code outputs coordinates of particles at a specified angle, simulating information obtained from a differential radial probe in a

cyclotron. It can be useful if a user wants to calculate the radial beam size and the turn separation at a given angle. This can be of particular interest for extraction studies.

In the second mode, the code periodically outputs coordinates of particles after time intervals given by:

$$i \cdot n \frac{2\pi}{\omega_0}, \quad i = m, m + 1 \dots m + k$$

where k, m, and n are positive integer numbers. In the second mode, the user can request output of both the main bunch and neighboring bunches. The second mode has two options: The code can provide the coordinates of the particles or it can produce a two-dimensional histogram of the beam charge distribution.

For debugging purposes, one can opt for a printout of coordinates of chosen particles. This output flows to the standard error stream that is normally a computer display.

2.5 Code structure

The code is written in C++ (ANSI/ISO International Standard) and is a console application. The program reads input parameters from a file provided by a user. Files are also used for input of such data as initial distribution, magnetic field map, and parameters of RF systems. The code outputs the particle data to files. Service messages and debug information are output to the standard output and error streams that are usually the display screen. All this allows one to compile and run the code

without modifications, in principle, on any computer system that has a modern C++ compiler.

The code structure is based on C++ classes. Below is a list of main classes with a short description of class members and member functions:

- An object of **class CGParameters** reads parameter-value pairs from a file provided by a user and keeps them in memory. The class has the overloaded member function GetVal:

  - char *GetVal(const char *$varname$)

  - char *GetVal(const char *$varname$, int $defval$)

  - char *GetVal(const char *$varname$, double $defval$)

  - char *GetVal(const char *$varname$, char *$defval$)

  The member function GetVal, when called, returns a string of characters with a value of the variable str. If the function cannot find the variable str in the list of parameters read from the parameter file it returns the default value $defval$. If no default value is provided, what means that the user must provide the value for str otherwise the execution of the code is impossible, then the program quits.

- **class CBField** contains the magnetic field which is read from a file provided by a user. The class has the overloaded member function GetField:

  - void GetField(int i, double r, double z, double &Br, double &Bt, double &Bz)

– void GetField(double *theta*, double r, double z, double &Br, double &Bt,

double &Bz)

GetField returns the radial, tangential, longitudinal components of the magnetic field as Br, Bt, and Bz respectively for a particle with the radius r and vertical displacement z. The first form calculates the field for a particle which has the same angle as i-th $r - z$ plane of the field grid. The function interpolates the field in r and z. The second form returns the field for the angle *theta*. The second form requires also interpolation in azimuth. The second form is mainly used when a particle crosses an acceleration gap between $r - z$ planes of the field grid.

- **class CParticle** contains attributes related to a single macro-particle: its co-ordinates and status (dead or alive). Particles belonging to the test bunch and the auxiliary bunch (see the definitions in section 2.2) have the type CParticle.

- **class CIon** is similar to CParticle. CIon contains coordinates and status of particles of neighboring bunches. The CIon class does not contain service class members related to tracking in the magnetic field. That is why objects of the class CIon are significantly smaller than CParticle objects.

- **class CGap** contains information and functions related to RF systems used in the code. The function ReadGap reads the shape of the accelerating gaps from a file, their frequencies, voltages, and initial phases and stores all this information in the computer memory. If a particle crosses an acceleration gap during a

consecutive integration step the member function ThGap returns 1 and the other member function Intersect finds the azimuthal angle of the intersection.

- **class CEqOfMot** The overloaded function Adv propagates a particle by a single Runge-Kutta step. It has to forms:

  - int Adv(CParticle &*part*, CBField **B*)

  - int Adv(CParticle &*part*, CBField **B*, double *dth2*)

  The first form of the function propagates a particle from i-th $r - z$ plane of the magnetic grid to the $i + 2$-th plane. The two intermediate steps of the RK step fall into the $i + 1$-th plane. This form of Adv calls only the first form of CBField::GetField (a member function of CBField, see above). The second form of Adv propagates a particle by an arbitrary angle *dth2*. This form of Adv uses the second form of the CBField::GetField. Adv returns 1 if the last step was successful and 0 otherwise. Finally, the member function ChngEPr changes the energy of the particle and its momenta when the particle crosses an acceleration gap.

- **class CSystem** is the base class for the test (CSystemS1) and auxiliary (CSystemS0) bunches. It contains members that are common for the test and auxiliary bunches: status, number of particles, and a pointer of the CParticle type. The class member function Advance (int Advance(double t, CEqOfMot **EOM*, CBField **B*, CGap **Gap*)), propagates the particles of a bunch by a single Runge-Kutta step. The function is called until the time of all particles ex-

ceeds the time given by the first parameter t. It also calculates and stores the coordinates of the particles at time moment t. There are two member functions: RPTav (void RPTAv()) and XYMinMax (void XYMinMax(double rav, double $thav$, double $alphap$, double $\&xmintmp$, double $\&xmaxtmp$, double $\&ymintmp$, double $\&ymaxtmp$)). The functions calculate the particle velocity and its direction and the beam size projected on the vector of the beam average velocity. This information is used for calculation of the space charge field. It is worth noting here that no object of CSystem type is created in the code. CSystem is inherited by CSystemS0 and CSystemS1.

- **class CSystemS1** is derived from the class CSystem. The program creates an object of the class CSystemS1 that contains particles of the test bunch. The class CSystemS1 has a function CreateParts that reads the initial distribution of the test bunch from a file provided by a user. The member functions OutFile and ThPrn of the class CSystemS1 are responsible for particle output.

- **class CSystemS0** The program creates an object of the class CSystemS0 that contains particles of the auxiliary bunch. The class CSystemS0 redefines the function CreateParts, which just create an array of CPartcile objects. In addition, CSystem0 defines an overloaded version of the assignment operator CSystemS0 CSystemS0::operator=(CSystemS1 $\&s1$), which essentially arbitrarily copies a given number of particles from the test bunch (objects $s1$) to the auxiliary bunch.

- Objects of the **class CSystemS2**type are used to store particles of the neigh-

boring bunches. Particles in CSystemS2 objects are of the type CIon instead of CParticle as in CSystemS0 and CSystemS1.

- **class CEField** is the base class for classes CEField1 and CEField2. It contains members and member functions related to calculation of the space charge field of the test bunch and the neighboring bunches. The function BoxSize calculates the size of the grid required for field calculation. The function PutGreen calculates the values of the Green function on the grid nodes. The function Solver calculates the potential at the grid nodes. The functions that distribute the beam charge density over the grid and the function that interpolates the field back on the particles depend on a particular case: the test bunch or the auxiliary bunch. Different instances of these functions are defined in classes CEfield1 and CEField2. It is necessary to note that no object of class CEField is created in the program. CEField only defines a double pointer. This pointer is used by the derived classes to allocate the required memory for the grid.

- **class CEField1** is derived from the base class CEField. The only object of this class created by the program is used to calculate the space charge field affecting particles of the test bunch. The function PutDist distributes the charge of particles of the test and neighboring bunches. Functions defined in the base class CEField are used to solve the field on the grid. At last, the member function GetField interpolates the field from the grid nodes to the particles of the test bunch. The class CEFiedl1 is a friend of classes CSystemS1 and CSystemS2. This grants functions of CEField1 an access to particles of the

test and neighboring bunches that are protected members of CSystemS1 and CSystemS2.

- **class CEField2** is derived from the base class CEField. An object of this class created by the program calculates the self-field of the auxiliary bunch. With some little exceptions, the class CEField2 is similar to CEfield1. CEfield2 is a friend of CSysstemS0. This grants CEField2 access to private members of CSystemS0.

2.6   Comparison to the program PICN

We simulated the beam dynamics of a 2 mA, 5 MeV beam in PSI Injector 2, using CYCO and PICN. The results of the simulations obtained by the programs are compared in this section.

To run CYCO, we used the magnetic field ZYKL9Z provided by Martin Humbel and Andreas Adelmann. The 2D field map ZYKL9Z was extended in the vertical dimension according to the formulas

$$
\begin{aligned}
B_r(z) &= z\frac{\partial B_0}{\partial r} \\
B_\theta(z) &= \frac{z}{r}\frac{\partial B_0}{\partial \theta} \\
B_z(z) &= B_0
\end{aligned}
\tag{2.31}
$$

where B_0 is the z-component of the field in the median plane, given in the 2D field map. The vertical beam size was 4 mm, the radial size was 5 mm. In the longitudinal direction, the macro-particles were randomly distributed with the probability

described by the Gaussian curve with an r.m.s size of 8 mm. All macro-particles with the deviation larger than 3σ were discarded. The total number of the macro-particles was 10^5. The initial energy spread within the beam was zero.

As mentioned in section 1.2, the program PICN treats the bunch as a set of needles of a fixed hight. The number of the needles used by PICN was $2 \cdot 10^5$. The beam in PICN simulations had the same hight and width as those in the CYCO simulations. The longitudinal distribution of macro-particles was similar in both cases. Note that we were not able to find information on the exact shape of the longitudinal distribution used in PICN to generate an identical distribution in CYCO.

Figures 2.5 and 2.6 show the results of the simulations by PICN and CYCO. As follows from the figures, both programs predicted similar beam behavior in the PSI Injector 2: The space charge force caused the bunch to deform into a galaxy-like shape in a few urns. After approximately 10 turns, the bunch transformed into a round distribution, which changed little after it has formed.
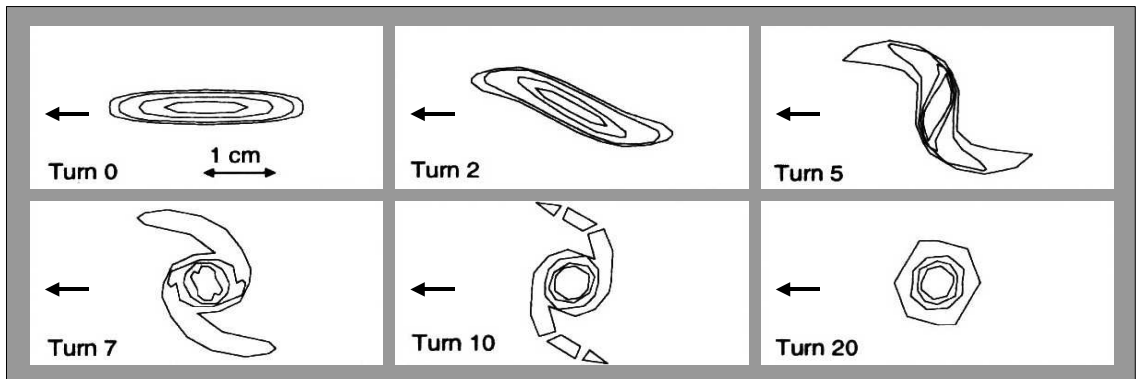
Figure 2.5: The distribution of a bunch of the 2 mA, 5 MeV proton beam in PSI Injector 2 simulated by PICN. The contour plot levels correspond to 10%, 20%, 50%, and 80% of the maximum charge density. Arrows on the figures show the direction of the beam motion. The figure with the initial distribution (Turn 0) provides the scale.
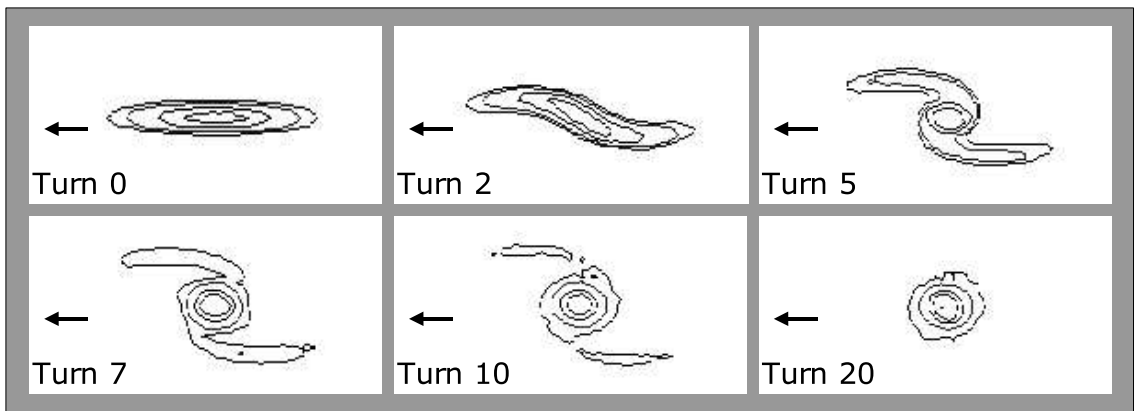
Figure 2.6: The beam dynamics in PSI Injector 2 simulated by CYCO. The beam current was 2 mA, the beam energy was 5 MeV. The contour plot levels correspond to 10%, 20%, 50%, and 80% of the maximum charge density. The scale of the figure is the same as that of the figures with the PICN results.

Chapter 3

SIMULATION OF THE BEAM DYNAMICS IN

SIR

3.1 Hard-edge model

3.1.1 Ring optics

The SIR optics had several major requirements:

- To simulate a part of an isochronous cyclotron it was necessary to use magnetic dipoles. Electrostatic bends are unacceptable since in these elements particles with larger radius lose kinetic energy at the entrance of a bend and move slower than the particles with smaller radius that gain the kinetic energy at the bend entrance. On the contrary, a magnetic bend does not change the kinetic energy of particles. Thus, the velocity of particles does not depend on their position at the entrance/exit of a magnetic bend.

- It has to be isochronous

- The optics scheme has to be as simple as possible to reduce the time and financial expenses required to build the ring

- The ring must be large enough to accommodate diagnostics and other required subsystems but smaller than the available 3x3 meter^2 area.

The simplest scheme that gives an isochronous solution consists of dipole magnets with edge focusing. As shown in Appendix B, a low energy ring that consists of N dipoles is isochronous if the pole-face angle is given by

$$\tan\left(\alpha_e\right) = \frac{L/2}{R + \dfrac{L/2}{\tan\left(\frac{\pi}{N}\right)}} \tag{3.1}$$

where α_e is the pole-face angle, R is the radius of the magnets, and L is the distance between the magnets. The ratio L/R with the edge angle given by Equation (3.1) determines the betatron tunes ν_x and ν_y.

Using the program DIMAD [22], we have studied how ν_x and ν_y depend on L/R for different N. The analysis has shown that all schemes of an acceptable size with $N \geq 5$ had ν_x very close to 1. An attempt to increase L with fixed R primarily affected ν_y and α_e. The radial tune, ν_x, on the contrary, grew very slowly. Another complication came from the fact that both ν_x and ν_y depend on the same parameter L/R. This made choosing the working point far from dangerous resonances more difficult.

Figure 3.1 shows the tunes for optics with four and five periods. The magnet radius R for these simulations was 0.45 m. The length of the drift between magnets changed from 0.4 m to 1.4 m in increments of 0.2 m. As shown in figure 3.1, a value of $\nu_x - 1$ for $N = 5$ was approximately twice as low as that for $N = 4$. In both cases, the vertical tune ν_y depended on L much stronger than ν_x. For L smaller than 0.6 m,
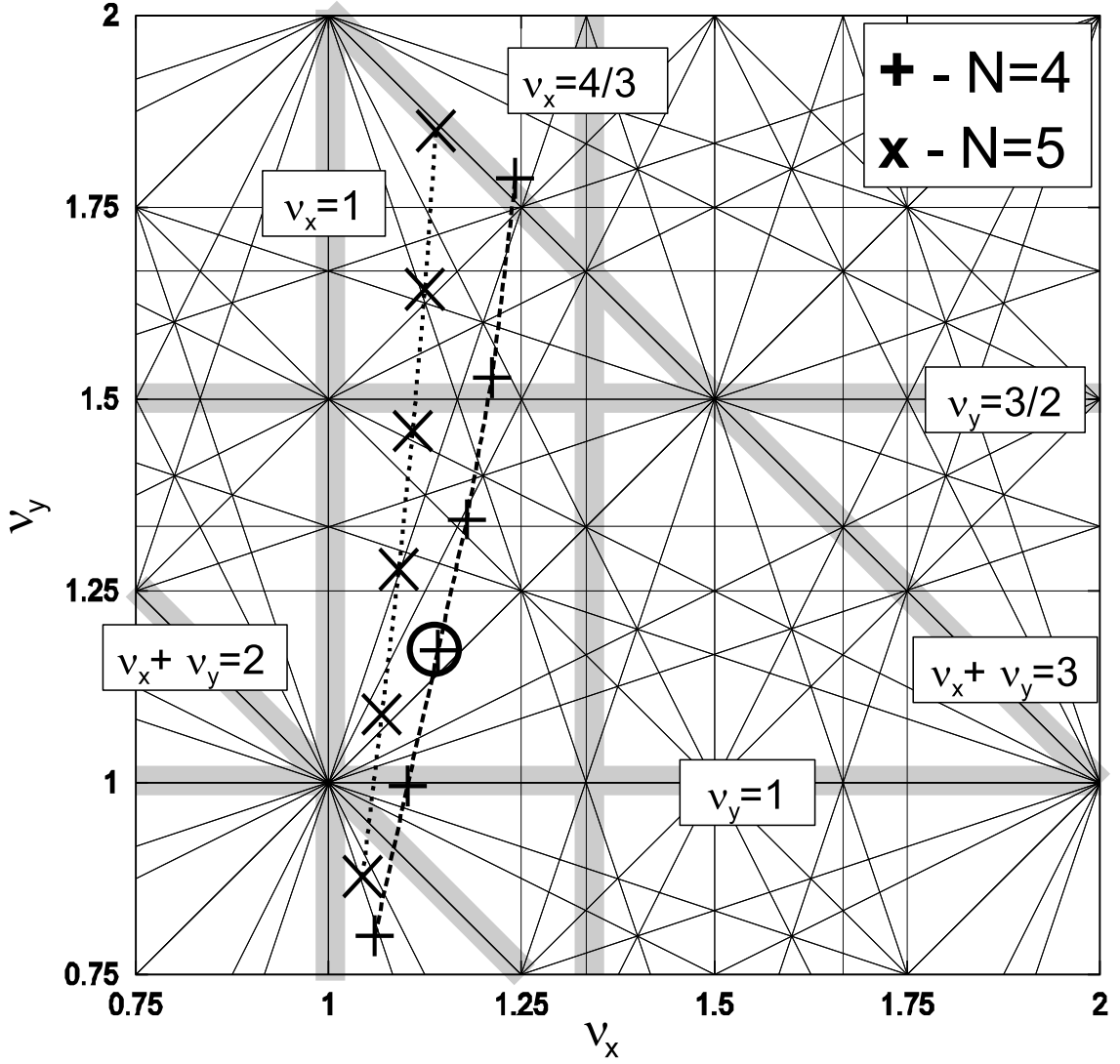
Figure 3.1: The tune diagram for optical schemes with four (+'s) and five (X's) magnets. The magnet radius was 0.45 m. The length of the drifts was changed from 0.4 m to 1.4 m with a step of 0.2 m. The edge angle was changed according to Equation 3.1 to provide isochronism. Though both ν_x and ν_y grew with the drift length, the vertical betatron tune depended on the drift length much stronger than the radial one. The circle shows the working point chosen for SIR ($\nu_x = 1.14, \nu_y = 1.17$).

the working point was too close to the integer resonances $\nu_x = 1$ and $\nu_y = 1$ and the sum resonance $\nu_x + \nu_y = 2$. For L larger than 0.9 m, the working point was in the region densely populated by strong vertical and sum coupling resonances. The most appropriate place for the SIR working point on the tune diagram was a square with a diagonal between the points (1.0,1.0) and (1.25,1.25). The density of resonances in this area was relatively low. Moreover, all order four or less resonances intersecting the area were difference resonances that only couple the transverse motion in x and y planes but do not cause an infinite growth of the betatron amplitudes.

The optical scheme that has been adopted for SIR has four magnets. Parameters of the solution that satisfy the requirements mentioned on page 47 are listed in Table 3.1. Figure 3.2 shows the optical functions vs. distance for a single period of the ring calculated by DIMAD.

3.1.2   Effect of alignment and manufacturing errors

In this section we evaluate the effects of alignment and manufacturing errors on the beam dynamics in SIR. We also estimate the effect of stray magnetic fields. The errors considered can be separated into two groups:

- Errors that primarily affect the closed orbit, including errors in the magnet gap, magnet length, vertical position of the magnets, rotation of the magnets around the beam axis, stray fields.

- Errors that affect the betatron tunes and isochronism: tilt of pole tips in the dipole magnets, magnet pole face rotation, free drift length error

Table 3.1: Parameters of SIR (hard-edge model)

N	4	α	25.159°
R	0.45 m (17.717")	ν_x	1.14
L	0.79714 m (31.383")	ν_y	1.17
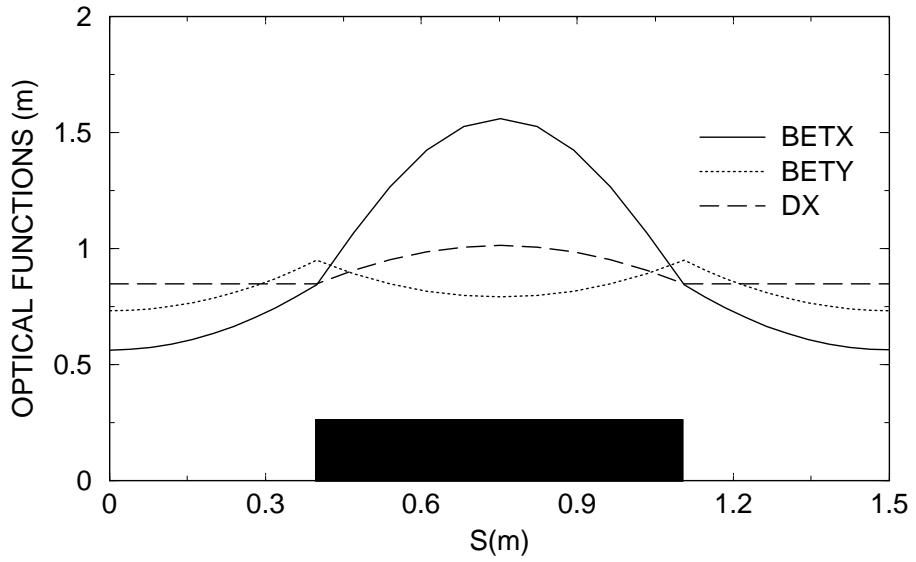
Figure 3.2: The optical functions vs. distance of a single period of the ring. The black rectangle schematically shows one of the dipole magnets.

To estimate the effect of a given error on the beam, we introduced the error into a single magnet or a drift and calculated the effect using DIMAD. Knowing how the localized error affects the beam and using the fact that the betatron tunes are close to unity, we could easily estimate the maximum possible distortion produced by the error of the same magnitude or weaker, arbitrarily introduced in all the four dipoles. If the error affects the closed orbit, the maximum possible orbit displacement would be approximately twice as large as that produced by the localized error. In a case of the error affecting the betatron tunes and the isochronism, the effect had to be multiplied by four. The only exception from this analysis was the error in the length of the straight sections. In simulating this effect we increased the length of all the four drifts by 5 mm.

Magnet gap error

The pole tips of the dipole magnets were machined with a tolerance of ± 0.005". The field variation in the dipoles produced by the gap error was calculated as $\delta B/B = -\delta d/d$, where B is the magnetic field in a magnet with the nominal gap size d. The SIR dipoles have a gap of 71.4 mm (2.81"). (For more details on the design of SIR dipoles, see Sections 3.2.1 and 4.2). The horizontal kick produced by this field variation was estimated as

$$\frac{\delta B \cdot l}{B \cdot R} = -\frac{\delta d}{d} \cdot \frac{\pi}{2} = \frac{.01}{2.81} \cdot \frac{\pi}{2} = -5.6 \cdot 10^{-3}$$

where l is the beam-path length in a magnet and R is the beam trajectory curvature. This kick was split into nine equal kicks that were uniformly distributed over one of

the dipoles. The horizontal orbit displacement simulated by DIMAD had a maximum of 9 mm in the magnet opposite to the "defective" magnet.

Magnet length error

The length of the magnets is 27.829" ± 0.03". A horizontal kick produced by the additional field integral due to the length error was estimated as

$$\frac{\delta l}{R} = \frac{0.03}{17.717} = 1.7 \cdot 10^{-3}$$

where R is the beam trajectory curvature. The kick was split in two equal kicks located at the edges of a dipole magnet. The horizontal orbit displacement calculated by DIMAD had a maximum of 2.1 mm in the magnet opposite to the defective magnet.

Vertical shift of a magnet

A vertical shift of the magnets induces a vertical displacement of the closed orbit. Kicks produced by the edges of a dipole were estimated as

$$\delta y' = \frac{y}{F} = \frac{y \cdot \tan(\alpha_e)}{R} = \frac{0.015 \cdot \tan(25.159°)}{17.717} = 3.9 \cdot 10^{-4}$$

where we assumed the vertical alignment error y to be equal to 0.015" and the pole face to be rotated on the angle α_e equal to 25.159°. Simulating the effect, we assumed that both edges had the same displacement y and produced the same kick $\delta y'$. The maximum vertical orbit displacement calculated by DIMAD was 0.7 mm.

Rotation of a magnet around the beam axis

Rotation of a magnet around the beam axis by an angle β results in a non-zero horizontal component of the magnetic field $\delta B_x = B \cdot \sin(\beta)$. The angle β was estimated as $\beta \approx 2\,\delta y/W = 0.03/10$, where we assumed a vertical alignment error, δy to be ± 0.015" at the location of supports and the distance between the supports, W, equal to 10". A vertical kick induced by the horizontal component of the dipole field was estimated as

$$\beta\frac{\pi}{2} = 4.7 \cdot 10^{-3}$$

The kick was split into nine equal kicks that were uniformly distributed over one of the magnets. The vertical orbit displacement calculated by DIMAD had a maximum of 2.6 mm inside of the "defective" magnet.

Stray fields

Steel structures such as racks, shelves, pipes, and elements of the building structure situated in the room and under the room floor produce magnetic fields up to a level of several Gauss at distances of several centimeters from their location. The field produced by these structures substantially decays and becomes weaker than the Earth's magnetic field at distances comparable to a meter. To simulate the effect of stray fields, we assumed that a 2.0-Gauss magnetic field, δB, had a uniform distribution in one of the drifts and was zero in all the others. The kick experienced by a 30 keV deuteron beam from this field was

$$\frac{\delta B \cdot L}{B \cdot R} = \frac{2.0 \cdot 31.383}{800 \cdot 17.717} = 4.4 \cdot 10^{-3}$$

where L is the length of the drift. The kick was split into 22 equal kicks in either horizontal or vertical direction uniformly distributed over the drift. The maximum orbit distortion from DIMAD simulations was 4.2 mm and 3.6 mm for horizontal and vertical kicks respectively.

Tilt of pole tips in a dipole magnet

The manufacturing tolerance of pole tips in the dipole magnets was ± 0.005". This can lead to a total gap variation, δd, of ± 0.01" and a magnetic field gradient of

$$\delta G = \frac{\delta d \cdot B}{d \cdot W} = \frac{.01 \cdot 800}{2.81 \cdot 19.0} = 0.15 \, Gauss/cm$$

if the main field B is 800 Gauss and the pole-tip width W is 190.0 mm (7.48"). According to DIMAD simulations, this additional gradient changes the momentum compaction factor α_p by $-4.3 \cdot 10^{-3}$, ν_x by $2.9 \cdot 10^{-3}$, and ν_y by $-2.0 \cdot 10^{-3}$.

Pole face angle error

The length of the pole tips in the dipoles is $27.829" \pm 0.03"$. The length variation shown in the Figure 3.3 can be interpreted as a rotation of the pole tip by an angle of

$$\delta \alpha_e = \delta(\tan(\alpha_e)) \cdot \cos^2(\alpha_e) = \frac{0.03}{7.48} \cdot \cos^2(25.1°) = 3.3 \cdot 10^{-3}$$

where α_e is the original pole face angle. This additional rotation of the both pole faces by $\delta \alpha_e$ changes the momentum compaction factor α_p by $2.1 \cdot 10^{-3}$, ν_x by $-1.2 \cdot 10^{-3}$, and ν_y by $1.3 \cdot 10^{-3}$.
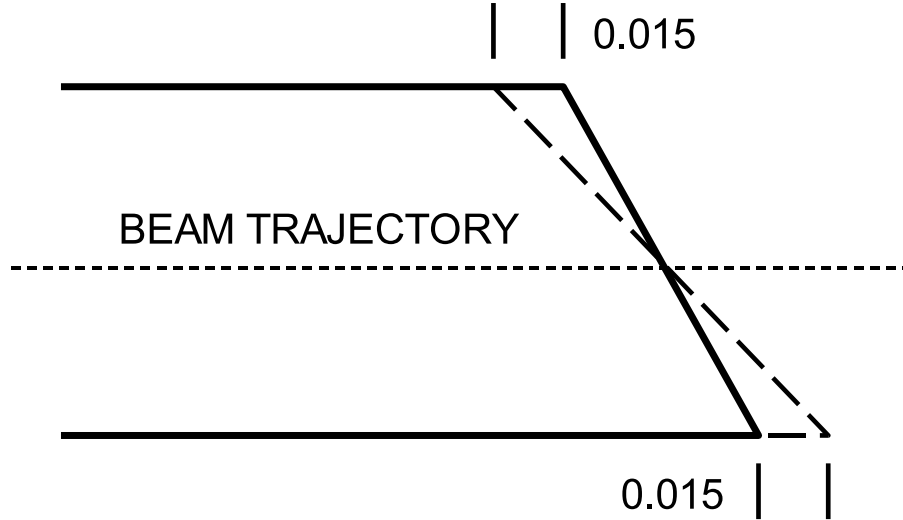
Figure 3.3: An example of rotation of the pole face of a magnet.

Length of straight sections

To estimate the effect of this error we have increased the length of all the four drifts by

5 mm (0.197"). This variation of the drift length caused the momentum compaction

factor, α_p, to change by $-3.3 \cdot 10^{-3}$ and the tunes ν_x and ν_y by $2.8 \cdot 10^{-3}$ and

$2.2 \cdot 10^{-3}$ respectively. An alignment error of 1-2 mm is acceptable. The most likely

source of large errors of this kind is miscalculation of the effective length of the dipoles.

Though this error can be potentially large, it can be compensated by realignment of

the magnets after the magnetic field of the dipoles has been measured.

Summary

Table 3.2 summarizes results of the error analysis. From the table, the magnet gap

error has the largest impact on the horizontal distortion of the closed orbit. The

magnet rotation around the beam axis and stray magnetic fields are the largest factors

generating a vertical orbit distortion. One can estimate the maximum possible error

produced by summing all the contributions given in the fifth column of Table 3.2:

$$\delta x_{orbit} = \pm(18.0 + 2.4 + 8.4) = \pm 28.8 \ mm \tag{3.2}$$

$$\delta y_{orbit} = \pm(1.4 + 5.2 + 7.2) = \pm 13.8 \ mm. \tag{3.3}$$

Expected maximum changes of the momentum compaction factor, and the betatron

tunes are:

$$\delta\alpha_p = \pm(1.72 + 0.84 + 0.33) \cdot 10^{-2} = \pm 2.89 \cdot 10^{-2}, \tag{3.4}$$

$$\delta\nu_x = \pm(1.16 + 0.48 + 0.28) \cdot 10^{-2} = \pm 1.92 \cdot 10^{-2} \tag{3.5}$$

$$\delta\nu_y = \pm(0.8 + 0.52 + 0.22) \cdot 10^{-2} = \pm 1.53 \cdot 10^{-2}. \tag{3.6}$$

Error corection is provided in SIR by correction dipoles and quadrupoles. A

detailed description of these subsystems is given in Section 4.4.

3.1.3 Transverse space charge effects in a KV beam

The incoherent transverse space charge effect decreases the transverse focusing and, as

a result, lowers the betatron tunes increasing the transverse beam size. To quantita-

tively estimate the effect, we assume the Kapchinsky-Vladimirsky (KV) distribution.

The phase space density of the KV beam is given by [19]:

$$f(x, x', y, y') = f_0 \delta\left(\frac{A_x^2}{\epsilon_x} + \frac{A_y^2}{\epsilon_y} - 1\right) \tag{3.7}$$

Table 3.2: Effect of alignment and manufacturing errors on the beam dynamics in SIR

Type of error	Tol.	Effect	Magnitude	Max.Magnitude
Magnet gap	± 0.01"	δx_{orbit}	9 mm	18 mm
Magnet length	± 0.03"	δx_{orbit}	1.2 mm	2.4 mm
Vert. shift	± 0.015"	δy_{orbit}	0.7 mm	1.4 mm
Magnet rot.	± 4.7 mrad	δy_{orbit}	2.6 mm	5.2 mm
Stray fields	± 2 Gauss	δx_{orbit}	4.2 mm	8.4 mm
		δy_{orbit}	3.6 mm	7.2 mm
Pole tip tilt	± 2.7 mrad	$\delta \alpha_p$	$-4.3 \cdot 10^{-3}$	$-1.72 \cdot 10^{-2}$
		$\delta \nu_x$	$2.9 \cdot 10^{-3}$	$1.16 \cdot 10^{-2}$
		$\delta \nu_y$	$-2 \cdot 10^{-3}$	$-0.8 \cdot 10^{-2}$
Pole face rot.	± 3.3 mrad	$\delta \alpha_p$	$2.1 \cdot 10^{-3}$	$0.84 \cdot 10^{-2}$
		$\delta \nu_x$	$-1.2 \cdot 10^{-3}$	$-0.48 \cdot 10^{-2}$
		$\delta \nu_y$	$1.3 \cdot 10^{-3}$	$0.52 \cdot 10^{-2}$
Drift lenght err.	± 5.0 mm	$\delta \alpha_p$	$-3.3 \cdot 10^{-3}$	$-3.3 \cdot 10^{-2}$
		$\delta \nu_x$	$2.8 \cdot 10^{-3}$	$2.8 \cdot 10^{-3}$
		$\delta \nu_y$	$2.2 \cdot 10^{-3}$	$2.2 \cdot 10^{-3}$

where ϵ_x and ϵ_y are x and y emittances of the beam and A_x^2 and A_y^2 are given by

$$A_x = \tilde{\gamma}_x x^2 + 2\tilde{\alpha}_x xx' + \tilde{\beta}_x'^2 \qquad (3.8)$$

$$A_y = \tilde{\gamma}_y y^2 + 2\tilde{\alpha}_y yy' + \tilde{\beta}_y'^2 \qquad (3.9)$$

where $\tilde{\gamma}_x$, $\tilde{\alpha}_x$, $\tilde{\beta}_x$, $\tilde{\gamma}_y$, $\tilde{\alpha}_y$, and $\tilde{\beta}_y$ are Courant-Snyder parameters.

The main attribute of the KV distribution is that any two-dimensional projection results in a uniform particle density. Because the charge density in x-y plane is uniform, the resulting space charge field is linear. If the KV beam is in a channel or a ring that consists of linear field elements, the net force produced by the beam and the external focusing is linear. The quantities A_x and A_y are integrals of motion in the linear field if the motion is stable. Because the distribution depends only on integrals of motion, it does not change in time.

The betatron tunes and the size of the self-consistent, stable distribution can be easily calculated in the linear field. The equations for the beam envelopes X(s) and Y(s) are given by the formulas [19]:

$$X'' + k_{x0}X - \frac{2K}{X + Y} - \frac{\epsilon_x^2}{X^3} = 0 \qquad (3.10)$$

$$Y'' + k_{y0}Y - \frac{2K}{X + Y} - \frac{\epsilon_y^2}{Y^3} = 0 \qquad (3.11)$$

where k_{x0} and k_{y0} are the periodic external focusing functions and K is the generalized perveance. A periodic solution of the system (3.10)-(3.11) yields the size of the stable, self-consistent beam. A numerical solution of the system (3.10-3.11) for a 23.0 keV 50 π·mm·mrad deuteron beam is shown in Figure 3.4. The figure shows the beam

59

envelopes for peak beam currents 0, 40 μA, and 80 μA. Table 3.3 shows the betatron tunes as a function of the peak beam current.

If the injected beam has the transverse dimensions different from the self-consistent solution given by the periodic solution of the system (3.10)-(3.11), the beam size will oscillate. If the deviation from the self-consistent solution is small, we can present the beam size as the sums $X(s) = X_0(s) + \xi(s)$ and $Y(s) = Y_0(s) + \eta(s)$, where $X_0(s)$ and $Y_0(s)$ are the self-consistent solution and ξ and η are small deviations from the self-consistent solutions. The linearized equations for oscillations of the mismatched beam envelopes are [19]:

$$\xi'' + a_1(s)\xi + a_0(s)\eta = 0 \tag{3.12}$$

$$\eta'' + a_2(s)\eta + a_0(s)\xi = 0 \tag{3.13}$$

where a_0, a_1, and a_2 are periodic coefficients that depend on the external focusing, beam current, and X_0 and Y_0:

$$a_0 = \frac{2K}{(X_0 + Y_0)^2} \tag{3.14}$$

$$a_1 = k_{x0} + \frac{3\epsilon^2}{X_0^4} + a_0 \tag{3.15}$$

$$a_2 = k_{y0} + \frac{3\epsilon^2}{Y_0^4} + a_0 \tag{3.16}$$

The System (3.12-3.13) can be unstable for SIR because the betatron phase advance per a period is larger than 90°. The stability analysis of the system (3.12-3.13) is mathematically identical to the stability analysis of the betatron motion in a periodic beam line with linear coupling. Numerical integration of four characteristic

60
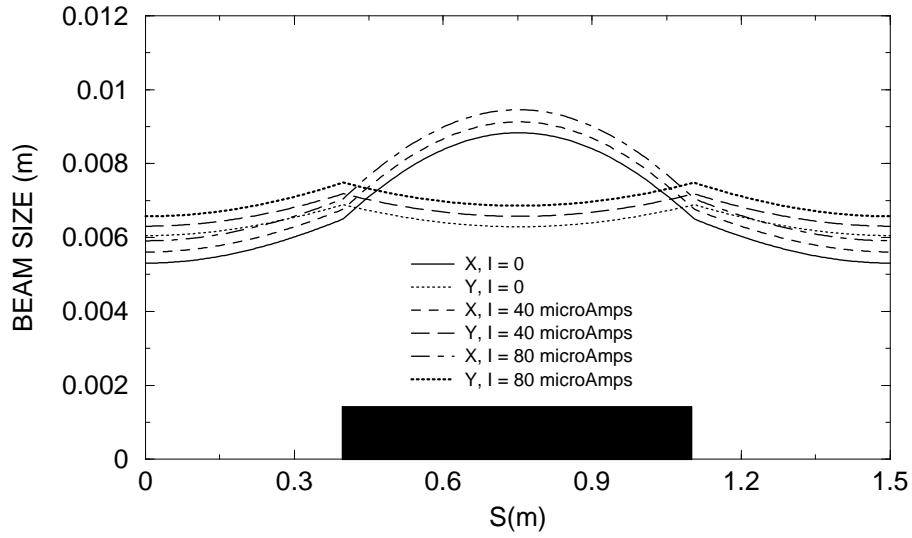
Figure 3.4: The beam envelopes X and Y vs. distance for peak beam currents 0, 40, and 80 μA. The black rectangle schematically shows one of the dipole magnets.

Table 3.3: The betatron tunes as a function of peak beam current.

$I(\mu A)$	ν_x	ν_y	$I(\mu A)$	ν_x	ν_y
0.0	1.142	1.169	**60.0**	0.997	1.031
10.0	1.116	1.145	**70.0**	0.975	1.010
20.0	1.091	1.121	**80.0**	0.954	0.989
30.0	1.067	1.110	**90.0**	0.933	0.969
40.0	1.043	1.075	**100.0**	0.912	0.949
50.0	1.020	1.053	**110.0**	0.889	0.919

functions with initial conditions $(\xi, \xi', \eta, \eta')_{1,2,3,4} = (1,0,0,0),(0,1,0,0),(0,0,1,0),(0,0,0,1)$

yields the matrix of the transformation described by (3.12-3.13). Table 3.4 shows the

absolute value of the four matrix eigenvalues vs. peak beam current for a 23.0 keV 50

π·mm·mrad deuteron beam. From the table, the oscillations of the mismatched beam

are stable ($|\lambda_{1,2,3,4}| = 1$) if peak beam current does not exceed 80 μA. This current

limit is approximately four times higher than the current required for the experiment.

Table 3.4: The absolute value of the four eigen values of the mismatched beam

envelope oscillations vs. peak beam current. The oscillations are stable if the current

is below 90 μA.

$\mathbf{I(\mu A)}$	$|\lambda_1|$	$|\lambda_2|$	$|\lambda_3|$	$|\lambda_4|$
0 - 80	1.0	1.0	1.0	1.0
90	1.0	1.0	1.04	0.96
100	1.0	1.0	1.0	1.0
110	1.04	1.04	0.96	0.96

3.1.4 3D simulation of the space charge effect in SIR (Hard-Edge Model)

To simulate 3D space-charge effects in the hard-edge model a Particle-In-Cell code

was developed. Historically, this code was developed before CYCO. In simulating

the beam dynamics in the ring, the code calculated coordinates of particles relatively

to an equilibrium particle, an imaginary particle with a given energy which moved

in the ring on a closed, equilibrium orbit. The position of other particles in the six

dimensional phase space was given by x, x', y, y' (displacements and angles relatively

to the equilibrium orbit), $\delta p/p$, and s, (the mometum deviation and the position along the equilibrium orbit). At each integration step, particles were propagated along the equilibrium orbit according to the formula

$$ds = ds_0 \cdot (1 - \frac{x}{\rho} + \frac{1}{\gamma^2}\frac{\delta p}{p}) \qquad (3.17)$$

where ds_0 is a longitudinal step of the equilibrium particle, ρ is curvature of the equilibrium trajectory, and γ is the relativistic factor. During the step transverse coordinates of the particles were transformed according to

$$\begin{bmatrix} x \\ x' \\ y \\ y' \end{bmatrix}_{s+ds} = M(s, s+ds) \begin{bmatrix} x \\ x' \\ y \\ y' \end{bmatrix}_{s} \qquad (3.18)$$

where $M(s, s + ds)$ is a 4x4 transfer matrix between s and $s + ds$.

The effect of the space charge force was included as an integrated kick (an abrupt change of x', y', and $\delta p/p$) at the end of every integration step. The field of the beam was calculated by a fast field solver developed specifically for the code and based on Fast Fourier Transformations.

Figures 3.5 and 3.6 shows an example of simulation of the dynamics of a 20 keV, 25 μA H_2^+ bunch in SIR. The bunch initially had an almost rectangular longitudinal distribution with the length of 10.5 cm. As shown in Figure 3.5, the vortex motion causes the edges of the bunch to bend. As the beam continues circulating in the ring, the disturbance propagates into the bunch and the bunch breaks into small round

63

clusters. Particles within each cluster are involved in the vortex motion around the cluster center. Figure 3.6 shows the longitudinal charge density profile of the beam after 0 (initial distribution), 5, 10, and 15 turns. The difference between the maximum energy in the bunch and the minimum energy in the bunch grows from from $5 \cdot 10^{-4}$ to almost 10% in less than 15 turns.

3.2 Beam dynamics simulations in a calculated 3D magnetic field

3.2.1 POISSON and TOSCA models

Beam dynamics simulations made at early stages of the project and presented in Section 3.1.4 have indicated a large beam energy spread induced by the coherent longitudinal-radial space charge effect. Using programs POISSON [23] and TOSCA [24], we have optimized the SIR dipole magnets so that the ring would be able to accept a 50 π·mm·mrad beam with the 10% energy spread and ± 20.0 mm closed orbit distortion.

POISSON model

As mentioned in Section 3.1.1, the mid-radius of the dipole magnets was set to 450.0 mm (17.717"). The size of the vertical gap in the dipoles was set to 71.4 mm (2.81"). This gap was large enough to accommodate a two-inch tall vacuum chamber and two quadrupole corrector coils described in Section 4.4. To calculate the magnetic field we have used the B-H curve of 1003 steel instead of 1010 steel actually used for the
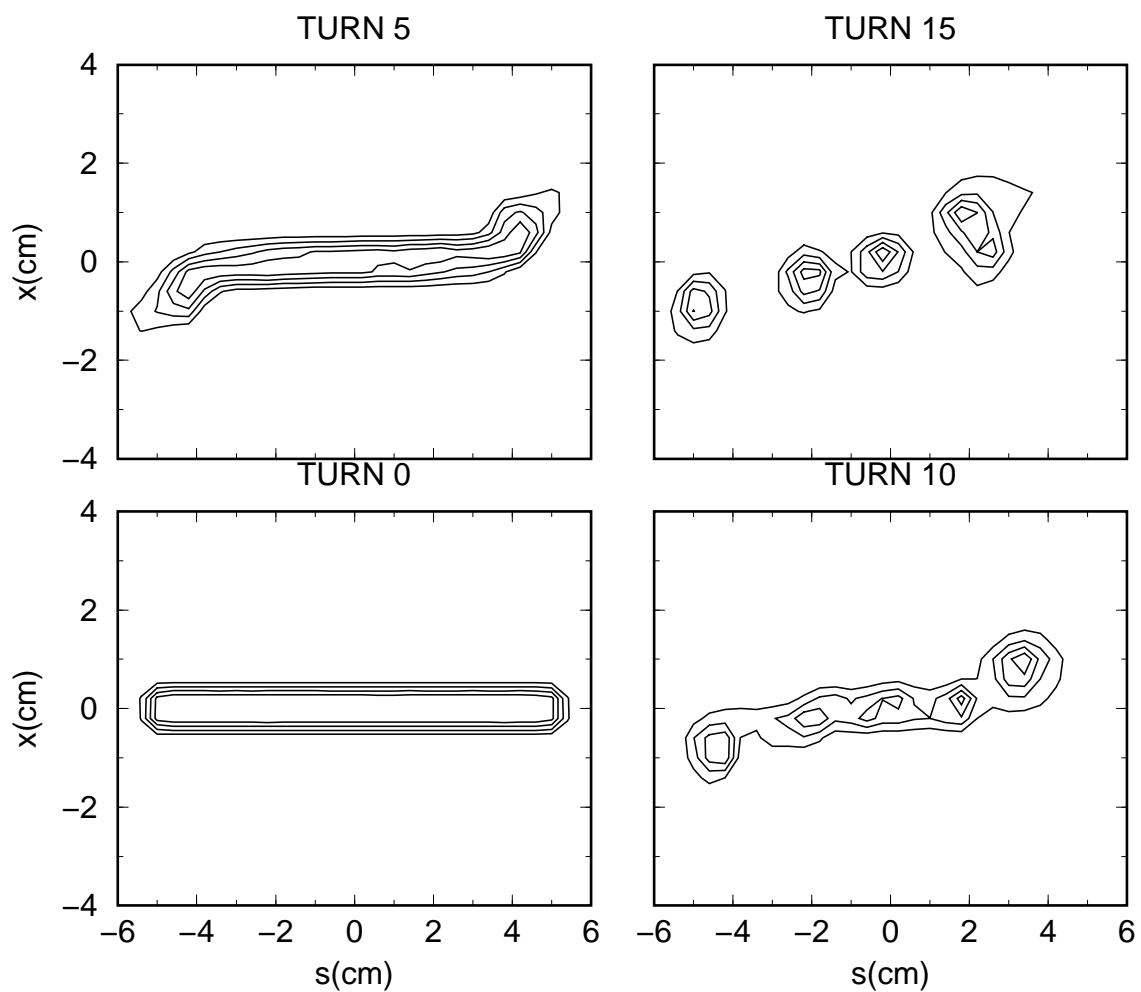
Figure 3.5: Median-plane charge density contour plot of the 20 keV, 25 μA H_2^+ bunch in SIR after 0 (initial distribution), 5, 10, and 15 turns.
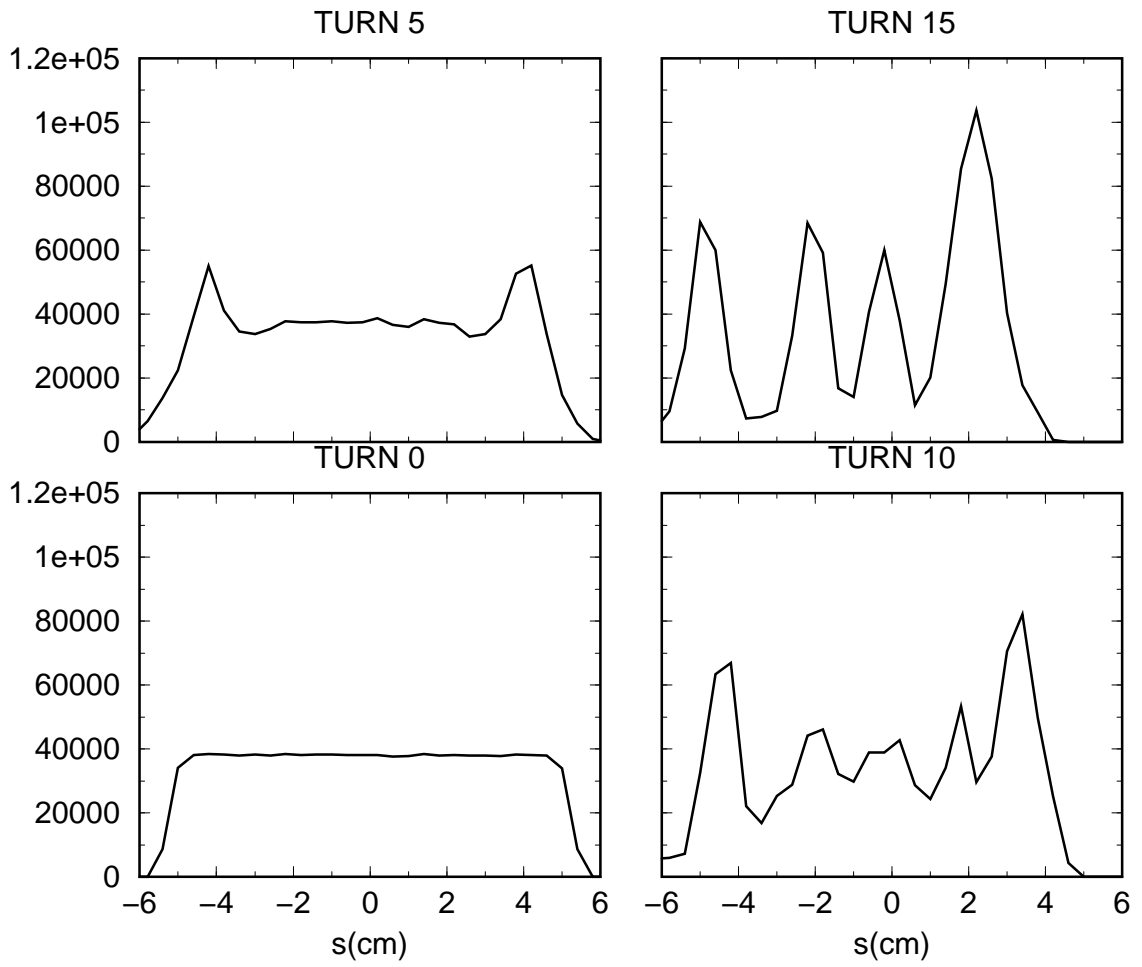
Figure 3.6: The longitudinal charge density profile of the 20 keV, 25 μA H_2^+ bunch in SIR after 0 (initial distribution), 5, 10, and 15 turns. The charge density is in arbitrary units.

magnets because the B-H curve of 1010 steel was not available at the time of the calculations. However, the measurement of the magnetic field described in Section 4.3 has shown that both the strength and the profile of the measured field were very close to predicted values.

The width of the flat field region necessary to accommodate the beam with the parameters mentioned on page 64 was estimated as

$$\eta \frac{\delta p}{p} + 2\sqrt{\beta\epsilon} + \delta x = 1.0 \cdot 0.05 + 2\sqrt{1.6 \cdot 5 \cdot 10^{-5}} + 2 \cdot 0.02 =$$

$$0.05 + 0.018 + .04 = 0.108 \text{ m} \tag{3.19}$$

where $\eta(\delta p/p)$ is the beam size due to the energy spread, $\sqrt{\beta\epsilon}$ is the betatron size, and δx is the beam centering error. The values of β and η were chosen from Figure 3.2.

Using POISSON, we have optimized the pole tip shape so that the size of the flat field region would be larger than 110 mm. Figure 3.7 shows the final, optimized configuration of the pole tips. The pole tip was 190 mm wide. Two bumps provided on both sides of the pole tips further increased the flat field region. Figure 3.8 shows magnetic field profile calculated by POISSON. According to Figure 3.8 the magnetic field changed by 0.05% in a region of 115 mm (450 ± 57.5 mm or 17.717 ± 2.26").

TOSCA model

To calculate a 3D magnetic field that includes edge effects we have used the program TOSCA. A 1/8 of SIR or one half of a drift between magnets and one half of a dipole
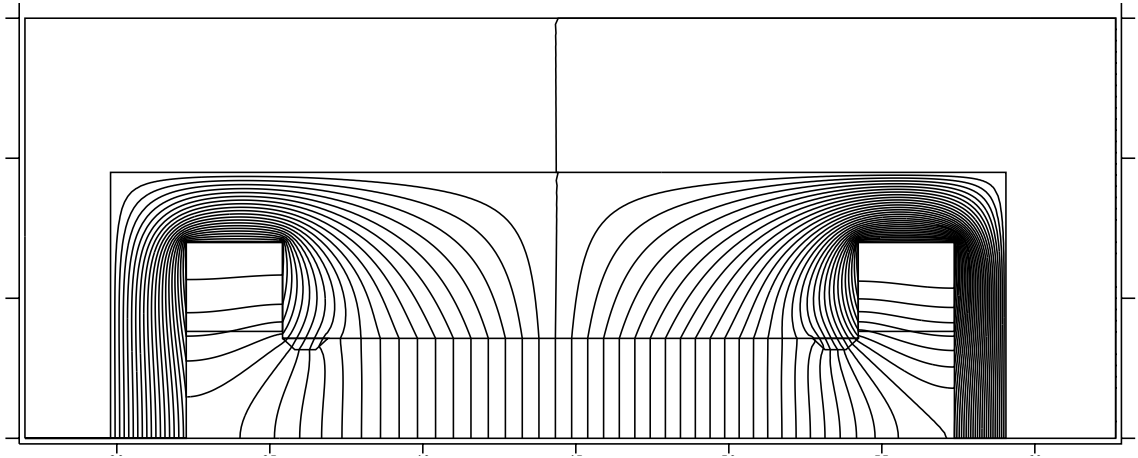
Figure 3.7: POISSON model of SIR dipoles.
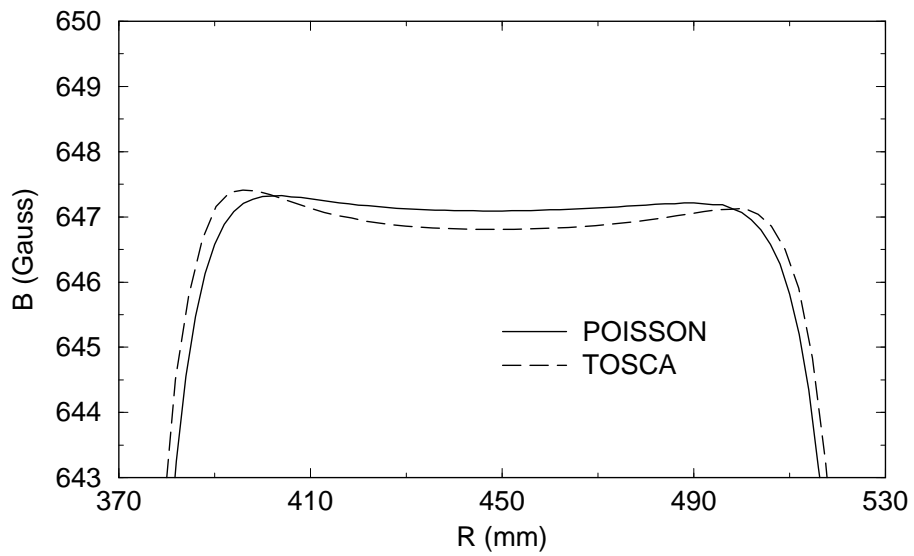
Figure 3.8: Magnetic field in the median plane of the SIR dipoles, generated by POISSON and TOSCA. The TOSCA field was taken in the middle of the magnets. Only the top 1% of the field is shown.

magnet was used for field calculations. The code GENSPEO [25], developed at the NSCL, has been used to calculate the optical functions, bare tunes, and isochronism in of SIR.

As expected, the betatron tunes were too low when we used the drift length and the edge angle calculated from the hard-edge model. The "softer" edge of the calculated field causes the betatron tunes, especially the vertical betatron frequency, to decrease. To increase the betatron tunes it was necessary to increase the drift length and the edge angle to 948.1 mm and 26.0° respectively. Figure 3.8 shows the magnetic field at the center of the magnet. Figure 3.9 shows a contour plot of the magnetic field calculated by TOSCA. The field that was also used for all other simulations presented in this section has a maximum value of 647 Gauss. This field level was an arbitrary choice and could be changed to any other value with the only limitation that the beam energy in the magnetic field must be equal or lower than 30 keV. The maximum beam energy is limited by the maximum output voltage of the ion source HV power supply.

3.2.2   Single-particle beam dynamics in the TOSCA field

The field map used in the simulations was generated as described in the last paragraph of Section 3.2.1 and had a maximum of 647 Gauss. As was mentioned before, we have used the code GENSPEO to calculate the optical functions, bare tunes, and isochronism in the field. Figure 3.10 shows the optical functions for a deuteron beam with a kinetic energy of 23.5 keV. Bare tunes vs. beam energy are presented in Figure

69
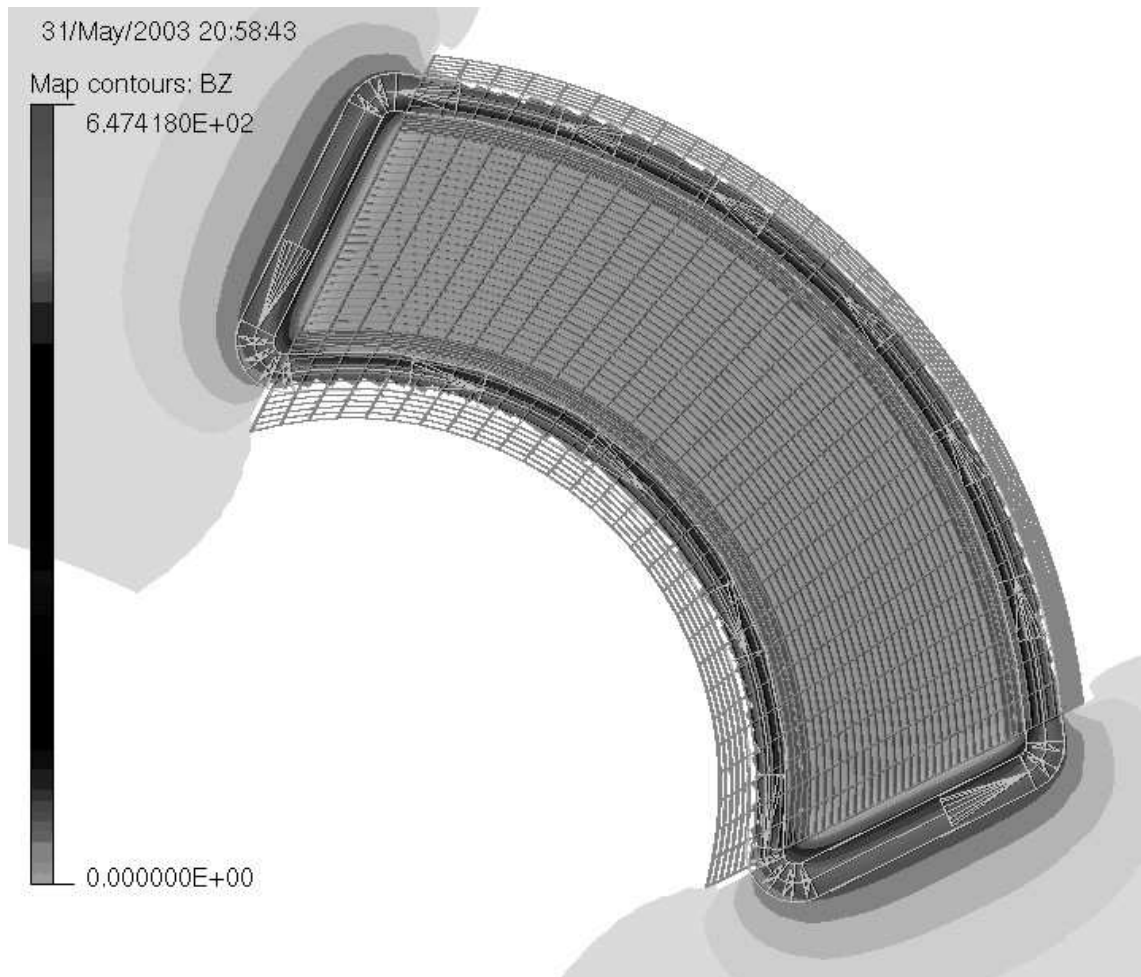
Figure 3.9: Contour plot of the median plane magnetic field generated by TOSCA. The meshed TOSCA model of the magnet with coils is also shown. Only a half of the magnet was used in the calculations.

3.11. The bare betatron tunes ν_x and ν_y of the mono-energetic 23.5 keV deuteron beam are 1.143 and 1.128 respectively. From the multi-particle simulations presented in Sections 3.1.4 and 3.2.3, the energy spread within the injected beam quickly grows from zero to almost ± 1.0 keV. This causes the radial and vertical tune spreads to grow to ± 0.004 and ± 0.01 respectively.

Chromatism of the betatron tunes can be reduced by means of sextupoles. Appendix C describes an example of partial compensation of tune chromatism by a single sextupole and discusses other possible sextupole schemes. Currently, we plan to use no sextupole components in the initial stage of the project. They can later be installed in the ring, depending on first experimental results.

Figure 3.12 shows the particle longitudinal lag per turn behind a reference ion with a kinetic energy of 23.5 keV vs. particle energy. As follows from the picture, the ring is almost ideally isochronous within the 23.5 ± 0.5 keV ($\pm 2.13\%$) range. Particles whose energy deviates by ± 1.0 keV ($\pm 4.26\%$) lag behind the reference particle at the rate of approximately 1.0 mm/turn. It is worth noting that the edge field effect has a strong impact on the shape of the lag curve. The edge magnetic field extends further out at the center of the pole tip than at the sides, closer to the return yoke. Thus, the field integral differs for particles entering a dipole magnet at different radii.

To estimate the size of the dynamic aperture in SIR we have developed a short code that calculates trajectories of ions in a realistic 3D magnetic field map generated by TOSCA. The code solved the complete system of the equations of motion of an ion in the magnetic field using the classical $4^t h$ order Runge-Kutta method. The

71
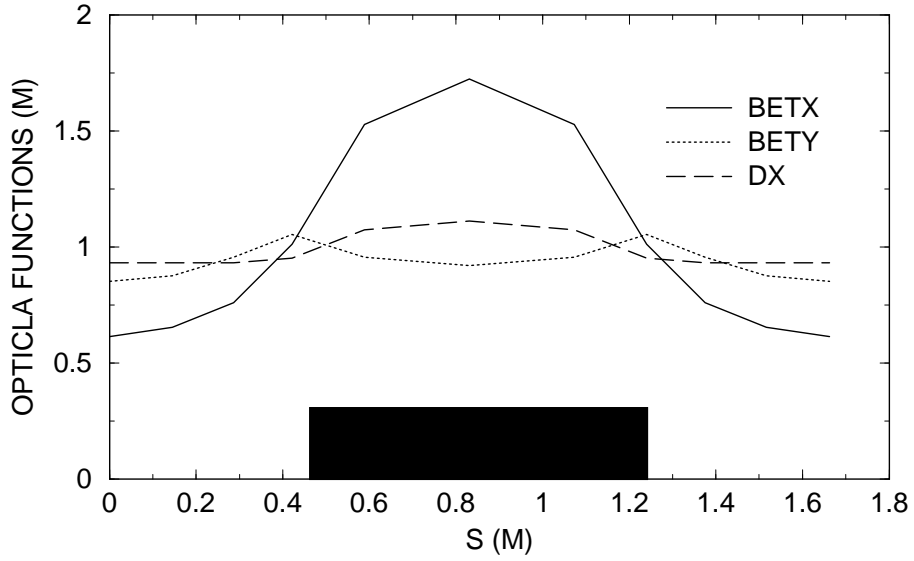
Figure 3.10: The optical functions for a single period of SIR vs. distance calculated in the field generated by TOSCA. The solid rectangle schematically shows one of the 90° dipole magnets.
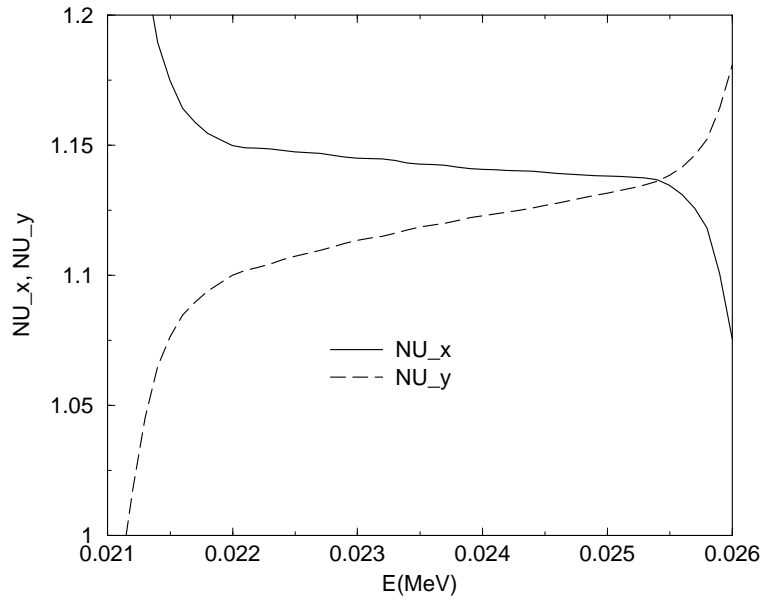
Figure 3.11: Bare tunes calculated in the TOSCA field vs. energy.
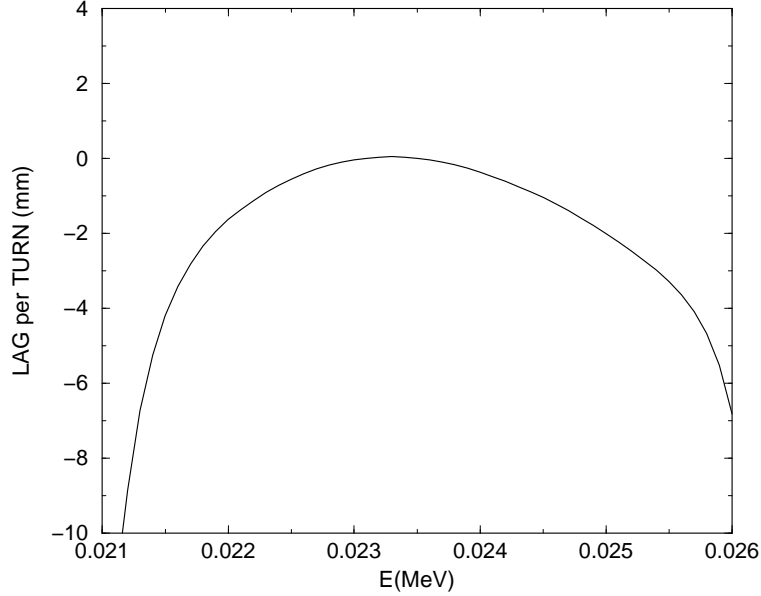
Figure 3.12: Particle lag per turn behind a reference ion of a kinetic energy of 23.5 keV vs. particle energy.

number of turns was pre-set to 1023. This number of turns exceeds the expected beam lifetime, determined by the residual gas pressure, by a factor of 3.5. (To find out more about vacuum and beam lifetime in SIR, see 4.7).

Figure 3.13 shows the X-X' phase space plot at the mid- point of a drift between two dipoles. From the picture, deuterons with a kinetic energy of 23.5 keV are stable inside of a phase space area of a size of 35x55 π·mm·mrad. The size of the stable region for particles with an energy deviation of ± 1.0 keV ($\pm 4.26\%$) is still larger than 26x40 π·mm·mrad.

Figure 3.14 shows the Y-Y' (vertical) phase space plot at the mid-point between the magnets. The size of the stable Y-Y' region is only weakly dependent on energy and is approximately equal to 25x30 π·mm·mrad.

Both the radial and vertical stable regions are sufficient to easily accommodate

73
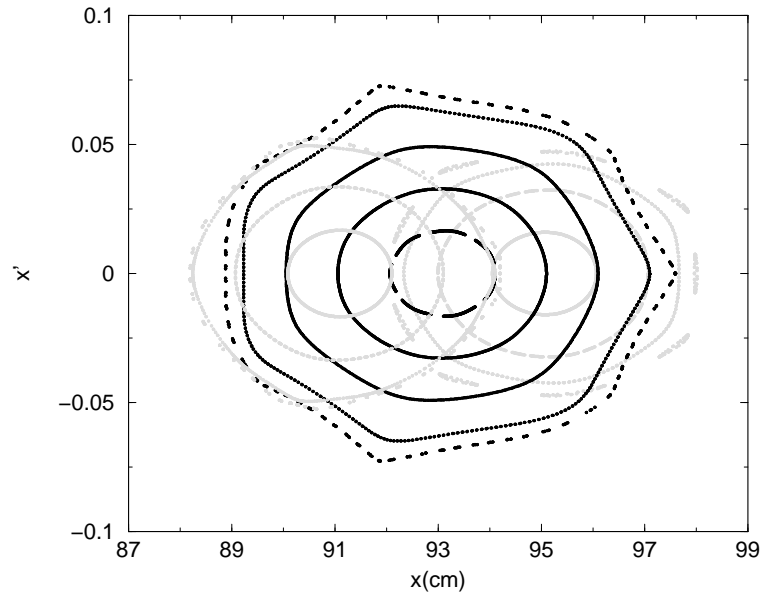
Figure 3.13: X-X' phase space plot at the mid-point of a drift between magnets. Trajectory with an energy of 23.5 keV is shown in black. Points of trajectories with energies of 22.5 and 24.5 keV are shown in gray.
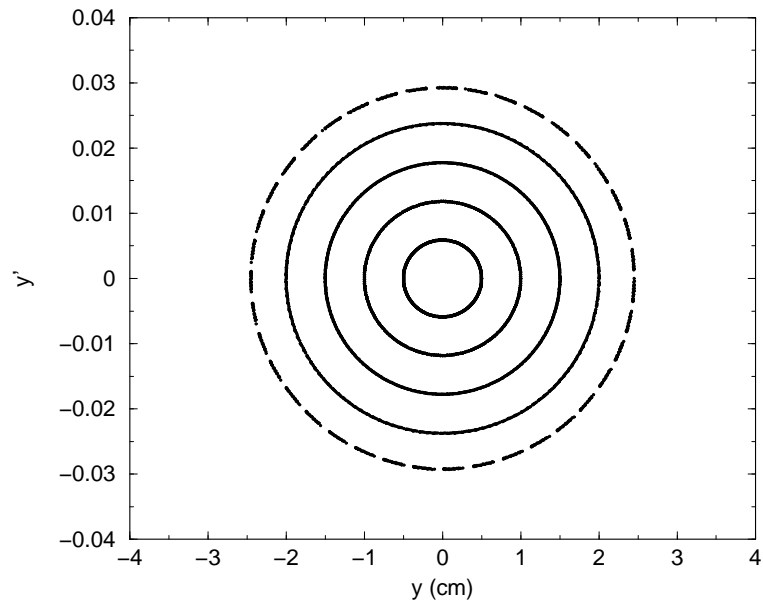
Figure 3.14: Y-Y' phase space plot at the mid-point of a drift between magnets for a beam energy of 23.5 keV

the beam from our ion source that has the emittance of less than 50 π·mm·mrad. (To find out more about the ion source and the beam emittance measurement system, see [26],[27],[28]).

3.2.3 Simulation of space charge effects in a TOSCA field

We used the code CYCO to simulate the beam dynamics of the SIR. The beam dynamics was simulated assuming a magnetic field of 647 Gauss (see section 3.2.1). The initial beam energy of the H_2^+ beam was 23.5 keV in all the simulations presented below. The integration step was equal to 1° what resulted in 360 integration steps per turn. The number of space charge field calculations per turn, N_e, was 180. The energy spread was zero.

We studied three cases:

- CASE 1: The beam emittance of the beam, ϵ, was equal to 50 $\pi \cdot mm \cdot mrad$. This emittance yielded the horizontal and vertical beam sizes in the mid-point between the dipole magnets equal to 11.2 and 12.8 mm respectively. The temporal length of the beam, t_b, was 200 nsec or approximately 30 cm for a beam energy of 23.5 keV.

- CASE 2: ϵ=12.5 $\pi \cdot mm \cdot mrad$, t_b=200 nsec.

- CASE 3: ϵ=500 $\pi \cdot mm \cdot mrad$, t_b=600 nsec corresponding to approximately 90 cm or 1/7 of the ring.

The initial linear charge density of the bunch had a rectangular shape in all the cases. The number of particles in cases one and three was 10^5 and $3 \cdot 10^5$ in the second

75

case. The distance between the mesh nodes of the grid used for the space charge field calculations was 2 and 4 mm in the first and the third cases and 1 and 2 mm in the second case. (For more details on the choice of the mesh step size, see section 2.3.1). The beam peak current was 20 μA in all the cases. The total charge was $4 \cdot 10^{-12}$ C for the 200-nsec-long bunch and $1.2 \cdot 10^{-11}$ C for the 600-nsec-long bunch. In the first and the third cases, we did not adjust the initial transverse size to the size of the self-consistent solution. According to section 3.1.3, the transverse size of the beam with a peak current of 20 μA is only 3% larger than the size of the matched beam with zero current, but we did match the transverse beam size for the beam with the smaller emittance. In all the simulations we tracked the beam for twenty turns. We assumed that the beam life time was infinitely long.

Case 1: $\epsilon = 50 \; \pi \cdot mm \cdot mrad$, $t_b = 200$ nsec.

Figure 3.15 shows the simulated beam distribution at turns 0 (initial distribution), 4, 8, 12, 16, and 20. Figure 3.16 shows the longitudinal bunch distribution for the same turns. Figure 3.17 shows how the transverse bunch distribution changes with the number of turn. Figure 3.18 shows the beam energy distribution for turns 8,12 ans 20. Finally, figure 3.19 shows the beam energy spread vs. turn number.

Case 2: $\epsilon = 12.5 \; \pi \cdot mm \cdot mrad$, $t_b = 200$ nsec.

Figure 3.20 shows the simulated beam distribution at turns 0 (initial distribution), 4, 8, 12, 16, and 20. Figure 3.21 shows the longitudinal bunch distribution after twenty turns. Figure 3.22 shows the transverse bunch distribution after 20 turns. Figure
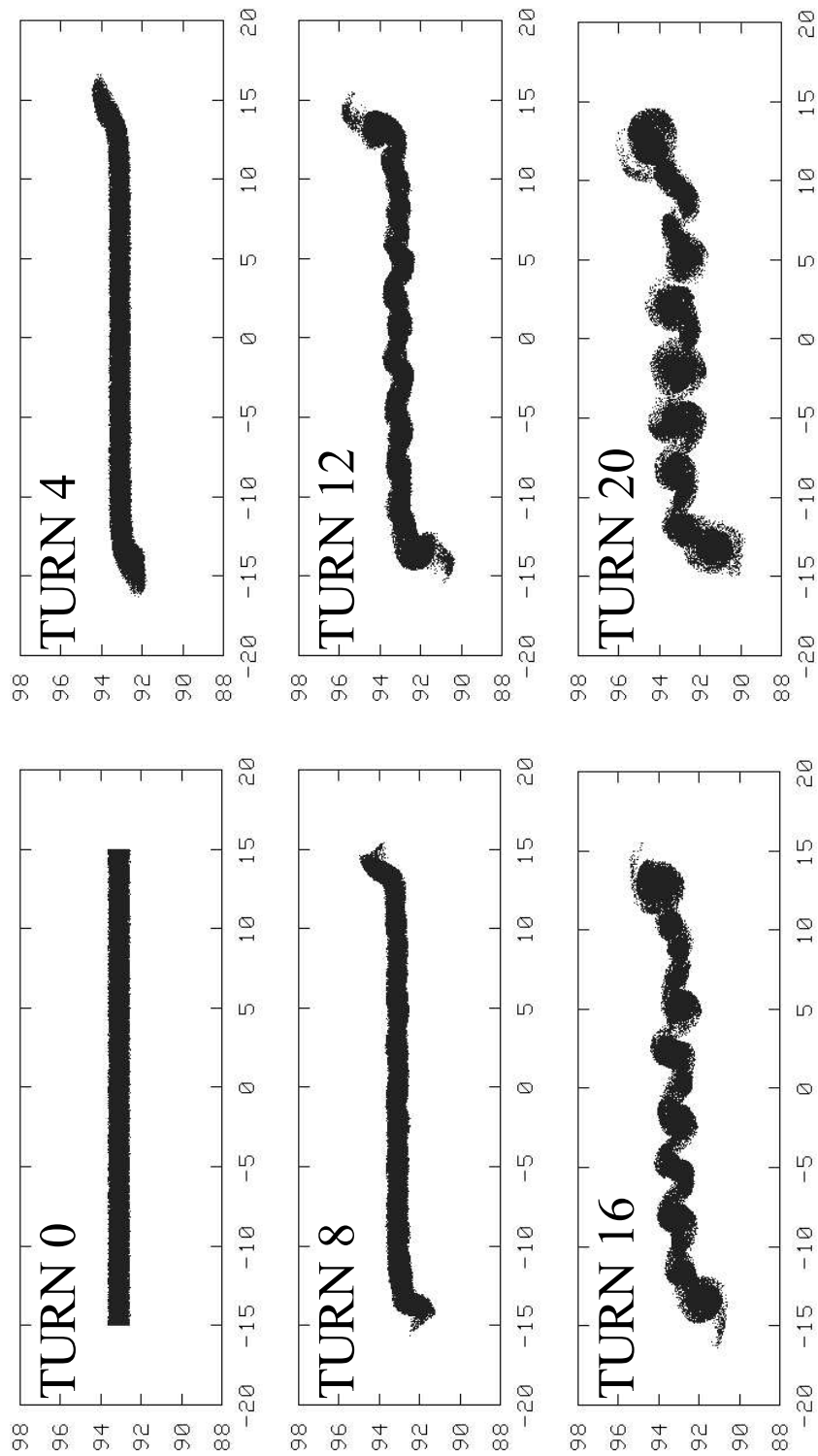
Figure 3.15: Simulated beam distribution projected on the median plane (top view of the beam). The pictures show the bunch in a straight section between two dipole magnets after 0 (initial distribution), 4, 8, 12, 16, and 20 turns.
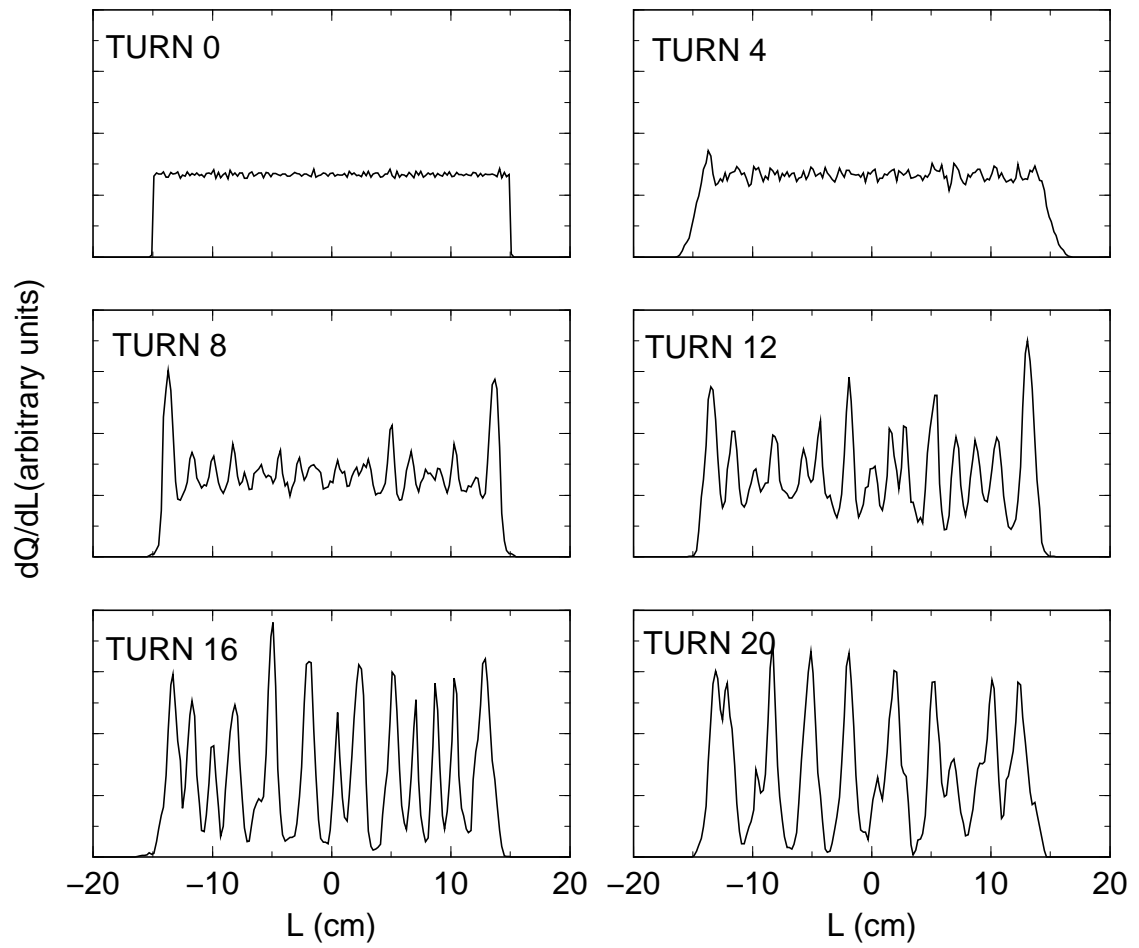
Figure 3.16: Simulated longitudinal charge distribution of the bunch after 0 (initial distribution), 4, 8, 12, 16, and 20 turns.
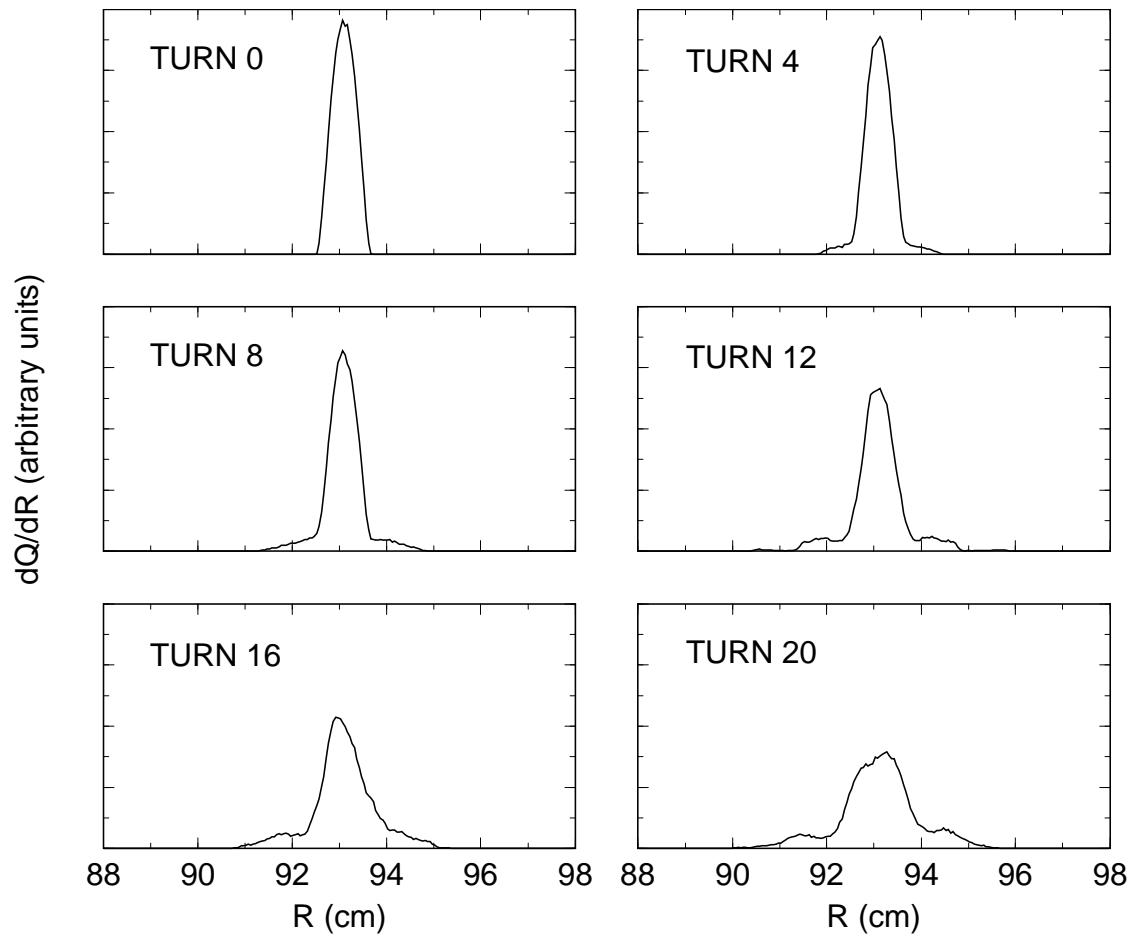
Figure 3.17: Simulated radial distribution of the bunch after various number of revolutions.
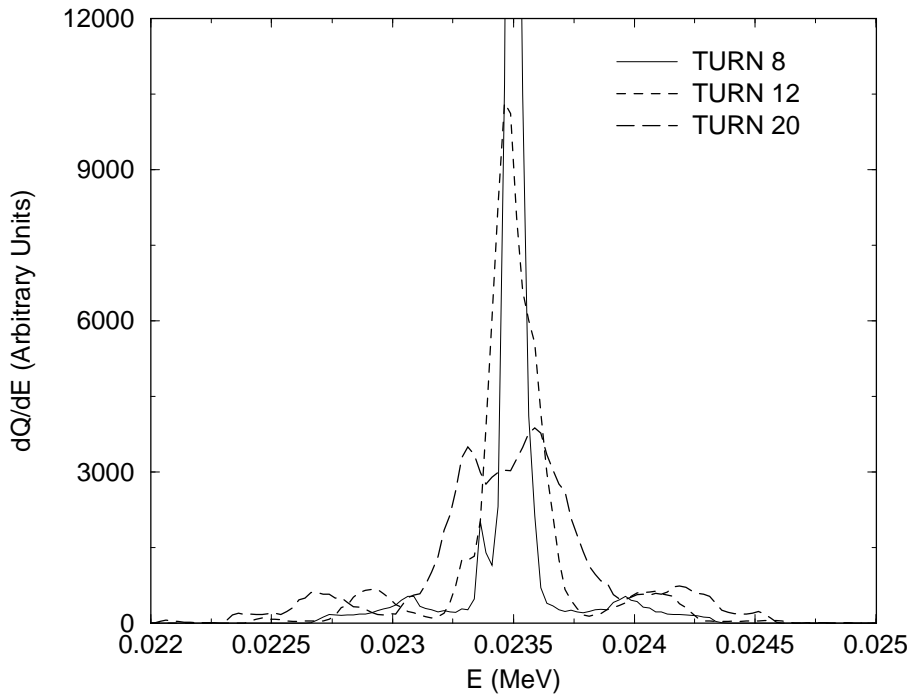
Figure 3.18: Energy distribution within the bunch after 8,12, and 20 turns. The distribution of the 8th is truncated in the figure.
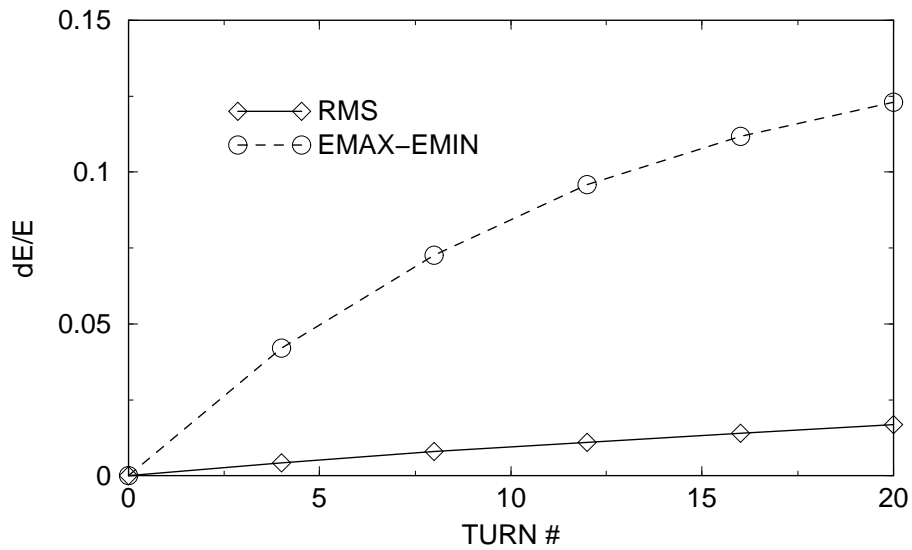
Figure 3.19: The RMS and full energy spread within the beam vs. turn number. The full energy spread was calculated as the difference between the maximum energy in the bunch and the minimum energy in the bunch.

3.23 shows the beam energy distribution after 20 turns. For a comparison, the three previous figures show the bunch distribution for the beam with the emittance equal to 50 $\pi \cdot mm \cdot mrad$. Figure 3.19 shows the beam energy spread vs. turn number.

Case 3: ϵ=**50** $\pi \cdot mm \cdot mrad$**,** t_b=**600 nsec.**

Figure 3.25 shows the simulated beam distribution at turns 0 (initial distribution), 4, 8, 12, 16, and 20. Figure 3.26 shows the longitudinal bunch distribution after twenty turns. Figure 3.22 shows the transverse bunch distribution after 20 turns along with the radial distribution of the 200-nsec-long beam with the same emittance. Figure 3.23 shows the beam energy distribution after 20 turns. For a comparison, the last figure also shows the energy distribution within the 200-nsec-long bunch. Figure 3.19 shows the beam energy spread within the 600-nsec-long bunch vs. turn number.

3.2.4   Summary of the simulation results

The simulations show that the space charge force causes the beam to break up. The break-up is accompanied by a fast growth of the energy spread and the beam size. The space charge force strongly deforms the head and tail of the bunch within several turns. Because the space charge field reaches its maximum value at the edges of the bunch, the head and tail are affected by the space charge force more than the inner parts of the beam. The deformed edges of the bunch create wings in the radial and energy distributions of the beam particles. Although the wings are relatively weak, their size can exceed the RMS size of the beam by a significant factor.

In the first several turns, the beam with the 12.5 $\pi \cdot mm \cdot mrad$ emittance was
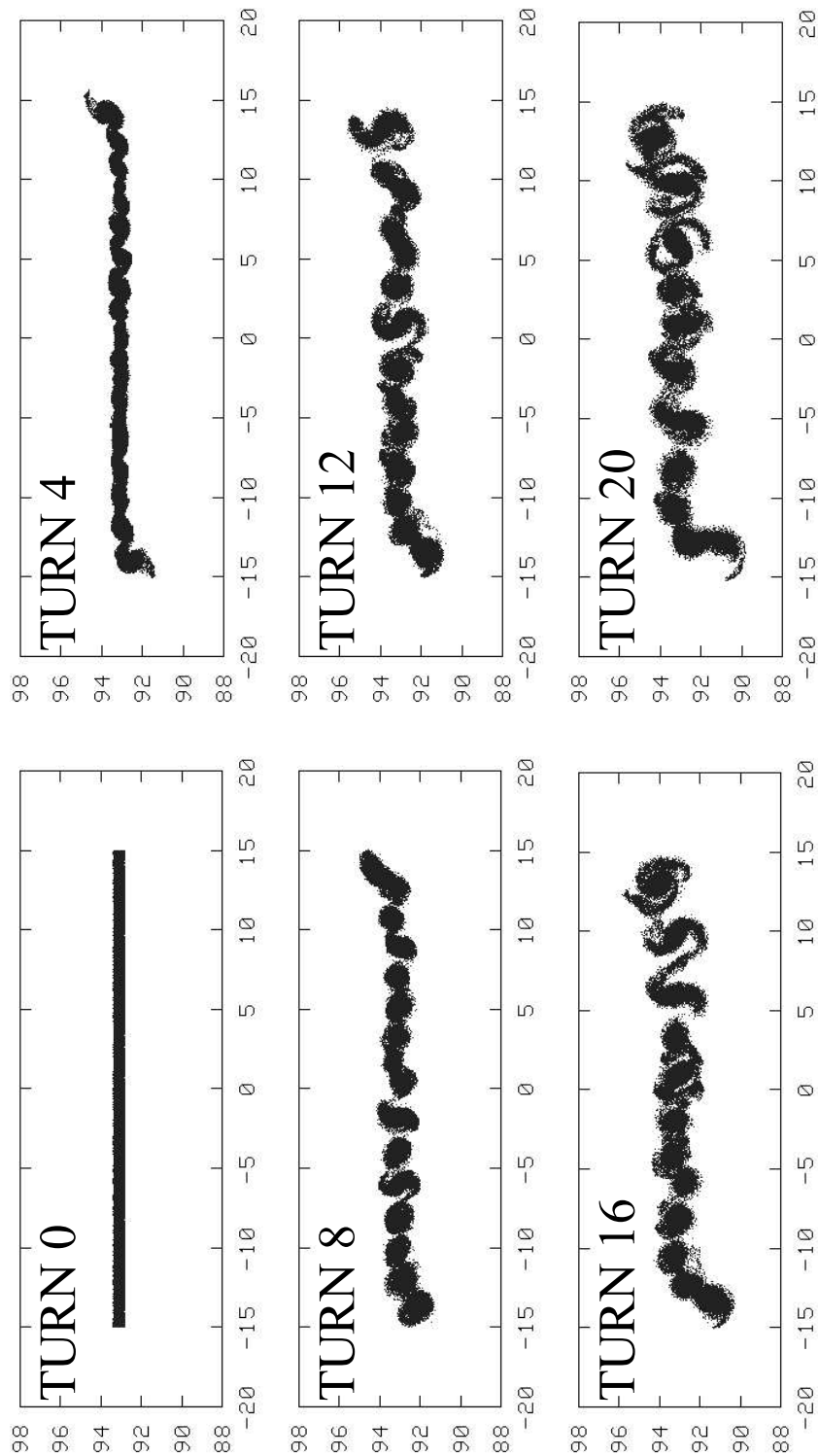
Figure 3.20: Simulated distribution of the beam with the emittance equal to 12.5 $\pi \cdot mm \cdot mrad$. The pictures show the bunch in a straight section between two dipole magnets after 0 (initial distribution), 4, 8, 12, 16, and 20 turns.
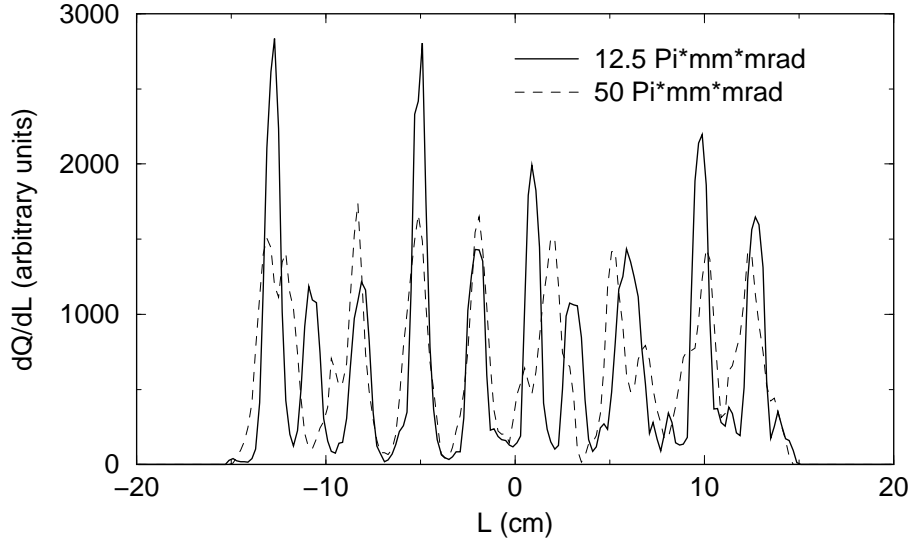
Figure 3.21: Simulated longitudinal charge distribution after 20 turns. The solid and dashed curves give the distribution of the beam with emittances of 12.5 and 50 $\pi \cdot mm \cdot mrad$ respectively.
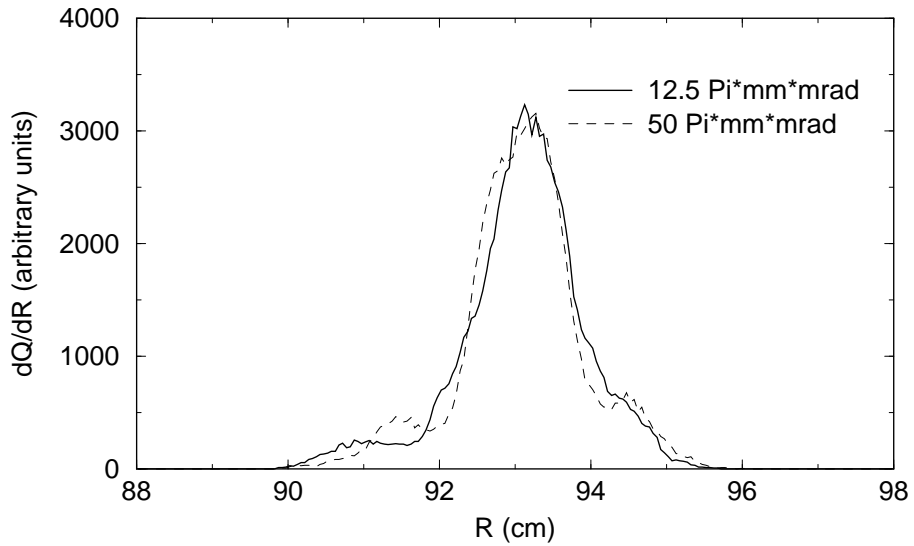
Figure 3.22: Simulated radial distribution of the beam with 12.5 $\pi \cdot mm \cdot mrad$ emittance (solid line) after 20 turns. The dashed curve shows the distribution of the beam with the 50 $\pi \cdot mm \cdot mrad$ emittance.
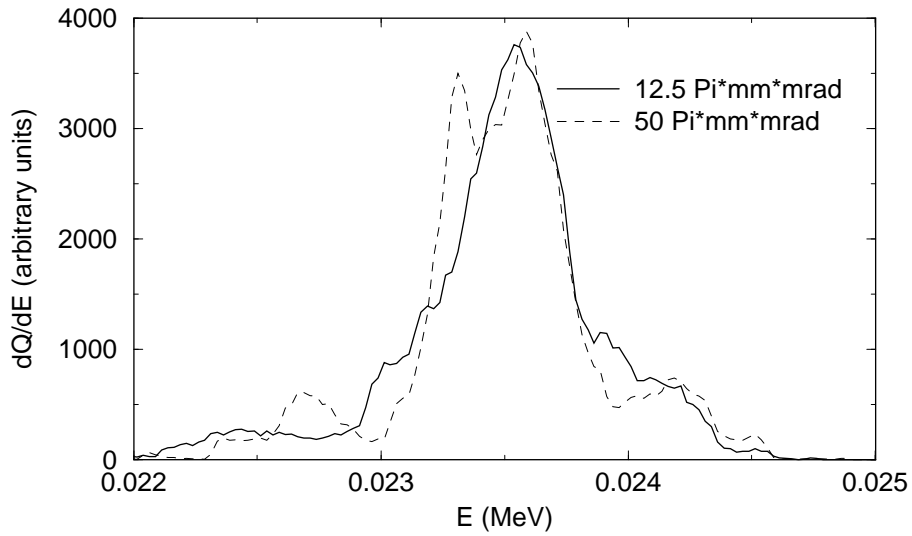
Figure 3.23: Simulated energy distribution within the bunch after twenty turns. The solid and dashed curves give the distribution of the beam with emittances of 12.5 and 50 $\pi \cdot mm \cdot mrad$.
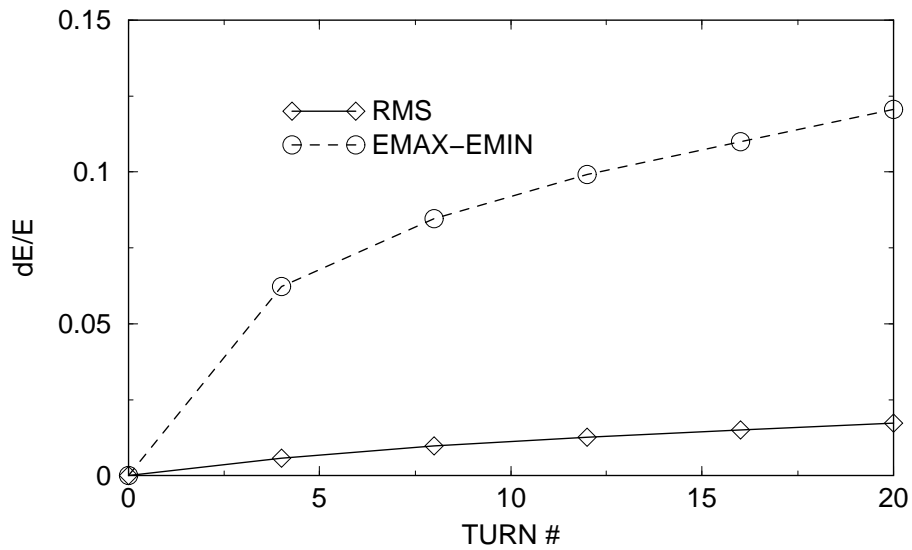
Figure 3.24: The RMS and the full energy spread within the beam vs. turn number. The beam emittance was equal to 12.5 $\pi \cdot mm \cdot mrad$. The full energy spread was calculated as the difference between the maximum energy in the bunch and the minimum energy in the bunch.

84
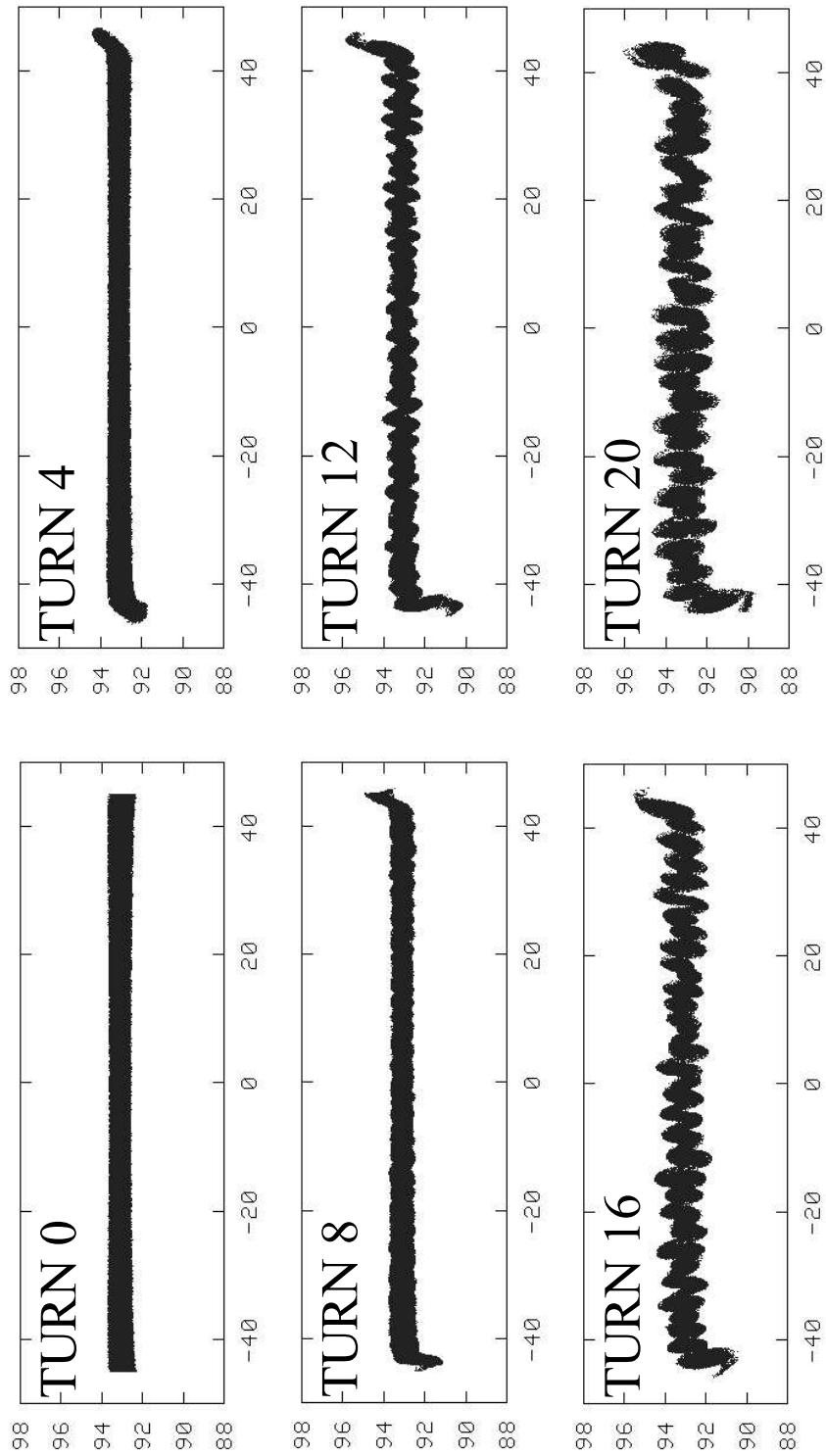
Figure 3.25: Simulated distribution of the 600-nsec-long bunch. The emittance of the bunch was equal to 50 $\pi \cdot mm \cdot mrad$. The pictures show the bunch in a straight section between two dipole magnets after 4,8,12,16, and 20 turns.
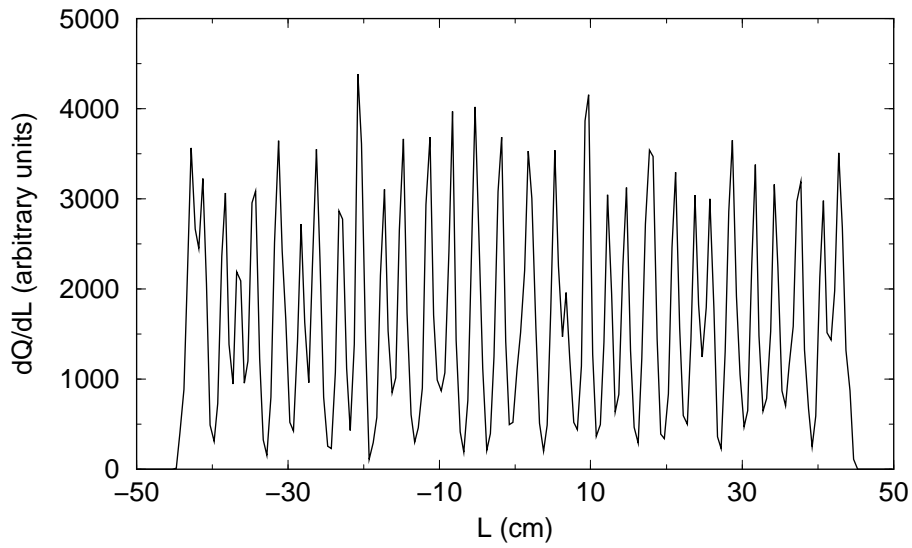
Figure 3.26: Simulated longitudinal charge distribution of the 600-nsec-long bunch after 20 turns.
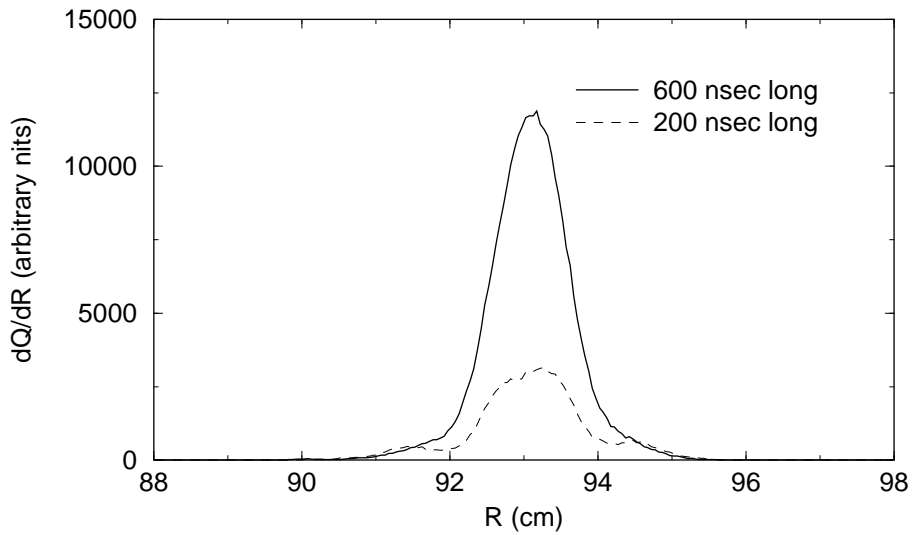
Figure 3.27: Simulated radial distribution of the 600-nsec-long beam with 50 $\pi \cdot mm \cdot mrad$ emittance (solid line) after 20 turns. The dashed curve shows the distribution of the 200-nsec-long bunch with the 50 $\pi \cdot mm \cdot mrad$ emittance.
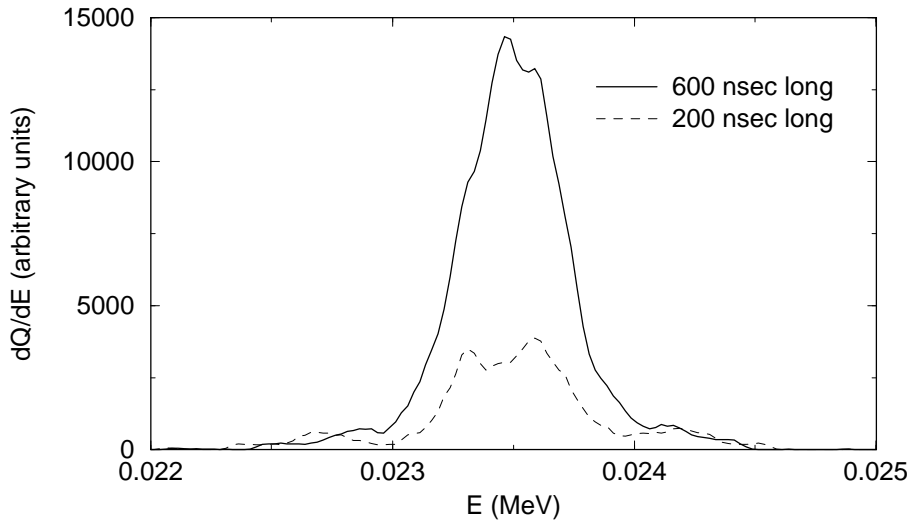
Figure 3.28: Simulated energy distribution within the 600-nsec-long beam after 20 turns. The dashed curve shows the distribution of the 200-nsec-long bunch with the $50\ \pi \cdot mm \cdot mrad$ emittance.
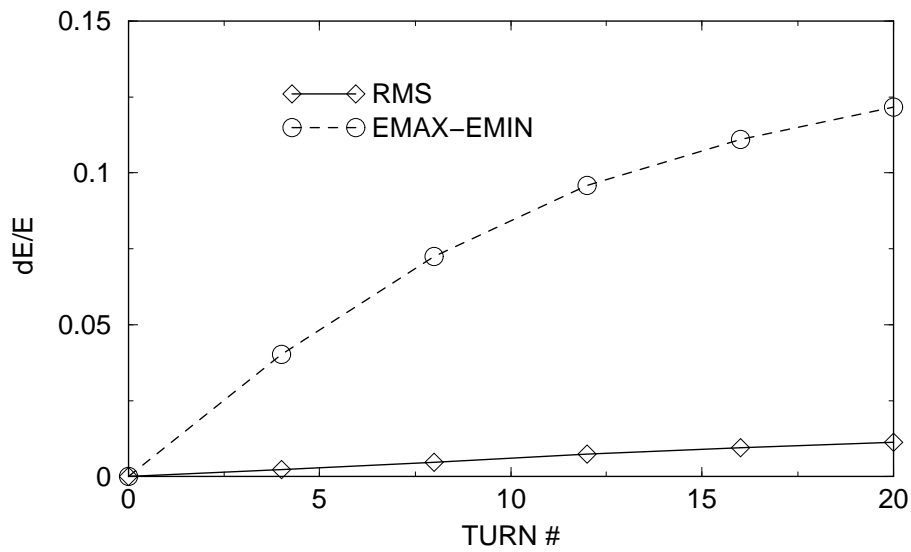
Figure 3.29: The RMS and the full energy spread of the 600-nsec-long bunch vs. turn number. The full energy spread was calculated as the difference between the maximum energy in the bunch and the minimum energy in the bunch.

braking into clusters at a faster rate than the beam with the emittance equal to 50 $\pi \cdot mm \cdot mrad$. The energy spread of the beam with the smaller emittance was also growing faster. However, the bunches had similar energy and radial distributions after 20 turns.

The behavior of the 600-nsec-long bunch was similar to that of the 200-nsec-long bunch. The beam became "unstable" and started braking in to clusters simultaneously everywhere along the bunch. The reason that causes the break-up inside of the (almost) uniform bunch is still unclear and requires additional numerical and experimental studies. One of the possible explanations can be statistical fluctuations of the particle density and related fluctuations of the space charge field within the bunch.

Chapter 4

SIR DESIGN

A simplified schematic view of SIR and its injection line, a list of main SIR parameters, and a description of how the ring operates can be found in the introduction. Here we concentrate on a description of the project subsystems. Figure 4.1 shows a detailed schematic view of the ring with all the steering, correctors, and diagnostics. The elements are referred in the text under the names used in the figure.

4.1 Ion source and injection line

A multi-cusp, filament ion source that can be biased up to 30 kV is used for production of hydrogen or deuteron beams. A detailed description of the ion source and the extraction region will be given in J. A. Rodriguez' dissertation [26] (currently in progress). It is worth noting here that

- The beam extracted from the ion source has an emittance significantly smaller than the acceptance of the ring. For example, a beam with an energy of 20 keV has an emittance of 50 π·mm·mrad if the plasma electrode hole is Ø2 mm. This is approximately 25 times smaller than the vertical acceptance of the ring and
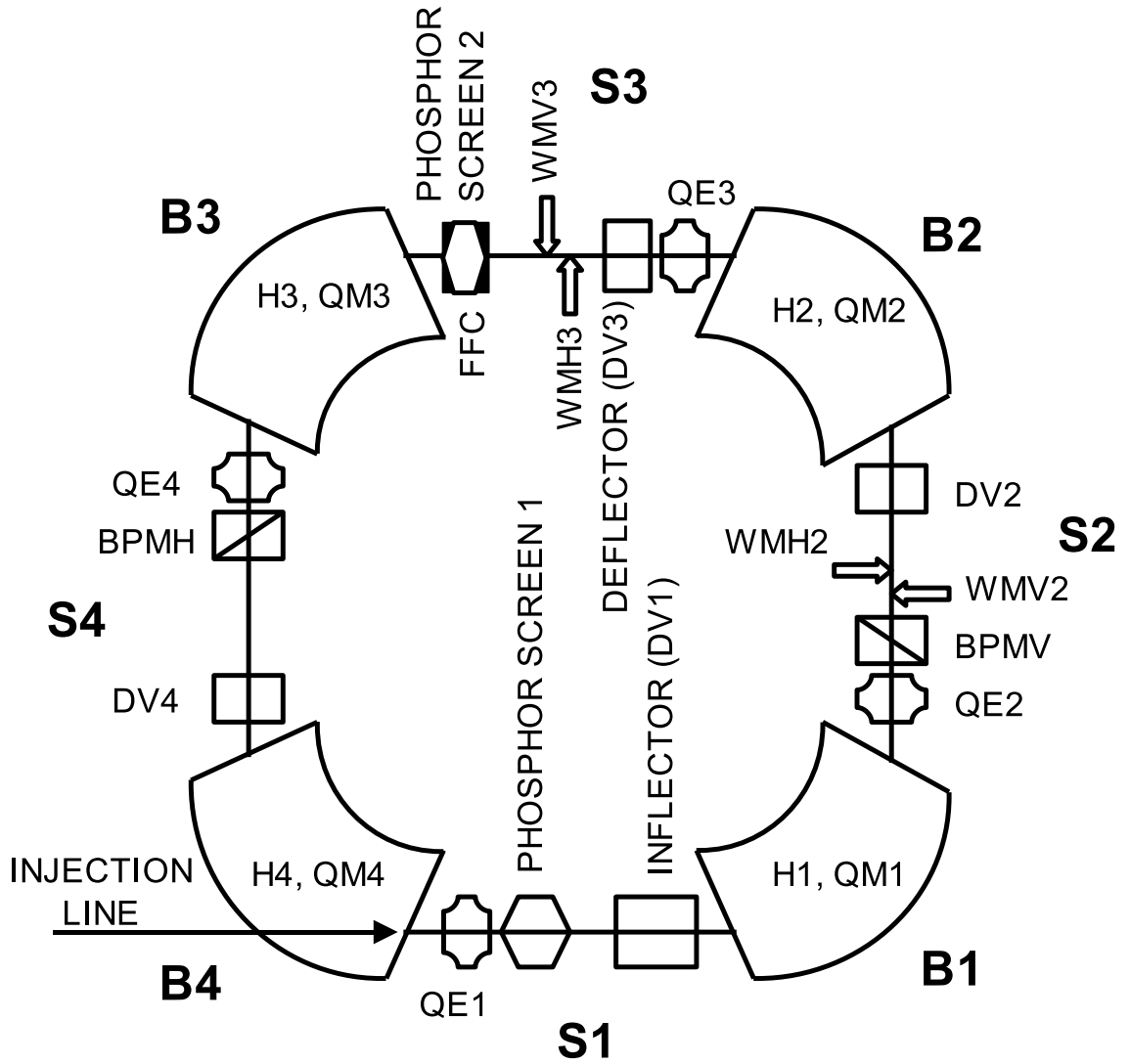
Figure 4.1: A detailed schematic view of the ring. All the elements are referred in this chapter under the same names as in the figure.

80 times smaller than the horizontal acceptance of the ring.

- The extracted beam current from the source easily exceeded the goal 100 μA. The maximum extracted current of the 20 keV H_2^+ beam was 400 μA.

The injection line consists of a dipole magnet that serves as a mass-state separator and is identical to the four ring dipoles, electrostatic beam steering electrodes, a triplet of electrostatic quadrupoles responsible for matching beam to the ring, beam chopper, and a 17.5° electrostatic bend. It also includes an emittance measurement system that follows the mass-separator magnet. A detailed description of the injection line is given in [26],[28].

4.2 Magnets

Four dipole magnets (B1-B4) form the Small Isochronous Ring. Each dipole consists of a steel yoke and upper and lower main coils. Each magnet also includes dipole and gradient correction coils.

4.2.1 Yoke

The magnet yoke consists of two mirror-symmetric halves, made of 1010 steel. The two halves are positioned relatively to each other with a help of dowel pins and held together by eight 5/16"-thick threaded rods, going through the return yoke. Figure 4.2 shows a cross-section of the magnet yoke. Table 4.1 gives important parameters of the yoke. A photograph of a half of the yoke set up on a support is shown in Figure 4.3.
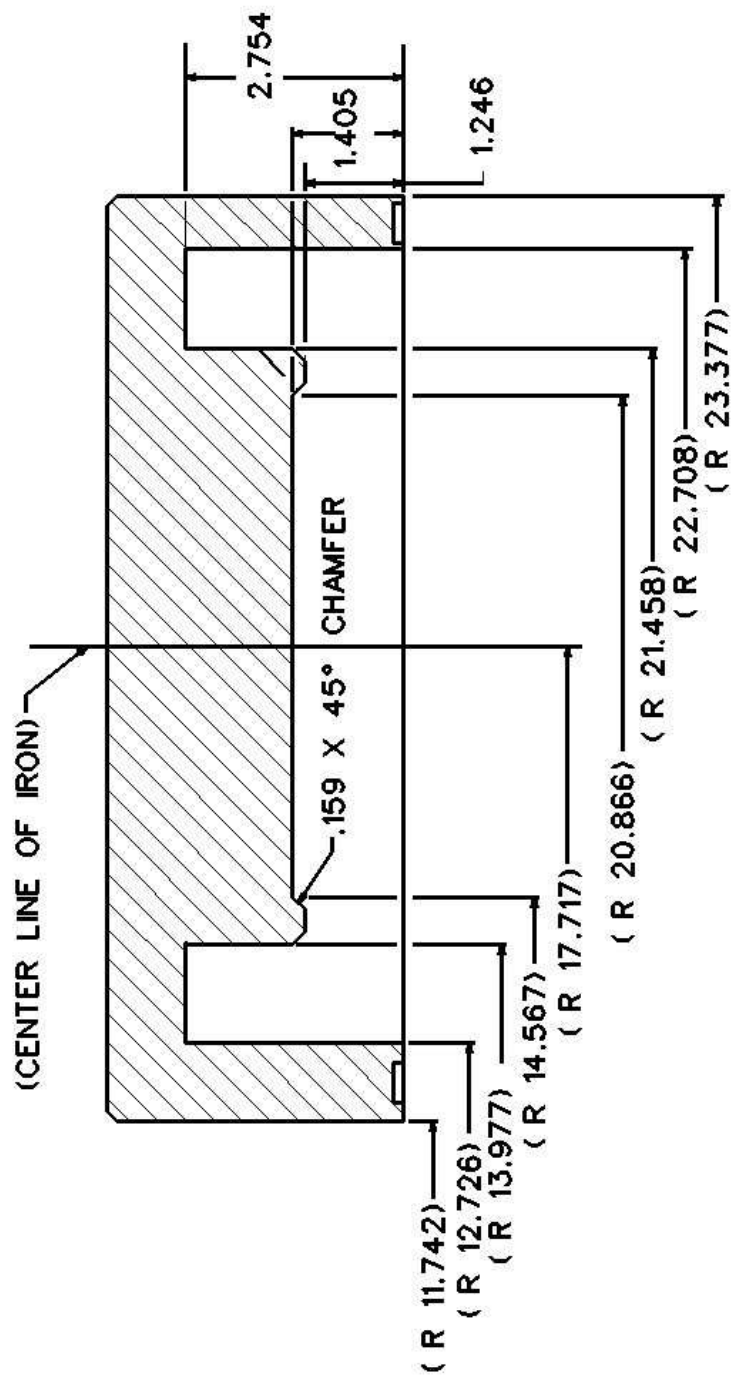
Figure 4.2: A cross-section of a half of the yoke. All dimensions are given in inches

Table 4.1: Important yoke parameters (all numbers given for a single half-yoke).

Mid-radius	450 mm (17.717")
Bending angle	90°
Half gap	35.7 mm (1.405")
Pole face angle	26°
Pole width	190 mm (7.481")
Full width	295.5 mm (11.635")
Full height	95 mm (3.738")
Total weight	91.7 kg (202 lb)

Figure 4.3: A lower half yoke on the support base.

4.2.2 Main coils

Each dipole magnet has two, upper and lower, main coils. Each coil consists of two pancakes. Twenty two pancakes total, including two spares were manufatured by New England Techni-Coil, Inc [1]. Figure 4.4 shows one of the pancakes sitting on the floor next to a 15" long ruler. Each pancake has 8 turns arranged in two layers with four turns in each layer. The coils were wound out of a hollow "quarter-of-an-inch" square conductor with Ø0.13" hole (0.25"x0.25"x0.13"ID). The fiberglass insulated conductor, used by the company, had dimensions (including insulation) 0.28"x0.28"x0.13"ID. The total length of the conductor for a pancake was approximately 600". Each pancake weighed approximately 11 pounds. The cross-section of the pancakes varied from 1.13"x0.58" to 1.26"x0.73" with an average size of 1.16"x0.61". The resistance of each pan-cake was approximately 0.01 Ω. The measured water flow through a pancake was 0.5 GPM for a pressure drop of 160 psi. The measured water flow was 2.5 times smaller than that calculated for a straight conductor of the same cross-section and length.

Eleven pancakes were wound clockwise. The rest were wound in the opposite direction. Each dipole coil was made of two pancakes tightened to each other with kapton tape. For additional insulation, the pancakes were separated by a layer of 10-mil-thick mylar. The pancakes in each coil were wound in opposite directions and paired as shown on Figure 4.5. This was done to reduce the effect of the transition between pancake layers which was in the mid-point of the pole face. A coil made

---

[1]New England Techni-Coil, Inc. 147 Middle Road, Tuftonboro, NH 03816
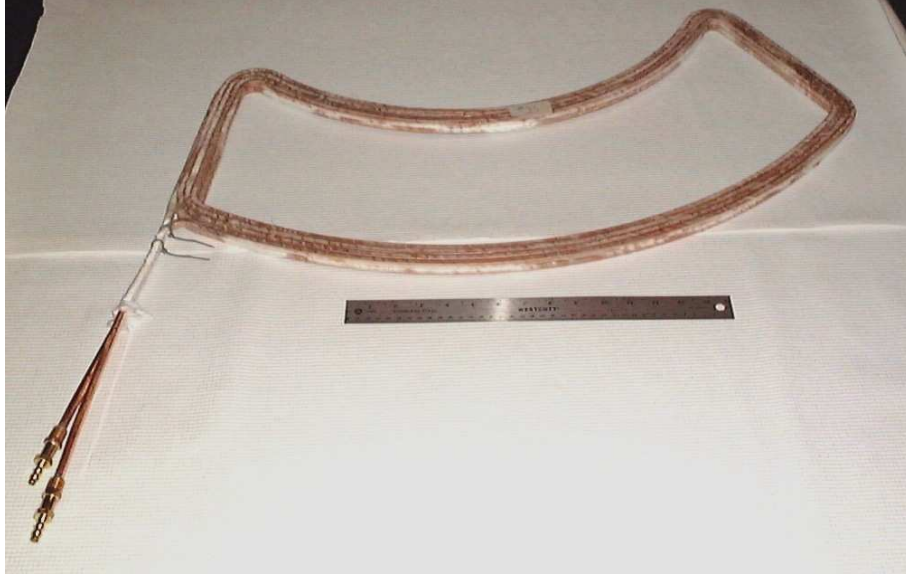
Figure 4.4: A double layer pancake next to a 15" ruler

of two pancakes wound in opposite directions produced less field distortion in the median plane than that made of two identical pancakes. When two pancakes of a different kind were paired as shown in Figure 4.5, the current dipole moment, defined as

$$\vec{d}_I = \frac{\sum \vec{r}_i}{N} \tag{4.1}$$

where N is the number of turns in two pancakes, 16, and $\vec{r}_i$ is a radius vector of the ith turn in a plane perpendicular to the pole face, was the same on both sides of the transition. If the coil were made of two identical pancakes, as shown in Figure 4.6 the dipole moment given by Equation 4.1 would change by $\Delta/8$ over the transition, where Δ is the distance between two conductors in a pancake.

The pancakes were connected between each other by copper bus-bars as schematically shown in Figure 4.7. Each bus-bar consisted of two pieces that were tightened
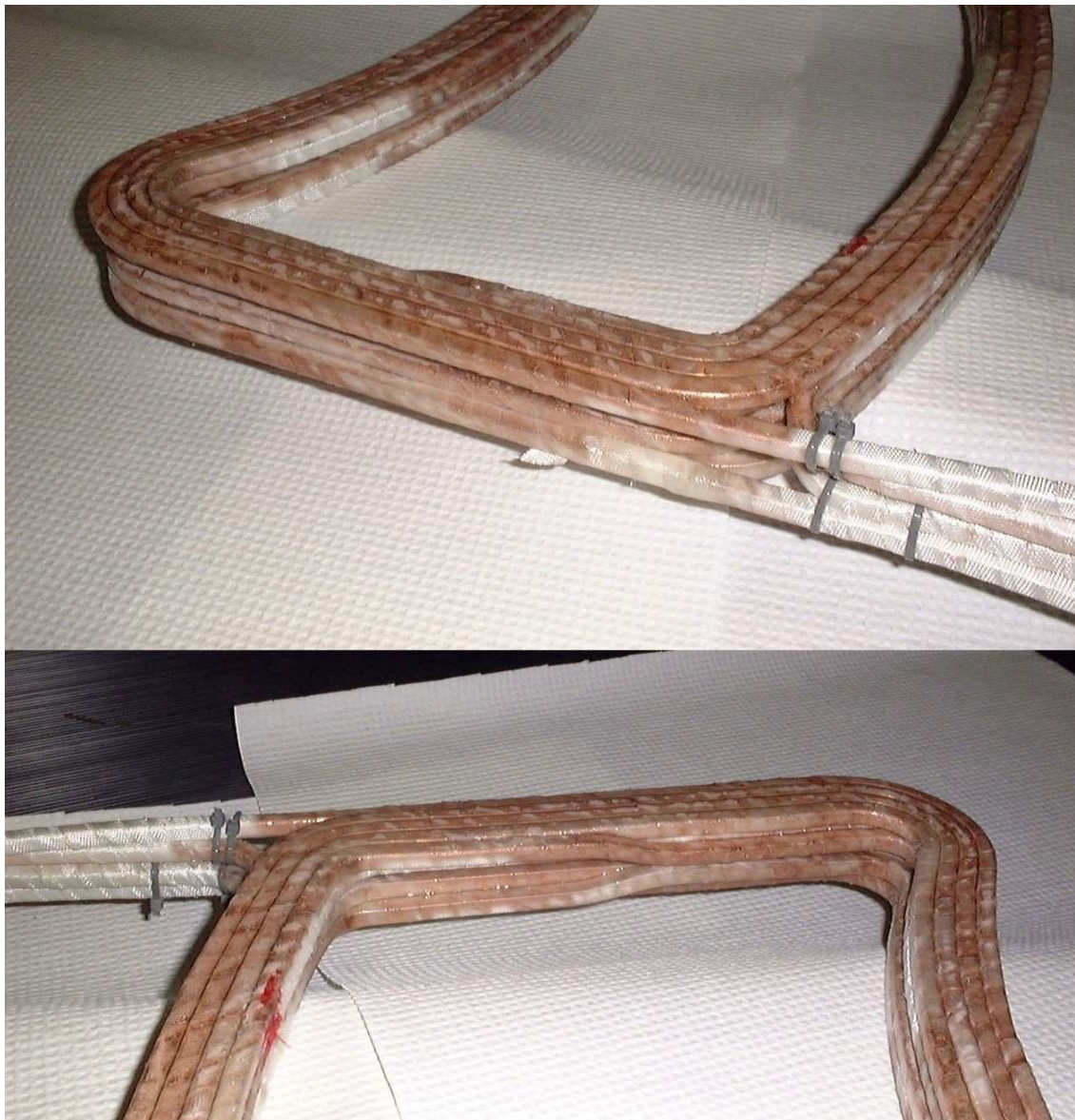
Figure 4.5: A coil made of two pancakes wound in opposite directions, as shown, produces the field less distorted than that from a coil made of two identical pancakes.
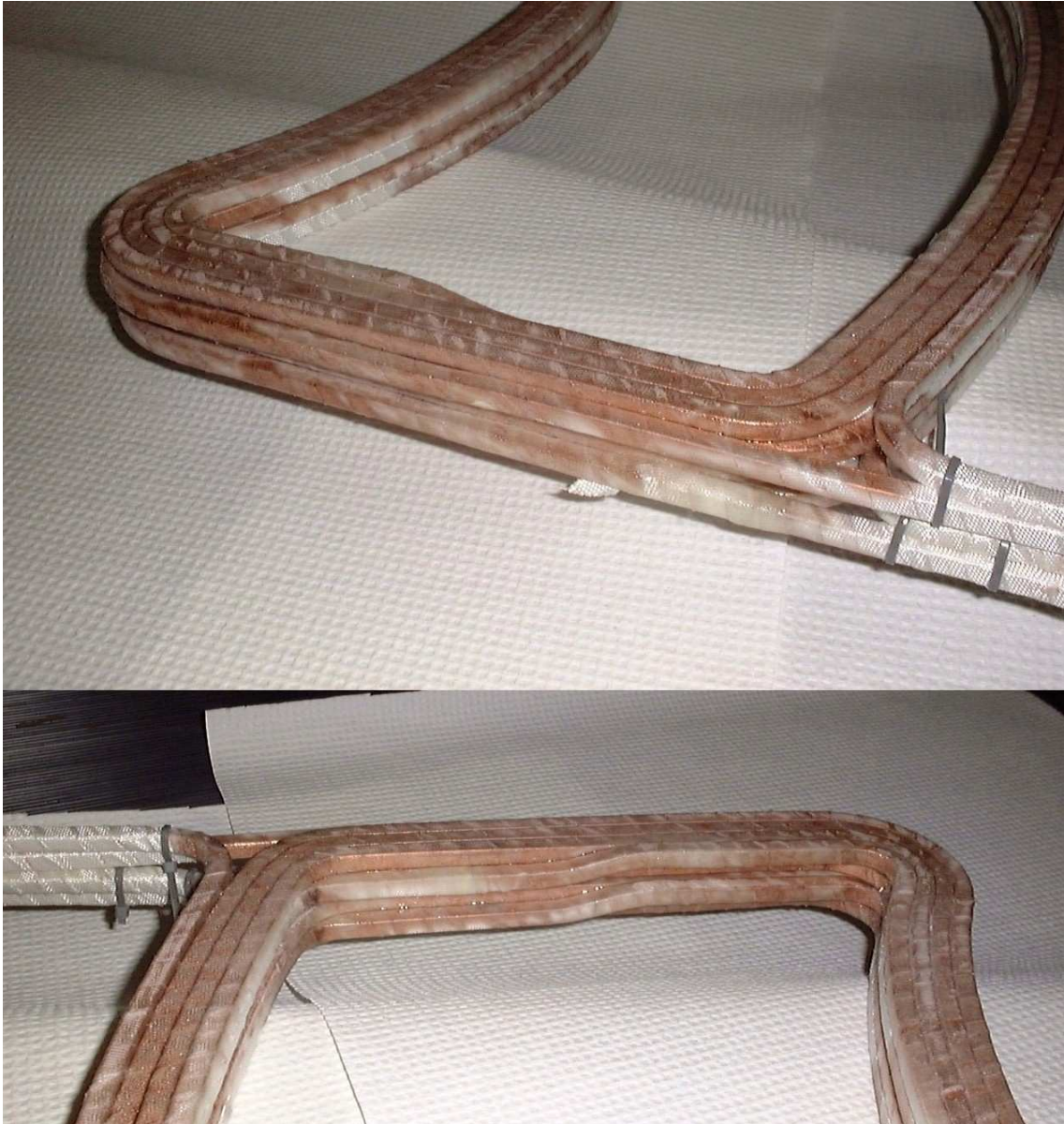
Figure 4.6: If a coil is made with two identical pancakes, its field will have a larger distortion than that of a coil made of two pancakes wound in opposite directions. The height of the center of the coil is different on left and right sides of the coil.

with screws as shown in Figure 4.8.

4.2.3   Assembly

Figure 4.9 shows a schematic cross-sectional view of an assembled dipole. From bottom to top, the layers are:

- 30-mil-thick, end-to-end piece of G-10

- 3-mil-thick, wrap-around piece of Mylar film. The same film provides additional insulation for the main coil on the sides

- Main coil with the dipole corrector coil (for a description of the dipole corrector see Section 4.4)

- 10-mil-thick, end-to-end piece of Mylar film

- A 2-3" long piece of G-10 (6 pieces in each half)

- Ø0.75" buna-N o-ring (6 rings of different thickness in each half)

- 30-mil-thick, end-to-end piece of G-10

- Quadrupole corrector plate (for a description see Section 4.4)

- Aluminum support pin

Each magnet was assembled according to the following procedure. First, the main coils with layers of insulation were inserted in the coil pits of each half of a dipole magnet. The coils were positioned and secured with small G-10 pieces inserted
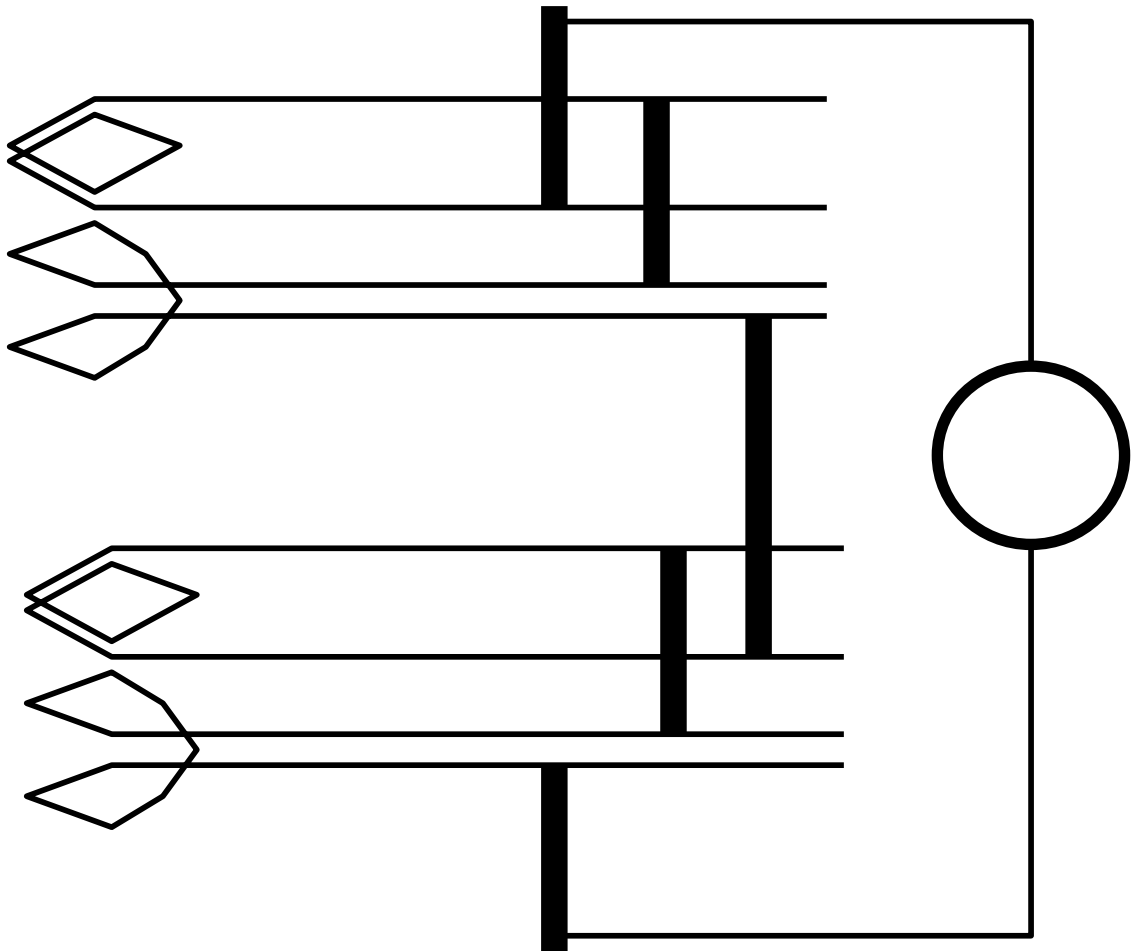
Figure 4.7: A schematics showing the connection of pancakes in a dipole
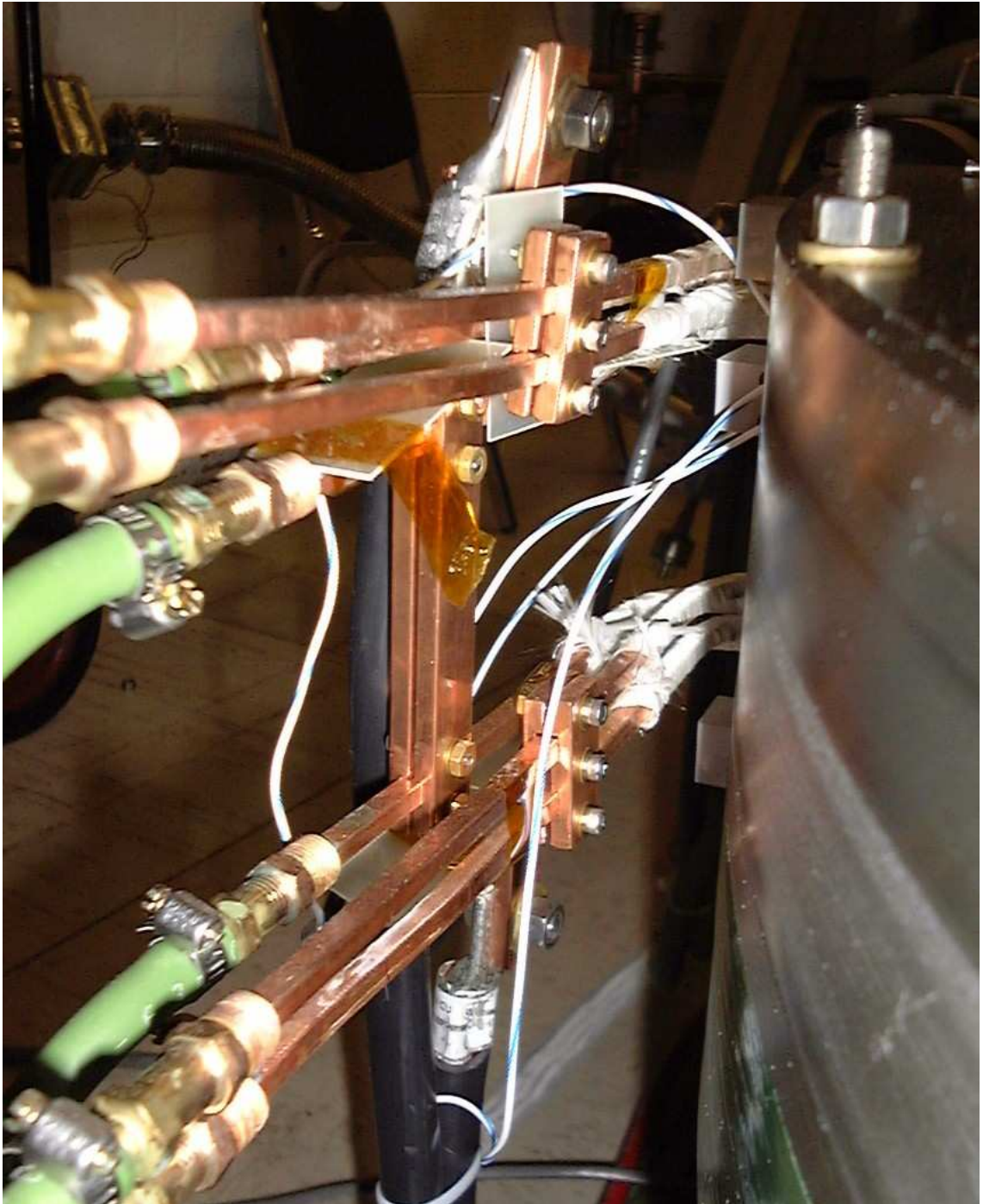
Figure 4.8: Pancake leads connected by bus-bars. Each bus-bar consists of two identical pieces tightened to each other with screws.
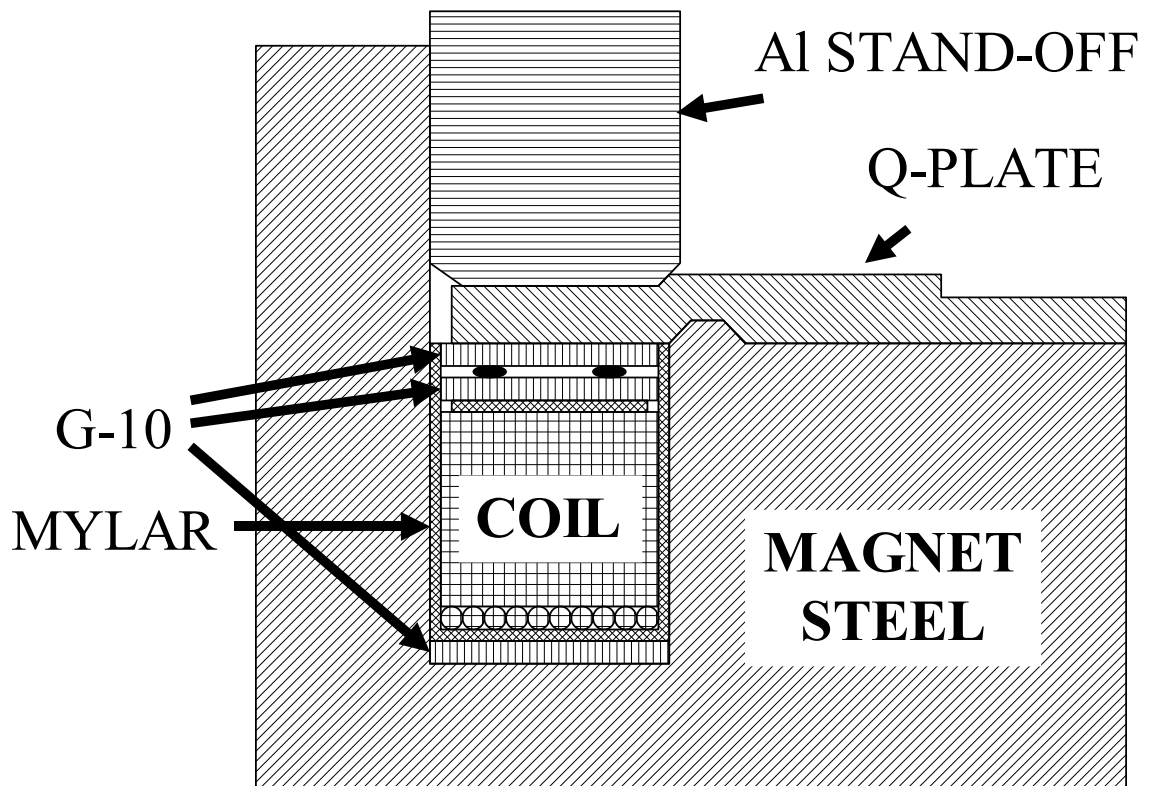
Figure 4.9: A cross-section of the SIR dipole magnet assembly. Only the lower left lower part of the assembly is shown.

between the coils and the magnet steel. Then, o-rings were selected to adjust the hight of the assembly so that quadrupole corrector plates would rest flat on upper pieces of G-10 with 10-30 mil gap between the plates and pole tips of the halves. After being positioned, the quadrupole corrector plates were fixed to the yoke halves with clamps. The force of the clamps compressed the o-rings and fixed coils in the grooves. Six aluminum support pins were placed on the upper G-10 pieces of the lower half. Next, the upper half was flipped over and placed on the lover half. The clamps were removed. The assembly was secured with eight pieces of threaded rod, going through the return yoke. The pins, through the the quadrupole plates and o-rings, provided pressure on the coil assemblies and kept the coils fixed in place.

4.3   Magnetic field measurements

Assuming that all magnets are identical, we have mapped only one magnet in details. The magnet, used as the injection line magnet, was mapped in two stages. First, we checked with an NMR probe that the field was flat inside the dipole. Second, we accurately mapped the fringe field.

The NMR probe was positioned vertically at the level of the median plane. However, there was no provision for accurate positioning the probe in the median plane. The measured field varied by less than 0.1% in a range of approximately $\delta r = \pm 50$ mm from the center of the pole tip ($r = 450$ mm) everywhere in the magnet. There was some field increase, approximately 0.05%, around $r \pm \delta r = 450 \pm 50$ mm, that was in a good agreement with simulations.

To measure the field in the edge region we used a transverse Hall probe manufactured by Bell Electronics. The system used for positioning of the probe consisted of two main parts: an aluminum plate with five longitudinal grooves and an aluminum sliding bar that held the Hall probe. The plate was attached to the quadrupole corrector plate that rested on a pole tip of the dipole. The sliding bar had 26 holes separated by a distance of 0.5" or 1.0". With a single pin, the probe could be accurately positioned at 130 (26x5) locations in the median plane. Figure 4.10 shows the Hall probe positioning system.

Figure 4.11 shows the magnetic field measured along the five grooves of the holder. The figure shows the magnetic field calculated by TOSCA as well. The magnetic field decreases slower than predicted by TOSCA. The measured effective length of the magnet was larger than the calculated one by 2.54 mm (0.1") or approximately 0.3%.

We used the measured field map to calculate the betatron tunes and isochronism in SIR. The difference between the measured and calculated fields was added to the calculated field map in the region where the field was measured. The rest of the calculated map left unchanged. Using the program GENSPEOG we have calculated the betatron tunes and the isochronism in the ring. Figure 4.12 shows the betatron tunes in the ring in the measurement-corrected and the original TOSCA fields. The betatron tunes in the measured field were slightly lower than in the calculated field. This was due to the "softer" edge of the measured field. Figure 4.13 shows the lag per turn in the measured and calculated fields. Though, the isochronous region

Figure 4.10: The Hall probe positioning system consists of an aluminum grooved plate, a pin, and a sliding bar that holds the Hall probe. The system is sitting on a table next to 6" ruler.
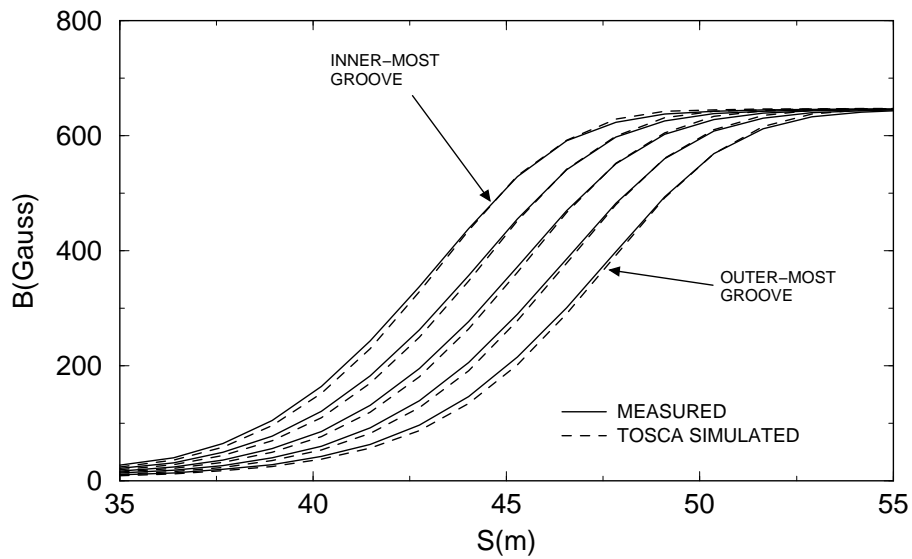
Figure 4.11: B_z measured in the edge region of the injection magnet. The median plane field was measured at 130 points along five lines by a single Hall probe. The figure also shows the field generated by TOSCA.

was smaller in the measured field, its width was large enough for the experimental program.

4.3.1 Hysteresis curve

The magnetic field in the magnets depends on the history of excitation and is a multi-valued function of the current. Setting up the field to a required level, especially with good accuracy, can be a time consuming problem if hysteresis is not taken into account. The solution to this problem is to use a magnetization (hysteresis) loop.

The maximum current in the ring dipoles is limited by the power supply and is equal to 130 A. This value was chosen as the maximum current in the hysteresis loop. The minimum was set to zero. The current in the coils of the injection line magnet was changed from 0 A to 130 A and then back to 0 A ten times. Then current was cycled two more times on the same loop. During last two times the field in the magnet was measured by an NMR probe. Figure 4.14 shows the upper part of the loop. Figure 4.15 shows the difference of the magnetic field curves from the linear function $B(I) = 725 \cdot I/130$. According to the figure the difference between magnetic field on the way down and on the way up reached approximately 4 Gauss (0.8%) at a current of 90 A. Figure 4.16 shows the difference between the magnetic field measured on the 11th cycle and the field measured on the 12th cycle. The difference between the cycles was $1.5 \cdot 10^{-4}$ and was caused by ripple of the power supply current. Appendix D contains the raw data for the magnetization loop.

If this loop is used, the current has to be changed always from 0 A to 130 A and back to 0 A. To change the current from 115 A to 100 A one has to, for example,

105
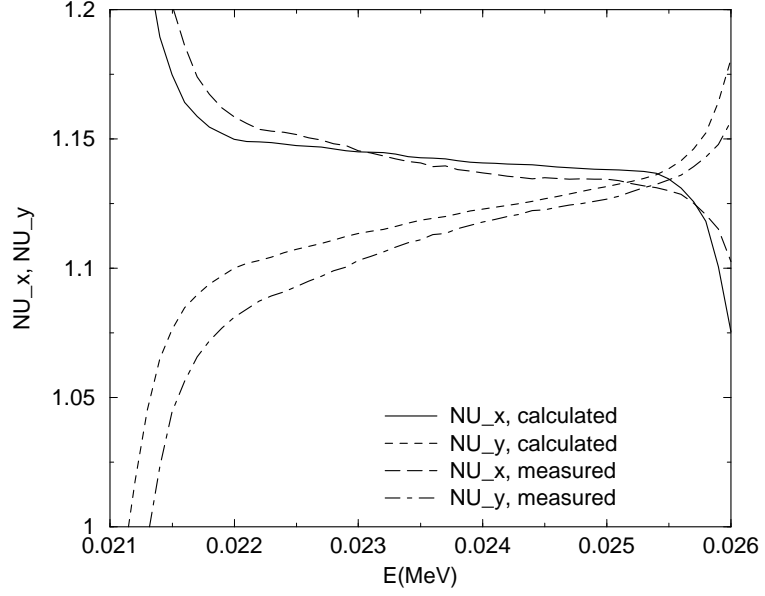
Figure 4.12: Bare betatron tunes in the measured field and in the field generated by TOSCA.
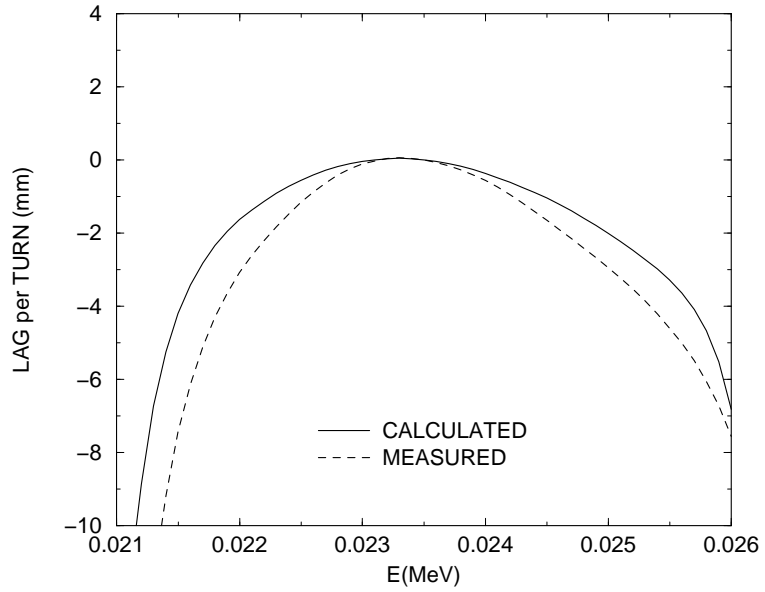
Figure 4.13: Particle lag per turn in the measured field and in the field generated by TOSCA.
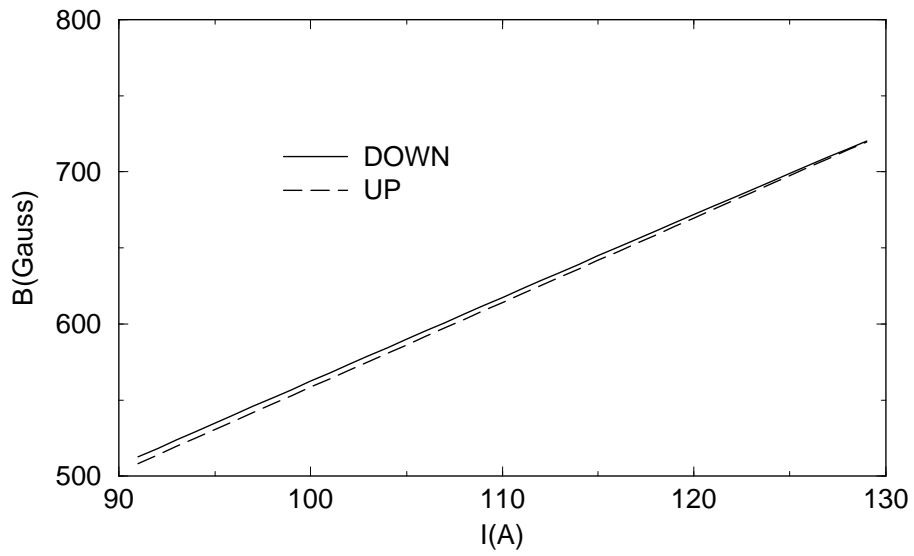
Figure 4.14: The upper part of the 0-130-0A hysteresis loop.
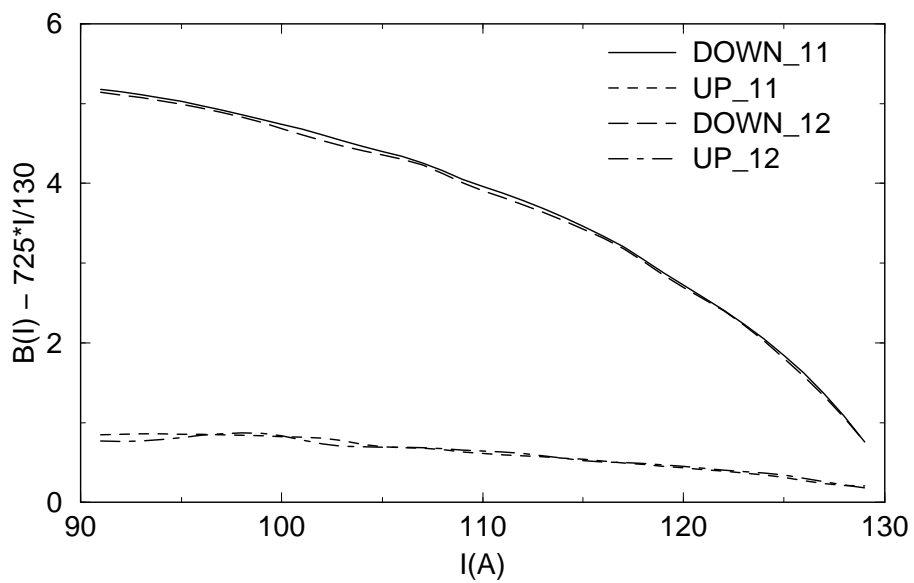
Figure 4.15: Difference of the measured magnetic field from the linear function $B(I) - 725 \cdot I/130$.
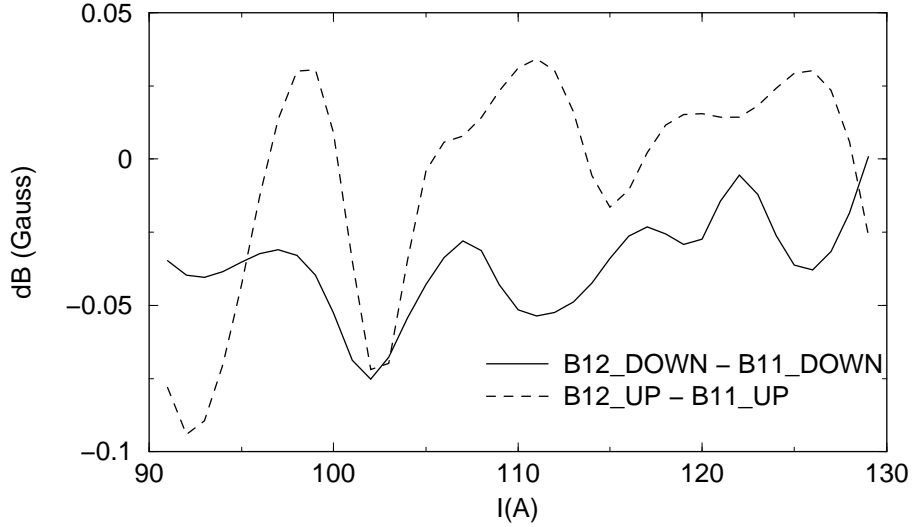
Figure 4.16: Difference between the 11th and 12th cycles.

increase current from 115 A to 130 A and then decrease it to 100 A. To increase current back to 115 A one has to go, first, to 0 A and then turn the current up to 115 A.

4.4   Steering and Quadrupole correctors

4.4.1   Horizontal beam steering (horizontal orbit correctors)

The dipole magnets B1-B4 include small steering coils H1-H4 that allow us to trim the field in each magnet independently. The corrector coils have 12 turns of 14 gauge wire. They were wound according to the following procedure:

- A 10-mil-thick mylar layer was directly attached to the main coils with patches of double-sided sticky tape.

- Patches of double-sided sticky tape were attached on the top of the mylar film

- Wire was directly wound on patches of double-sided sticky tape attached to the mylar layer

- The whole assembly was secured with kapton tape

Figure 4.17 schematically shows a cross-section of the horizontal dipole corrector wound on the main coil. Figure 4.18 shows a photograph of a half wound corrector coil seating on the main coil. Powered by small, independent power supplies with a maximum current of 3 A, the coils are capable of producing a magnetic field of ± 15 Gauss ($\pm 1.9\%$). This field variation is strong enough to correct 90 mm errors of the closed orbit at a main field level of 800 Gauss.

4.4.2   Vertical beam steering (vertical orbit correctors)

To control the vertical position of the beam in SIR we use electrostatic deflectors DV1-DV4. DV1 and DV3 are also used for injection and extraction. During injection and extraction these plates serve as inflector and deflector kickers (for more details on injection and extraction see section 4.5). After injection/extraction is completed, voltage on DV1/DV3 is switched to the steering mode.

Two more electrostatic deflectors, DV2 and DV4, are situated in straight sections S2 and S4. Figure 4.19 shows a photograph of one of the deflectors situated on a support frame. The deflector plates are 3" long and 4" wide. The wings on the plates increase the flat-field region from ± 30 mm to approximately ± 40 mm. Voltage on the these two deflectors is regulated by separate 4 kV power supplies, directly connected to deflector plates.
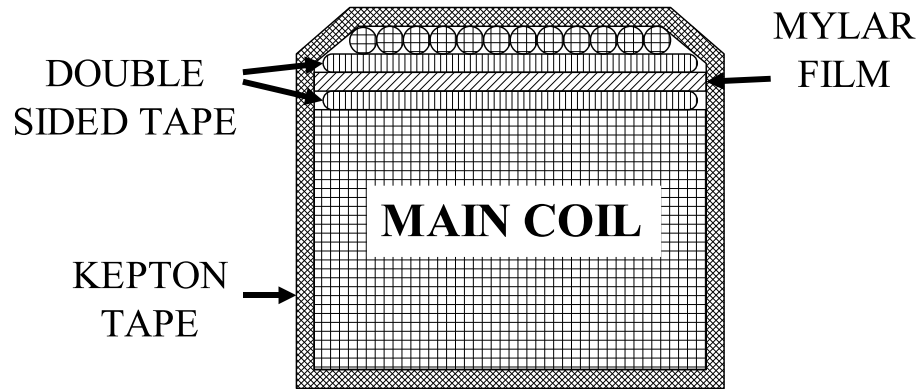
Figure 4.17: The dipole corrector is wound directly on the main coil. It is attached to the coil by patches of double sided sticky tape.
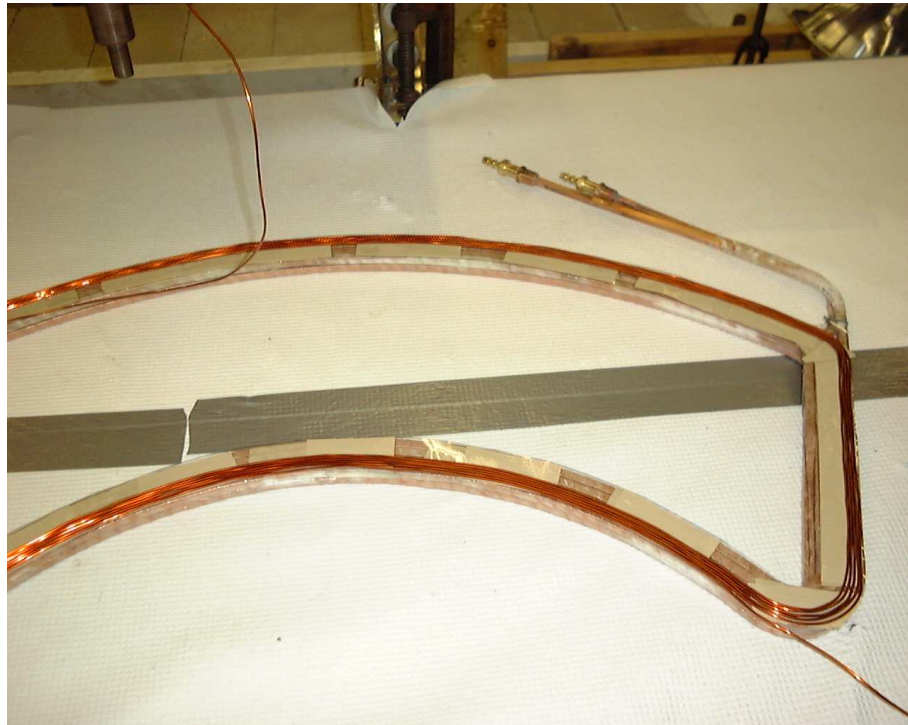
Figure 4.18: A half wound dipole corrector coil
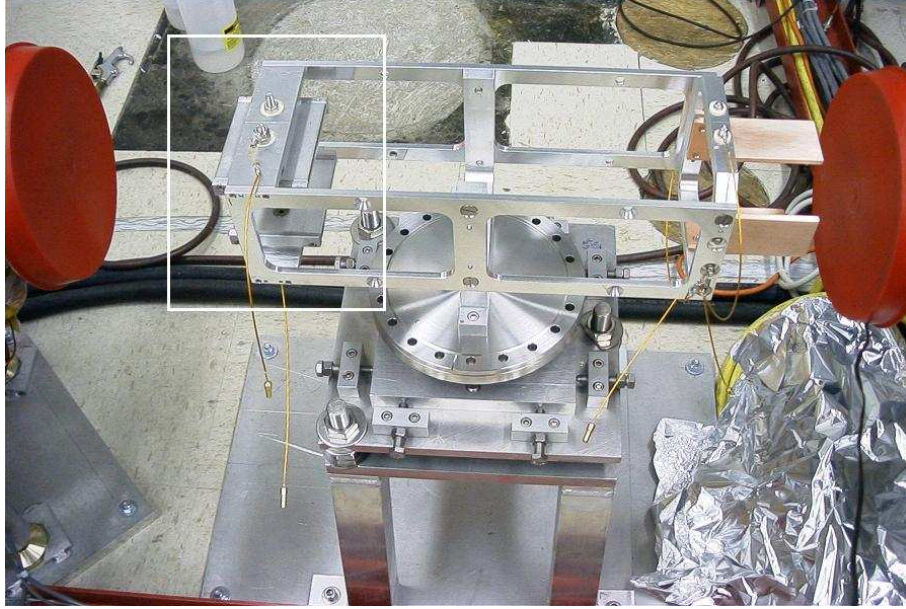
Figure 4.19: The free drift section S2 with the vertical deflector marked by the rectangle. The photograph also shows the electrostatic quadrupole and the support.

4.4.3 Quadrupole correctors

The betatron tunes and isochronism in SIR can be controlled, if required, by means of four electrostatic quadrupoles QE1-QE4 installed between the magnets and four gradient correctors QM1-QM4 situated in the dipole magnets.

Each electrostatic quadrupole consists of four flat, 44 mm-wide (1.73"), 89 mm-long (3.5") stainless steel plates separated by a distance of 100 mm (see Figure 4.20). Simulations done by Alberto Rodriguez with the help of the program SIMION [29] have shown that these quadrupoles provide a linear kick within a circle of a radius of 40 mm (1.7"). A deviation of the kick from an ideal linear dependence due to high-order multipoles does not exceed $\pm 5\%$ within the 40 mm circle.

Each gradient corrector consists of four coils. Two coils were wound clockwise and other two in the opposite direction. Each coil has eight turns of 12 gauge wire.
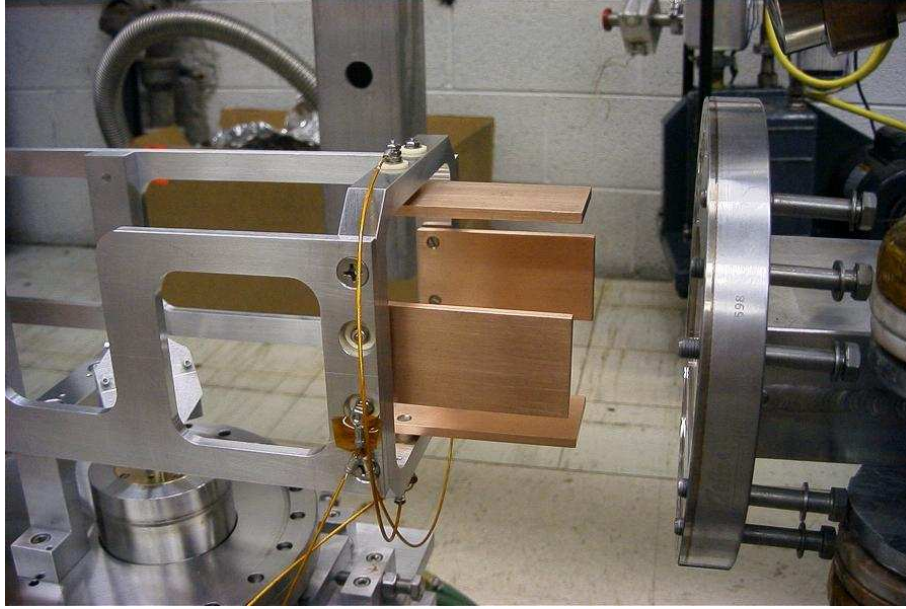
Figure 4.20: Photograph of one of the electrostatic quadrupoles.

The wire was placed in grooves cut in aluminum matrices (plates) and secured with epoxy. The plates were covered with a layer of 0.003"-thick mylar film for additional insulation. Placed on pole tips of the dipole magnets, these correctors induced field gradient. Figure 4.21 shows one the aluminum plates with two coils. The magnetic field of the gradient correctors was calculated with POISSON. Figure 4.22 shows the POISSON model. Figure 4.23 shows the median plane magnetic field with the quadrupole corrector on and off. A gradient of the field induced by the corrector is 4 Gauss/cm for a coil current of 12 A (see figure 4.24).

4.4.4 Legitimacy of using electrostatic correctors in SIR

Let's assume that we have two short deflectors of the same length L: one electrostatic with a field $\mathcal{E}$ and the other magnetic with a field B. Let's also assume that both deflectors deflect particles by the same angle α. The angle, in the first approximation,

112

Figure 4.21: The gradient corrector consists of two grooved aluminum plates with 12th gauge wire placed in the grooves. The photograph shows one of the plates.
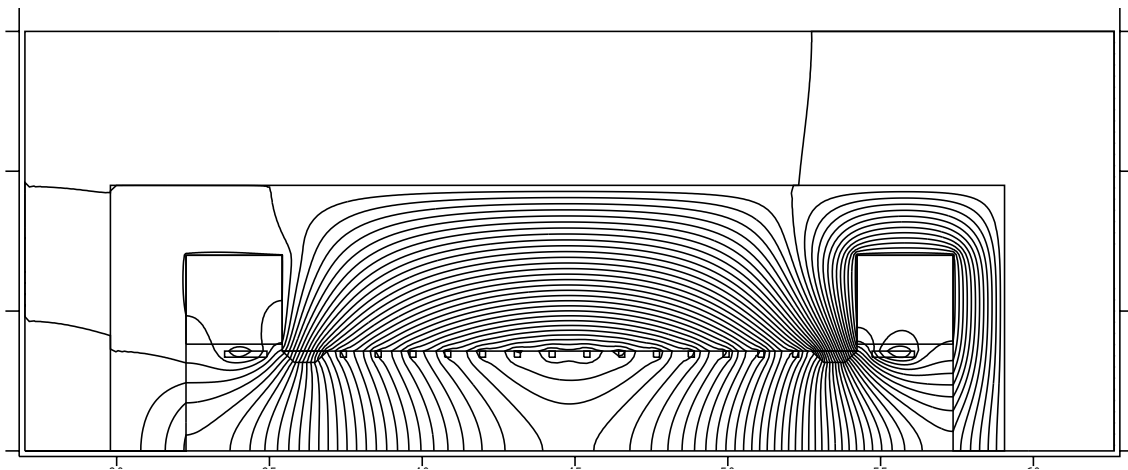
Figure 4.22: A POISSON model of the gradient corrector. The main coils are off.
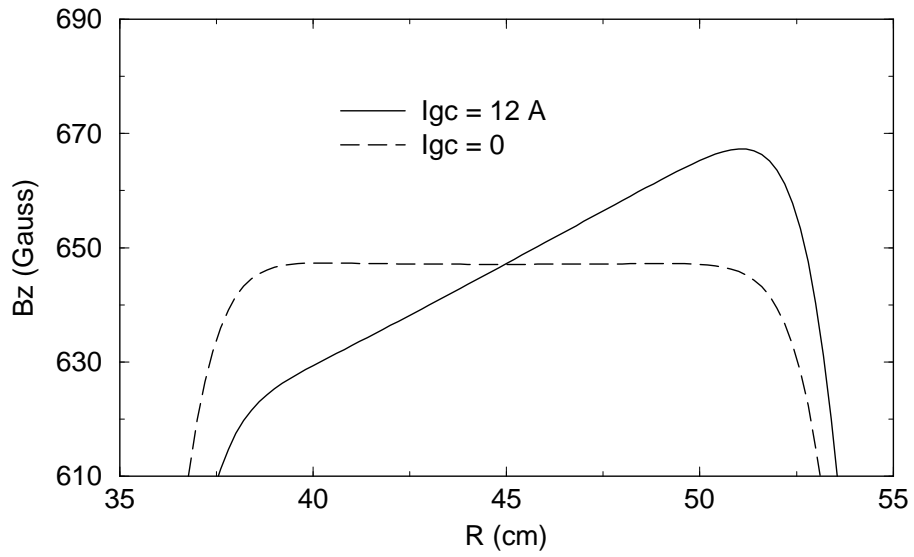
Figure 4.23: The magnetic field, generated by POISSON, with and without the field of the gradient corrector. Current in the gradient corrector was 12 A.
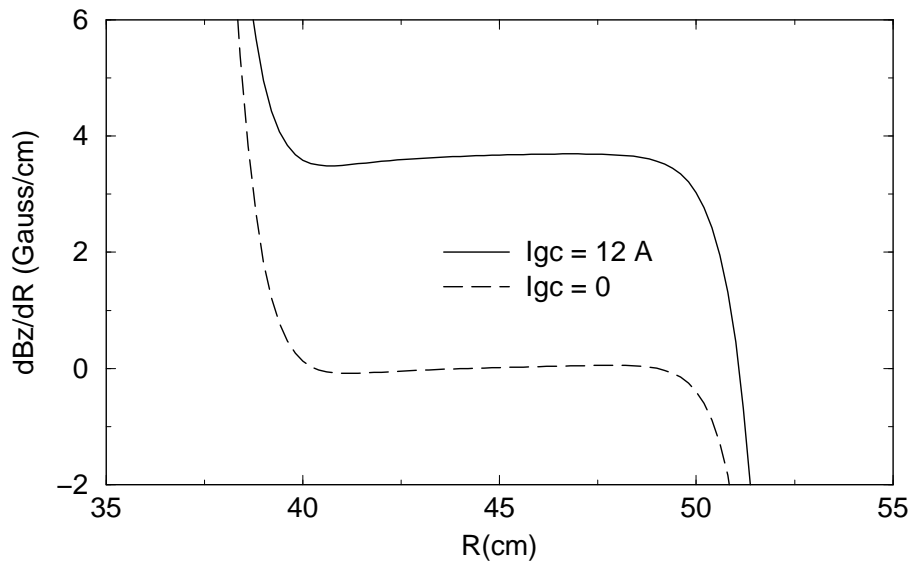
Figure 4.24: The field gradient with and without the field of the gradient corrector. Current in the gradient corrector was 12 A.

is (in CGS):

$$\alpha = \frac{qBL}{cmv} \quad \text{magnetic bend} \tag{4.2}$$

$$\alpha = \frac{q\mathcal{E}L}{mv^2} \quad \text{electrostatic bend} \tag{4.3}$$

The ratio of the equations 4.2 and 4.3 yields the formula:

$$\mathcal{E} = \beta B \tag{4.4}$$

where β is v/c. Then using electric field to steer and manipulate a low energy beam is more advantageous than using a magnetic field. The design of electrostatic devices for low beam energies is usually simpler than the design of magnetic correctors. On the other hand, electrostatic devices have to be in vacuum, requiring electrical feedthroughs and complicating the design of the vacuum chamber and alignment systems.

As was mentioned in section 3.1.1, the beam time-energy dynamics in electric field is different from that in magnetic field . Because SIR simulates a full-scale isochronous cyclotron or small synchrotron, where the magnetic field is used for beam bending and focusing, use of electrostatic devices in SIR must be limited to cases when the distortion of the time-energy dynamics produced by the electric field is small.

Electrostatic vertical deflectors

From the energy conservation law, the velocity of a particle in the electric field, in the low beam energy limit, is

$$\bar{v} = \sqrt{v^2 - \frac{2q\phi}{m}} \tag{4.5}$$

where v is the velocity in the field-free region. Thus, the difference between velocities of two particles with the same total energy after they enter the field can be found from the equation

$$\bar{v}_2^2 - \bar{v}_1^2 = (\bar{v}_1 + \bar{v}_2)(\bar{v}_2 - \bar{v}_1) = \frac{2q\,\delta\phi}{m} \tag{4.6}$$

If we assume that the field is weak and the difference between $\bar{v}_1$, $\bar{v}_2$, and v is small, the last equation yields

$$\frac{\delta v}{v} = \frac{q\,\delta\phi}{2E} \tag{4.7}$$

where E is the initial kinetic energy of the particles, $mv^2/2$.

Because the particles have different velocities, they spend different time in the field region. The time difference is

$$\delta t = -\frac{L}{v^2}\,\delta v \tag{4.8}$$

where L is the length of the field region. Thus the difference in the path of the two particles by the end of the field region is

$$\delta L = v\,\delta t = -L\frac{\delta v}{v} = -L\frac{q\,\delta\phi}{2E} \tag{4.9}$$

For dipole correctors, it is convenient to express the last formula through the deflection angle α and the distance between the particles δz

116

$$\delta L = -L \frac{q\, V\, \delta z}{2Ed} \tag{4.10}$$

where d is the distance between the deflector plates. Using 4.3, we can rewrite the last equation as

$$\delta L = -\alpha\, \delta z \tag{4.11}$$

The deflectors installed in the drifts S2 and S3 (each one of them) produce the vertical kick of $2.8 \cdot 10^{-2}$ if the voltage on the plates is 1000 V (the total voltage difference between the plates). If we assume a beam size of 10 mm, then the longitudinal separation between two particles with $z = .5$ mm and $z = -.5$ mm will grow by 0.28 mm per each passage of the deflector. Because of the betatron motion this effect does not accumulate. Two particles, one at the top of the bunch and the other at the bottom, will exchange position in 9 turns.

Electrostatic quadrupole correctors

Electrostatic quadrupole correctors located in all the drifts are designed for a maximum voltage of ± 1000 V on each electrode. SIR is designed to accept the beam with an energy spread of $\pm 10\%$. The beam size due to the 10% energy spread is approximately ± 25 mm. The distance between the pole tips of the quadrupole is 100 mm. Thus, the beam with the 10% energy spread occupies half of the free space between the electrodes. The potential difference between the quadrupole axis and the line $x = 25$ mm is 250 V if the quadrupole voltage is ± 1000 V. Using the formula 4.9, we conclude that separation between two particles with $x = 0$ and $x = 25$ mm

due to the quadrupoles in the ring increases with a rate of 2 mm per turn including the effect of all the four quadrupoles. The lag per turn due to the quadrupoles depends quadratically with the energy. For example, a particle with $\delta E/E = 2.5\%$ lags a particle with the equilibrium energy at a rate of 0.5 mm per turn, a negligible perturbation.

4.5   Chopper and Injection-Extraction system

Here we will briefly describe the system used for chopping, injection, and extraction of the beam. Detailed description of these systems, including results of beam simulations and measurements, can be found in [26].

4.5.1   Chopper

The chopper cuts a continuous beam into bunches. It is situated in the injection line after the quadrupole triplet as shown on Figure 1.1 and consists of two 5-cm-long plates. When voltage on the plates is zero, the beam goes straight through the chopper and is injected into the ring. When voltage on the plates is on, the electric field deflects the beam and prevents the beam from being injected into the ring. Voltage on the plates is regulated by two independent high voltage power supplies. A temporal structure of the HV signal is created by two fast semiconductor switches, PVX-4140, commercially available from Directed Energy Inc. The switches are specifically designed to drive high-impedance and capacitive loads. They can generate flat pulses with a rise/decay time of 25 ns and an amplitude of up to 3.5

kV. To truncate the fringe field of the buncher the plates are placed between two mesh plates. The mesh plates have a transparency of 90% and are separated from each other by a distance of 6 cm. The chopper deflects the beam from zero to the maximum angle in

$$\delta t = \tau_{rise} + \frac{L}{v} = 25ns + \frac{60mm}{1.5mm/ns} = 65ns$$

where L is a drift between the mesh plates and v is a particle velocity, here assumed to be 1.5 mm/ns, corresponding to 20 keV deuterons. Only a small part of this 65-ns-long tail can be captured in SIR. The rest of the tail, as well as the completely deflected beam, will hit the vacuum chamber of the injection line or will be lost in SIR. Simulations performed by Alberto Rodriguez and presented in detail in [26],[28] show that only particles that are in the first 10-15 nanoseconds of the 65-nsec-long tail will survive in the ring.

4.5.2 Inflector and deflector

To inject the beam into SIR we use a single-turn injection scheme. The inflector consisting of two copper plates is in the drift S1. It deflects the beam into the ring and sets the beam onto the closed orbit. Voltage on the plates is regulated by two PVX-4140s, identical to those used for chopping. Voltage on the injection plates is turned on well before a bunch enters the ring and turned off after the tail of the bunch is injected but before the head makes one complete turn. The empty gap in the beam is needed to safely turn off the inflector and turn on the deflector.

The deflector is another set of plates installed in drift S3. The deflector sends the

beam to the Fast Faraday cup, to measure the longitudinal beam profile.

4.5.3 Timing

Figure 4.25 shows the timing system used to switch the voltage of the buncher, inflector and deflector. A NIM signal generator produces a main strobe pulse that triggers all other devices, including an oscilloscope recording data. Driven by the strobe, two channels of a lab-made signal generator QDGG produce two TTL signals, to gate the two chopper switches. The length of the TTL signals can be changed from 50 ns to several micro-seconds. The delay time can be varied from 0 to several micro-seconds. A Nortec A-416 signal generator produces two TTL signals that fire the two inflector PVX-4140s. The length of the inflector TTL signals can be changed from 0.4 μsec to 4 μsec. The delay time can be changed from 100 nsec to 110 μsec. The system that drives the deflector is similar to that used for the inflector except that one more A-416 is used for a fine adjustment of the delay time. This is necessary because fine adjustment of the delay of an A-416 becomes very difficult if delay time is very long.

4.6 Diagnostics in SIR

Diagnostics in the injection line consist of the beam emittance measurement box and a Faraday cup installed at the end of the line. A detailed description of the injection line diagnostics can be found in [26],[28]. Beam diagnostics in SIR includes two phosphor screens, two horizontal and two vertical scanning wire monitors, one vertical and one horizontal shoe-box capacitive BPMs. Figure 4.1 shows location of
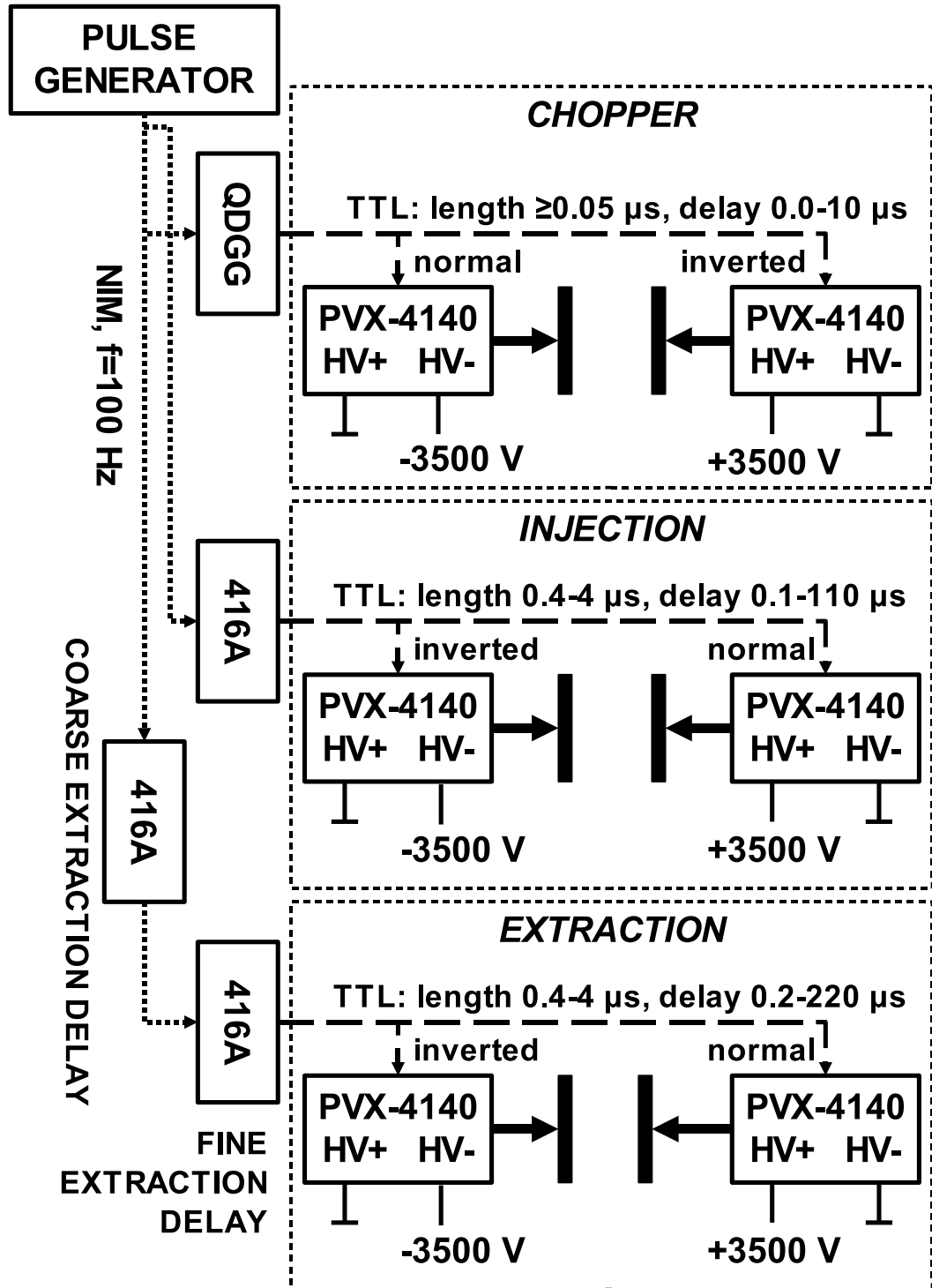
Figure 4.25: Timing system responsible for turning on and off voltage on the chopper, inflector, and deflector plates.

the diagnostics in the ring.

4.6.1 Phosphor screen monitors

A retractable phosphor screen is situated in the injection section of the ring (S1). The setup consists of an aluminum screen, covered with phosphor and a linear-motion feedthrough with two pneumatic cylinders. The screen can be moved in one of the three positions: in the way of the beam coming from the injection line, in the median plane to detect the beam after a single turn, and below the median plane completely out of the way. The beam spot on the screen is observed by a video camera through a 6" viewport and displayed on a monitor. Figure 4.26 shows a photograph of the injection section with the phosphor screen setup.

The other phosphor screen is in the extraction drift S3. The phosphor screen is situated above the median plane as shown in Figure 4.27. It is displaced from the median plane by the same distance as the fast Faraday cup. The phosphor screen in S3 can be also used as a Faraday cup.

4.6.2 Scanning wire monitors

Four scanning wire monitors are used in SIR. A pair of monitors, one vertical (WMV2) and one radial (WMH2), is in the drift S2. The other pair (WMV3 and WMH3), identical to the first one, is situated in the extraction drift S3 close to the fast Faraday cup. A radial scanning wire monitor consists of a 0.04"-thick, 2"-long piece of tungsten wire, an aluminum wire holder, and a 4"-stroke motorized feedthrough manufactured by Huntigton. Figures 4.28 and 4.29 show a photograph of one of the horizontal wire
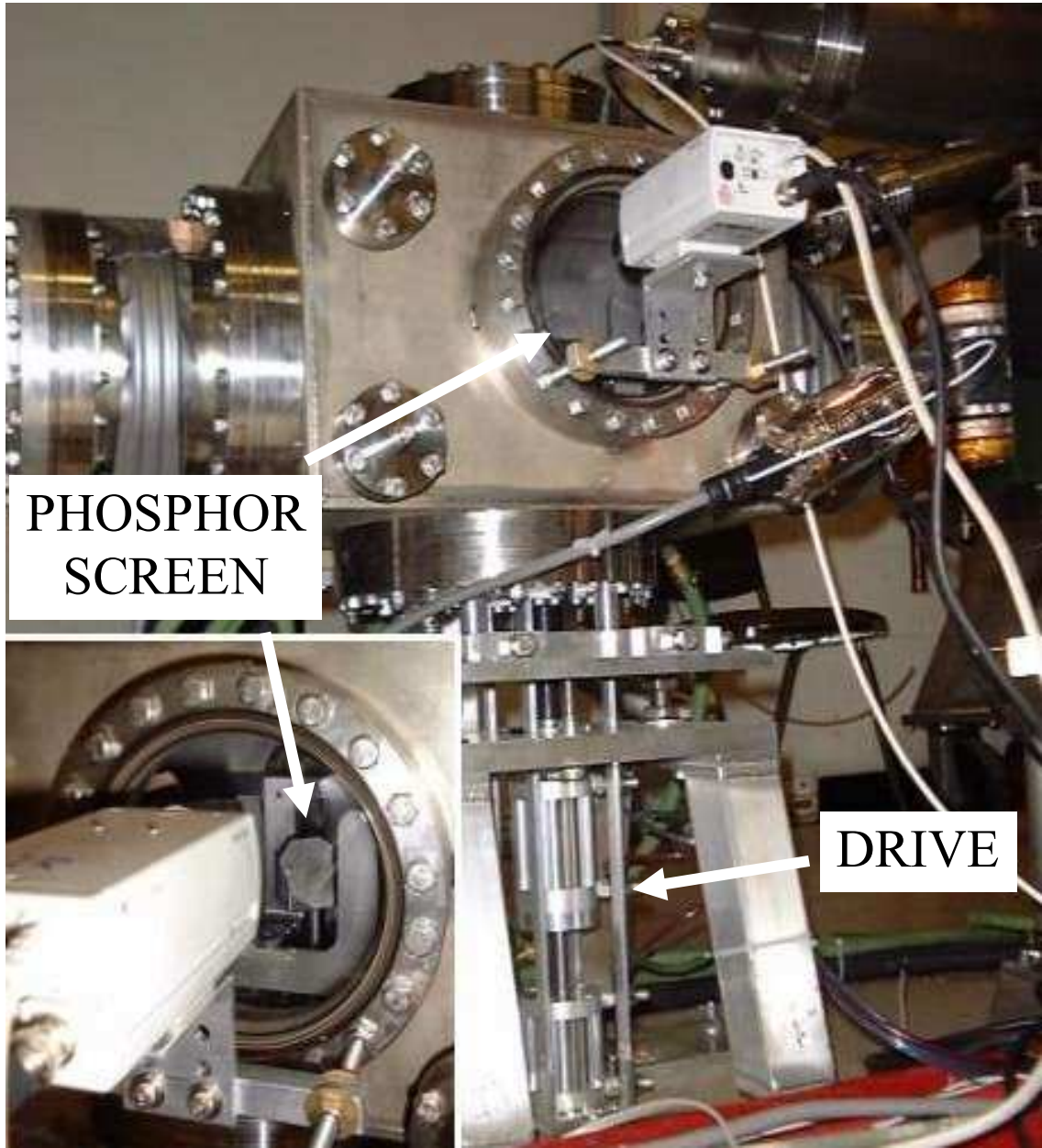
Figure 4.26: The injection section of the ring (S1). The main photograph shows the vacuum chamber with the viewport and the phosphor screen drive. The insert shows the viewport with the phosphor screen itself.
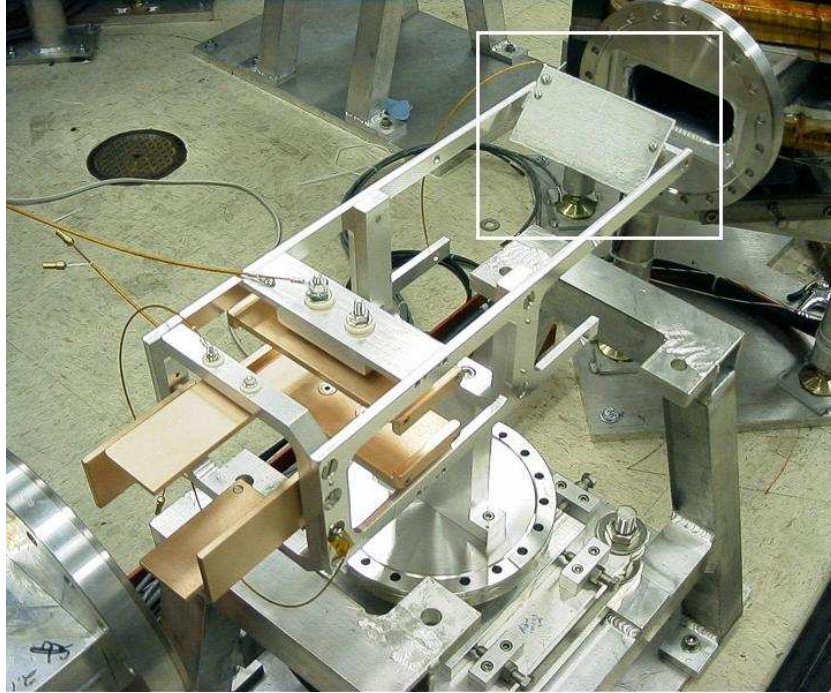
Figure 4.27: Extraction Section S3. The phosphor screen is shown in the white rectangle. In the complete assembly, the viewport is situated just above the phosphor screen.

monitors. The tungsten wire is attached to the aluminum holder by two setscrews and makes an electrical contact with the holder. The holder is attached to the linear motion feedthrough by two ceramic stand-offs and electrically isolated from the feedthrough. Electric current from the tungsten wire is transfered through a vacuum-rated flexible cable attached to the aluminum holder and a electrical feedthrough in the vacuum chamber. The vertical scanning wire monitors are similar to horizontal monitors but wider because the horizontal beam size is larger than the vertical size.

4.6.3 Fast Faraday Cup

A coaxial fast Faraday cup, located in the drift S3 just after scanning wire monitors WMV3 and WMH3, is used to record the longitudinal charge distribution of the
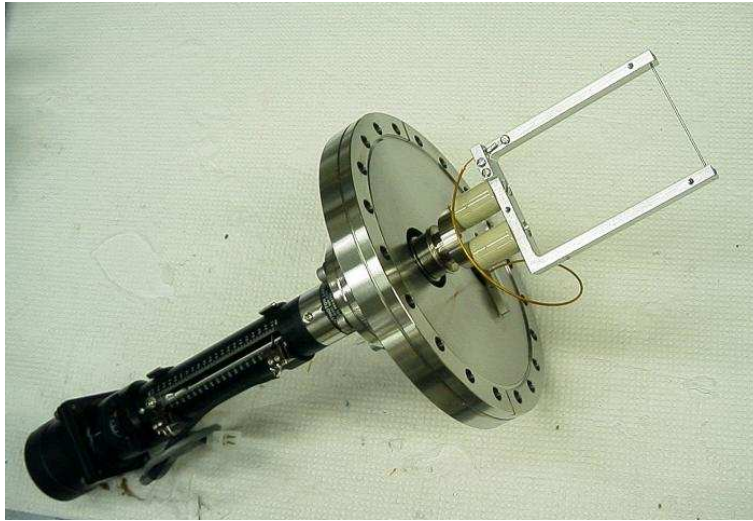
Figure 4.28: One of the two horizontal scanning wire monitors.

Figure 4.29: One of the two vertical scanning wire monitors. The wire holder in the monitor is wider than that in the horizontal wire monitors.

beam. The Faraday cup is offset vertically by 2.5" from the median plane. This clearance lets the beam circulate in SIR without hitting the Faraday cup. When a longitudinal beam profile is to be measured, the beam is deflected onto the Faraday cup by the pulsed deflector kicker. The cup has an active area of Ø12.7 mm (0.5"). The whole device can be moved radially by a linear motion feedthrough identical to the feedthroughs used for scanning wire monitors. By changing the horizontal position of the Faraday cup, we can map the beam charge density as a function of length (time) and horizontal displacement. More details on a design of the Faraday cup can be found in [26].

4.7 Vacuum system

The emittance box and the vacuum chamber in straight sections S1-S4 were made of 304 stainless steel plates. Holes for flanges and nipples were waterjeted in the plates, and flanges and nipples were directly welded to the plates. Regular 6" stainless steel tube was used for the section of the injection line that connects the emittance box and the ring and contains the quadrupole triplet and the chopper. Though stainless steel is almost non-magnetic in bulk, its permeability increases if it is machined or welded. Variation of the μ is unpredictable and very difficult to quantify. Available experimental data on variation of the μ due to welding and machining is limited and (somewhat) inconsistent. To avoid complications related to increased permeability of stainless steel, the vacuum chambers in all the dipoles were made of aluminum.

Aluminum and stainless steel parts were joined by bi-metal flanges [2]. Figure 4.30 shows a piece of the vacuum chamber of one of the dipoles with two 8" bi-metal flanges.

Figure 4.30: A 90° piece of the rectangular aluminum vacuum chamber in the dipole magnets. Two 8" bi-metal flanges are used to connect the piece to stainless flanges of the straight sections.

4.7.1   An estimate of the residual gas pressure in SIR

The two main sources of residual gas in the ring are outgassing from the walls of the vacuum chamber and the gas flux from the ion source. We use four 500 L/s turbo-pumps in the final setup. Two pumps are in the injection line and two pumps are in

---

[2]Manufactured by Atlas Technologies, 301 10th Street, Port Townsend, Wa, 98368, USA

the ring. One of the pumps in the injection line is located just below the ion source. The other one is in the beam emittance measurement box. The pumps in the ring are located in the drifts S1 and S3.

To estimate the gas flux from the ion source to the ring we have used the model shown in Figure 4.31. In this model, all gas is assumed to come from the ion source. Outgassing was included later (see next paragraph). Pressure in the source was 1 mTorr. To calculate conductance of the pipe segments we have used the Clausing formula

$$C_{pipe} = R\left(\frac{L}{D}\right) \cdot \frac{v\,A}{4} \tag{4.12}$$

where L and D are the tube length and diameter respectively, A is the area of the pipe, v is velocity of gas molecules, and $R(L/D)$ is a dimensionless coefficient that depends on the ratio of the pipe length and diameter. The coefficient, tabulated as a function of L/D, can be found, for example, in [30]. Though the formula accurately describes conductance of circular tubing, we used it to calculate the conductance of the vacuum chamber in the dipoles which has a rectangular cross-section. The rectangular pipe was substituted with a circular one of the same area. Appendix E provides mathematical details related to the calculation of the gas flow from the ion source. Table 4.2 summarizes the results of the calculations. It gives the average pressure in the ring for two sizes of the hole in the ion source plasma electrode: Ø2 mm and Ø1 mm (the second number is included in brackets). Pressure was calculated for hydrogen and deuterium. The first column gives numbers for the case when only

three turbo-pumps are used, assuming that the pump in the emittance box is shut off.

The other source of the residual gas in the ring is outgassing. According to [31] the outgassing rate of unbaked stainless steel after a day of pumping is on the order of 10^{-8} Torr l/(cm^{2}sec). In these calculations we assumed an outgassing rate of 10^{-9} Torr l/(cm^{2}sec). This means longer pumping, maybe a week or so. According to some references, for example [30], freshly machined aluminum can outgas less than stainless steel. The actual outgassing rate of an aluminum surface depends on such parameters as surface roughness and the oxide layer thickness. Here we assumed for simplicity the same number for both stainless steel and aluminum. In estimating pressure in the ring due to outgassing, we assumed that the ring and the injection line were completely separated, and there was no gas flux between these two. Mathematical details of the calculations are presented in Appendix E. The estimated average pressure of water vapor in SIR was $5.5 \cdot 10^{-8}$ Torr. Baking the vacuum chamber can decrease pressure and pumping time. Though, many parts of the vacuum chamber cannot be baked because they contain or come in contact with heat-sensitive parts such as o-rings (emittance box), insulated wire (injection line and straight sections of the ring), and magnet coils (dipole magnets).

In the last two paragraphs, we presented a rough estimate of gas pressure in the ring. The results of measurements of the residual gas pressure are presented in chapter 5.

ION SOURCE

0

570 mm
∅152 mm
1

1060 mm
∅152 mm

1007 mm
∅83 mm

2A

NOT
INCLUDED

407 mm
∅47 mm

2

SIR

3

1007 mm
∅83 mm

NOT
INCLUDED

P_0=1 mTorr
S_1=S_{2A}=S_2=S_3=500 L/s
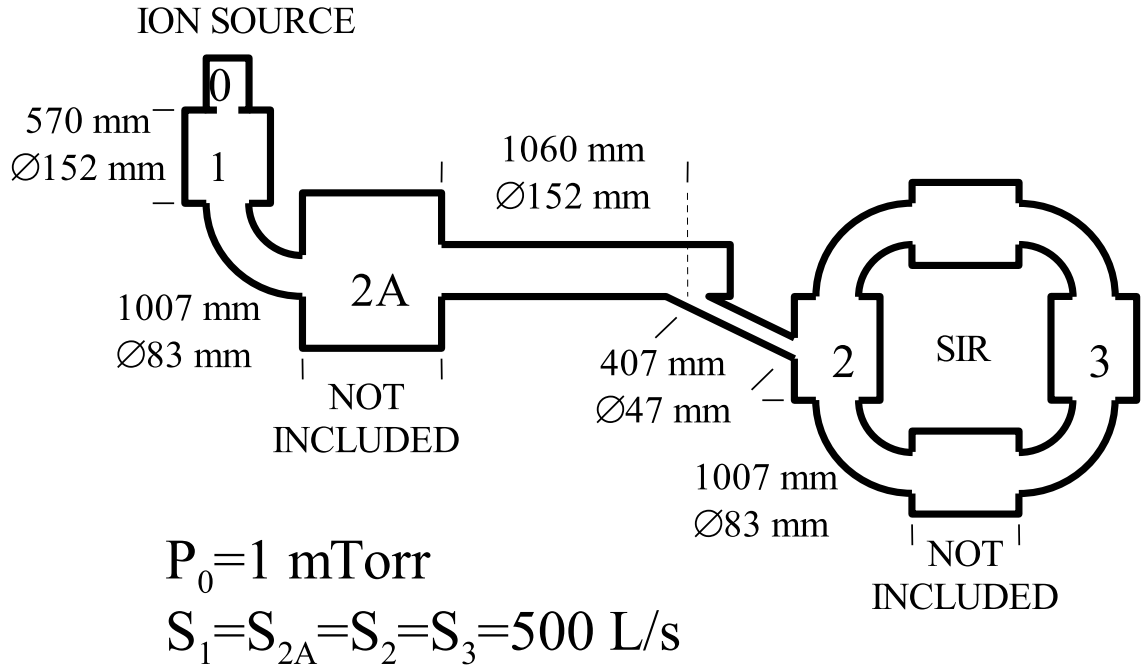
Figure 4.31: Schematic used for calculation of the gas flow from the ion source. Four turbo-pumps were installed at points 1,2A,2, and 3. A simplified, lumped-element model used for analytical calculations and equivalent to the schematics is shown in Figure E.1.

Table 4.2: Average pressure in SIR due to gas flux from the ion source. It is assumed that pressure in the source is 1 mTorr. The pressure was calculated for two sizes of the hole in the plasma electrode: ∅2 mm and ∅1 mm (the second number is included in brackets).

	3 Turbos	4 Turbos
H_2	1.4e-7 (3.5e-8)	4.3e-8 (1.1e-8)
D_2	7.3e-8 (1.8e-8)	1.8e-8 (4.6e-9)

4.7.2 Expected beam life time in SIR

At a pressure of 10^{-8}-10^{-7} Torr the beam life-time is primarily determined by electron capture from atoms and molecules of residual gas. According to [32], the cross-section for electron capture of a 10 keV proton is almost the same for hydrogen, nitrogen, water, and argon and equal to $1.5 \cdot 10^{-15}$ cm^2. The cross-section weakly depends on beam energy for an energy range of several tens of keV. Because the cross-section is almost the same for all these gases, in calculating beam losses, we added up the partial pressure of all gases and used average value of the cross-section. In the approximation that all losses are determined by electron capture, beam intensity in SIR can be expressed as a function of the turn number, N, by the formula:

$$I(N) = I(0)e^{-\frac{N\,C}{L}} \tag{4.13}$$

$$L = \frac{1}{\sigma n}$$

where C is a circumference of the ring, L is the mean free path, σ is the cross-section of electron capture, and n is the number of molecules of residual gas per unit volume. Figure 4.32 shows beam intensity vs. turn number in SIR calculated from Equation 4.13 for three values of the residual gas pressure: $5 \cdot 10^{-8}$ Torr, 10^{-7} Torr, and $5 \cdot 10^{-7}$ Torr. The mean free path for these pressure values is 631 turns, 316 turns, and 63 turns respectively.

Beam particles can ionize molecules and atoms of residual gas. Positively charged ionized atoms and molecules are expelled from the beam. Electrons, on the contrary, are attracted to the beam. According to [19], the cross-section for ionization at low
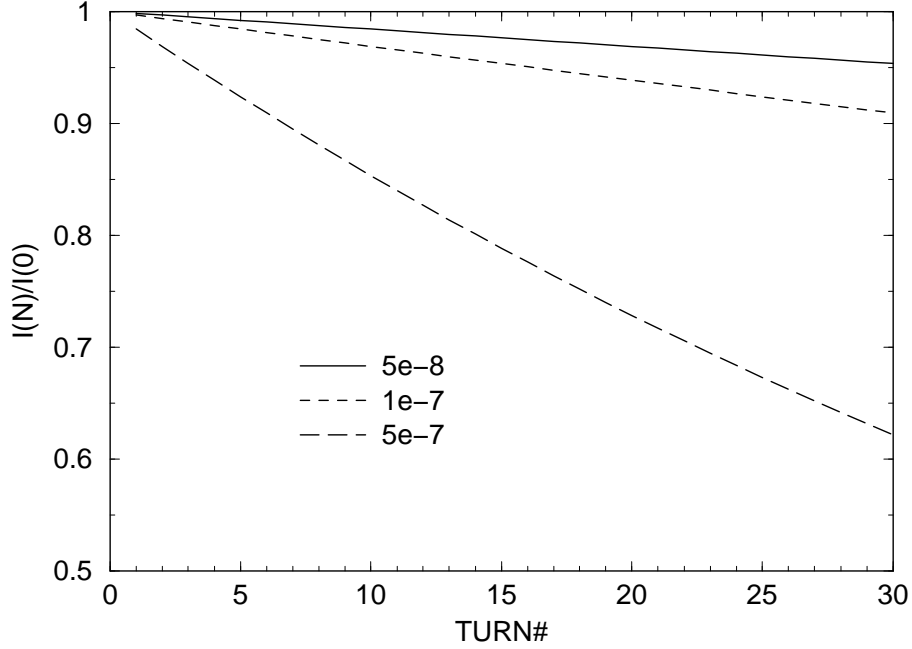
Figure 4.32: Estimated decrease of the beam intensity in SIR due to electron capture from the residual gas.

energies is close to 10^{-16} cm^2. Assuming the extreme condition that all positively charged ionized ions are momentarily expelled from the beam, the maximum degree of neutralization at a distance l from the head of the bunch can be estimated as

$$\xi = \frac{l}{L} \qquad (4.14)$$

where L is a free mean path between ionization events. Table 4.3 gives the maximum degree of neutralization for a 3-meter long bunch and a residual pressure of $5 \cdot 10^{-8}$, 10^{-7}, and $5 \cdot 10^{-7}$ Torr.

The empty gap in the beam prevents electrons from accumulating in the beam. An electron with an energy of 1 eV has a velocity of $6 \cdot 10^5$ m/sec. In free space, the electron would travel a distance of 0.6 m in one microsecond. Thus, the electron will

132

Table 4.3: The maximum degree of neutralization at the end of 3-meter long bunch.

Pressure (Torr)	Neutralization
5e-8	$0.7 \cdot 10^{-4}$
1e-7	$1.4 \cdot 10^{-4}$
5e-7	$7.2 \cdot 10^{-4}$

most certainly leave the beam region and hit the vacuum chamber if the gap is one microsecond or longer.

Chapter 5

EXPERIMENTAL RESULTS

The injection line of the ring and the dipole magnets D1-D4 was assembled and tested in April-May of 2003 [34]. The vacuum chamber of the ring was assembled by the end of October of 2003. Figure 5.1 shows a photograph of the SIR room taken on November 2, 2003.

The maximum current that we were able to reach in the dipole magnets of the ring with our power supply (EMI 135-20) was 130 A. This current corresponds to a maximum beam energy of 29.5 keV for the H_2^+ beam. The magnetic dipole and quadrupole correctors situated in the dipole magnets were powered to the full design current. The polarity and the level of the field produced by the correctors were checked. The electrostatic deflectors and the quadrupole correctors situated in the straight sections of the ring were tested up to 1000 V. The injection and extraction deflectors were tested up to 3.5 kV, voltage necessary for extraction of a 30 keV beam.

5.1 Vacuum in the ring

In the current setup, we use two 500 L/s turbo-pumps in the injection line and two 500 L/s turbo-pumps in the ring (see Figure 4.30). We started pumping down the
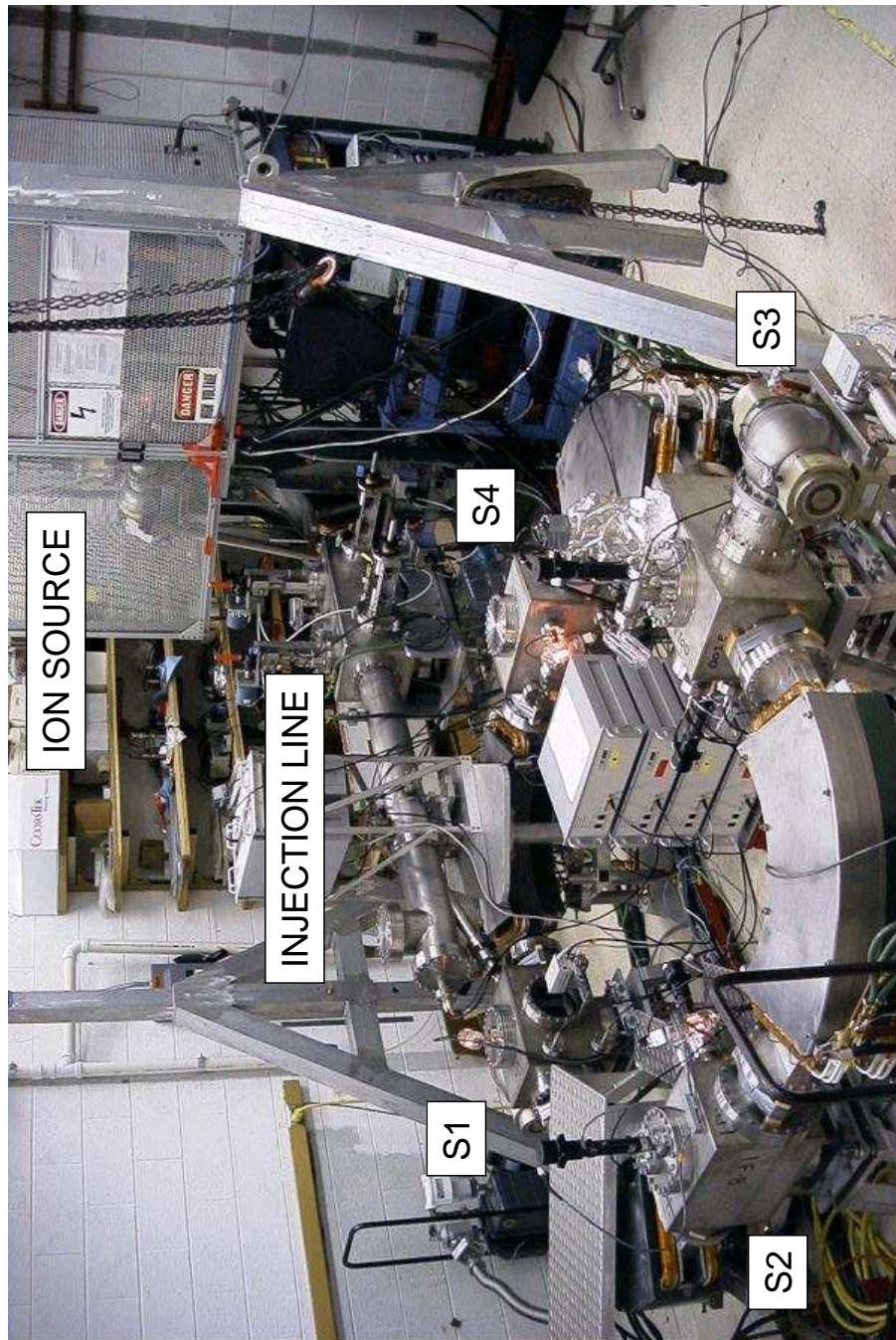
Figure 5.1: A photograph of the SIR ring and its injection line taken on 11/02/2003.

injection line in the middle of October of 2003. Approximately two weeks later, we started pumping down the ring. When pressure in the ring was still 100 times higher than that in the injection line, we opened the gate valve separating the injection line and the ring. The reading of the ion gauges in the injection line remained virtually unchanged, supporting our assumption made in section 4.7 neglecting the flux of the residual gas from the ring to the injection line.

Table 5.1 shows pressure of the residual gas read by ion gauges situated in the injection line and the ring. The gauge situated in the injection line was just below the ion source (point 1 in figure 4.30). The other three gauges were in straight sections of the ring S1, S2, and S4. Unfortunately, the pressure reading in the S3 drift was not available because the filament of the ion gauge burned out on the second day of pumping. The average pressure in the ring corresponding to the numbers shown in the table was approximately $4.5 \cdot 10^{-8}$ Torr, very close to the predicted value of $5.5 \cdot 10^{-8}$

Table 5.1: Residual gas pressure just below the ion source and in the S1, S2, and S4 straight sections of the ring. The regulated valve in the ion source was closed.

IG location	P(torr)
Inj. Line	$3 \cdot 10^{-8}$
S1	$3.5 \cdot 10^{-8}$
S2	$5.5 \cdot 10^{-8}$
S4	$4.5 \cdot 10^{-8}$

We have used hydrogen for all the experiments described below. Pressure in the ion source was setup using a Pirani gauge which was above the ion source and connected to the source by a 15 cm-long piece of standard Ø0.25 copper tube. Using a variable valve, we set the Pirani gauge reading to 10 mTorr in all our experiments. The real pressure at the location of the Pirani gauge was approximately 7 mTorr. (The Pirani gauges are calibrated for hydrogen and show higher pressure for hydrogen.) The corresponding pressure in the ion source was approximately 1.8 mTorr. The second column of Table 5.2 shows pressure read by the ion gauges. The ion gauges are usually calibrated for nitrogen or air. To adjust the reading, we have divided the difference due to hydrogen by 0.47 and then added the adjusted difference to numbers in table 5.1. The third column of table 5.2 shows the total, adjusted pressure. The total average pressure in the ring was approximately $1.0 \cdot 10^{-7}$ Torr. Changes of the source parameters (excluding the source pressure) had little effect on pressure in the ring. For example, turning on the discharge in the ion source changed the pressure in the ring by only about $1 - 2 \cdot 10^{-8}$ (adjusted) Torr.

The difference in the average pressure due to the flow of hydrogen from the ion source was approximately $5 - 5.5 \cdot 10^{-8}$ Torr. That is approximately 2.5 times higher than that expected from the calculations presented in section 4.7 and appendix E. This maybe related to the fact that the turbo-pumps used in the project (Pheiffer/Balzers TPU510) have a compression ratio of approximately 10^3 for hydrogen. Hence, if a ratio of the partial pressure of hydrogen in back-up lines to pressure of hydrogen in the ring reaches about 1000, the pumping speed of the pumps sharply

Table 5.2: Pressure read by the ion gauges and the total adjusted pressure in the injection line next to the ion source and in the S1, S2, and S4 straight sections of the ring. The chamber of the ion source was pressurized to approximately 1 mTorr.

IG location	P(Torr) READING	P(Torr) Tot. ADJUSTED
Inj. Line	$6 \cdot 10^{-7}$	$1.3 \cdot 10^{-6}$
S1	$8 \cdot 10^{-8}$	$1.3 \cdot 10^{-7}$
S2	$8 \cdot 10^{-8}$	$1.0 \cdot 10^{-7}$
S4	$7 \cdot 10^{-8}$	$1.0 \cdot 10^{-7}$

declines. The partial pressure of hydrogen in the back-up lines is a parameter that depends on the type of pumping oil used in roughing pumps. It can easily reach a level of milliTorrs and can limit the effective pumping speed. The compression ratio exponentially grows with the molecular weight of pumped gas. For deuterium, it exceeds 10000. That is why using deuterium instead of hydrogen may provide lower ring pressure should it be desirable.

The ion source can be operated at lower pressure in the source chamber. We have been able to operate the source with the chamber pressure equal to 0.5 mTorr. Though, a pressure of $0.8 - 1.0$ mTorr may be required for stable source operation.

5.2 First beam in the ring

5.2.1 Injection and the first turn

The first successful attempt to inject the beam onto the median plane of the ring was made in May of 2003 [34]. At that time, the beam was brought through the injection line and the first dipole D1 and dumped into a Faraday cup after a quarter of the ring. The Faraday cup registered an electrical current of approximately 60 μA. This reading included the current of secondary electrons. The real beam current was approximately 20 μA.

The first beam was injected onto the closed ring at the end of October of 2003. A DC H_2^+ beam was extracted from the ion source biased to 17 kV. The beam went through the injection line and was deflected into the ring by a set of deflector plates situated at the end of the injection line. At the entrance of the ring, the beam was detected by the phosphor screen situated in the straight section S1. (For a detailed description of the phosphor screen, see section 4.6.1.) The Figure 5.2 shows a photograph of the screen with a beam spot. After the phosphor screen has been lowered to the median plane, it immediately detected the beam after one turn. Figure 5.3 shows a photograph of the beam spot on the phosphor screen lowered to the median plane. No matching between the injection line and the ring was done due to the lack of cables from power supplies to the injection line quadrupoles. The beam was focused in the injection only by the Einzel lens situated right after the ion source and by the analyzing magnet. At the time of the experiment described here, the horizontal beam steering in the injection line was not fully operational either.

In the multi-turn experiments described below we could see coherent radial betatron oscillations with an amplitude of 1-1.5 cm.

5.2.2   First experience with the multi-turn operation

To inject the beam in the multi-turn mode, we enabled the timing system schematically shown in Figure 4.25. The length of the bunch was set to 1 μsec. The length of the inflector pulse was set to almost 3 μsec with almost zero delay after the chopper pulse. The length of the extraction pulse that controlled the voltage on the deflector plates situated in the straight section S3 was set to 2.5 μsec. The delay between the chopper pulse and the extraction pulse was varied from almost zero to approximately 220 μsec. The revolution period of the beam in the ring was approximately 5.1 μsec. The time required for the beam to travel from the chopper plates to the inflector plates was approximately 1 μsec. The voltage on the chopper, inflector, and deflector plates was 2.0 kV, the same as in the DC mode. The whole system had a repetition rate of 1 kHz.

When the delay time of the extraction pulse was equal to $(n + 0.5) \cdot T$, where n is an integer and T is the revolution period, the beam was extracted to the phosphor screen situated in the straight section S3 two inches above the median plane. (For a description of the phosphor screen, see section 4.6.1). Changing the delay time of the extraction, we could extract a given turn and see a beam spot on the phosphor screen. Figure 5.4 shows the beam spot on the screen after 2.5, 6.5, 10.5, 14.5, 18.5 and 20.5 turns. The total number of turns was 46, corresponding to the maximum available delay of 220 μsec . To observe more turns, a longer delay would be required.
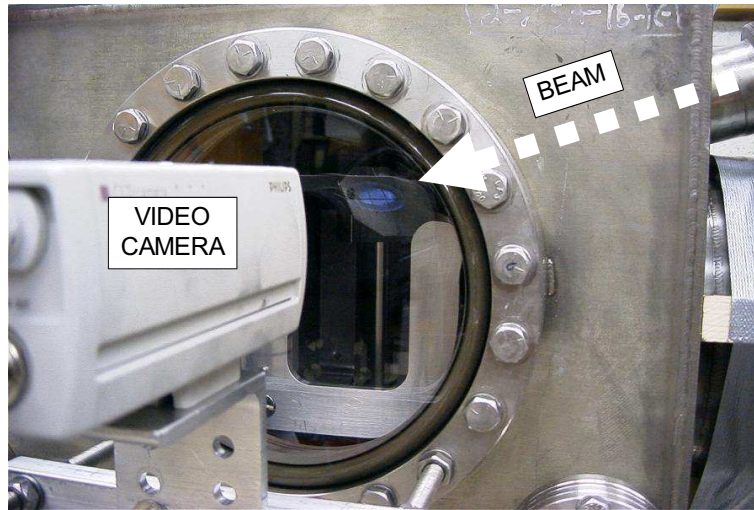
Figure 5.2: A photograph of the beam spot on a phosphor screen. The DC H_2^+ beam is intercepted by a phosphor screen on its way from the injection line to the ring. The energy of the beam is 17 keV. The beam current is approximately 25 μA.
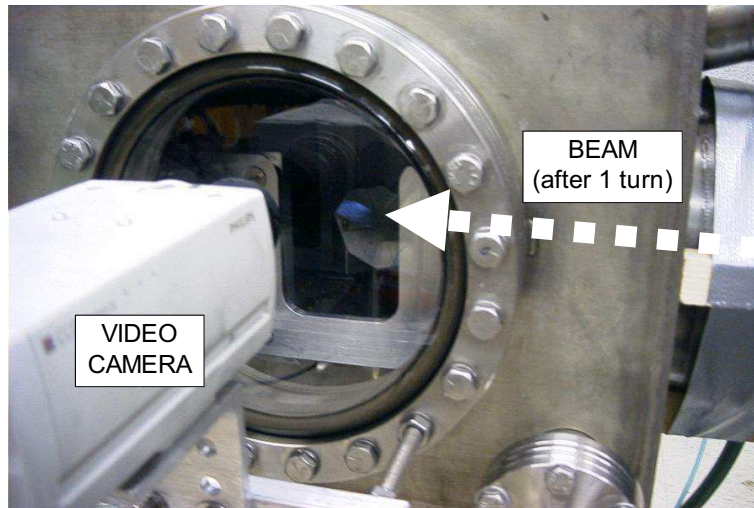
Figure 5.3: A photograph of the beam spot after a single turn. The phosphor screen is in the median plane. The injected beam passes above the phosphor screen.
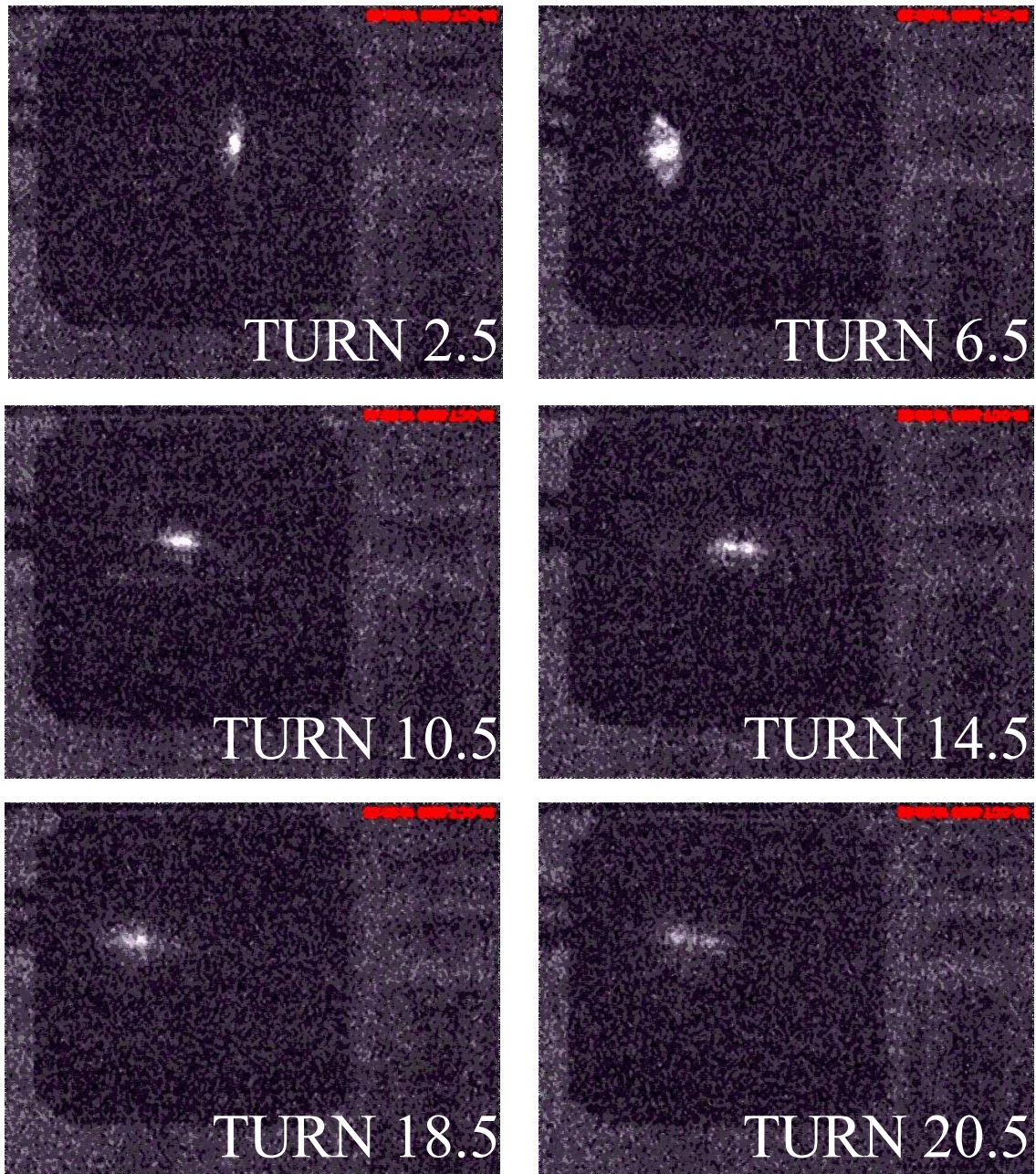
Figure 5.4: Beam spot produced by the extracted H_2^+ beam on the phosphor screen situated in the straight section S3. The peak beam current was approx 3.5 μA, beam energy 17 keV with a pulse length 1 μsec. The injection/extraction frequency was 1 kHz. Each frame is approximately 91 mm by 68 mm.

5.3 Measurement of the beam life time and betatron tunes

5.3.1 Beam life time

The electrical current of the extracted beam intercepted by the phosphor screen situated in the straight section S3 was read through an electrical feedthrough in the vacuum chamber. Figure 5.5 shows the average extracted beam current vs. turn number. Note that we increased the length of the injected bunches to 2 μsec, the injection frequency to 2 kHz, and the peak beam current to 20 μA to increase the current intercepted by the phosphor screen. The current read from the phosphor screen also included the current of the secondary electrons.
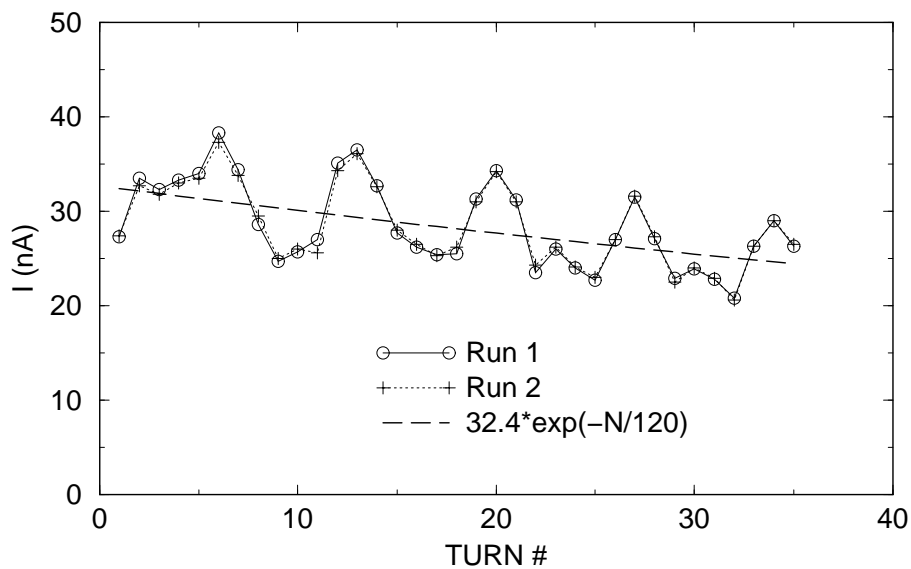
Figure 5.5: The average current read by the phosphor screen in the S3 drift. The experimental data (Run 1 and Run 2) was fitted with an exponential function with a decay time of 120 turns.

To separate systematic errors from noise we took the measurements twice. The curves corresponding to two different runs are almost identical and show large vari-

ations of current readings depending on turn number. The variation of the beam current readings from turn to turn was correlated with the motion of the beam spot on the phosphor screen due to the radial betatron oscillations. The intensity has maxima at turns 6, 13, 20, 27, and 34. The maxima are separated by 7 turns that approximately coincides with the number of turns required for the beam to make one complete radial oscillation on the phosphor screen. (See next section for measured betatron frequencies.) The correlation of the current reading with the beam spot position may be explained by variation of quality of the phosphor screen surface and, as a result, variation of the efficiency of the secondary electron emission.

The dashed line shows the exponential function fitted to the measured data. The decay time of the fitted curve is 120 turns. Assuming that all the losses are due to electron pick-up from the residual gas, we can estimate the average pressure as $2.6 \cdot 10^{-7}$ Torr. At the moment of the experiment, the average pressure measured by ion gauges was $1.2 \cdot 10^{-7}$ Torr

5.3.2 Betatron tunes

The injected beam oscillates in the ring around the closed orbit. If the oscillating beam is extracted, the position of the beam spot on the phosphor screen also oscillates (see figure 5.4). Measuring the displacement of the beam spot on the phosphor screen in S3, we have calculated the betatron tunes. To improve the accuracy of the calculations we fitted a sine curve to the data and found its amplitude, phase, and frequency.

First, we injected a beam with radial oscillations and calculated the radial betatron frequency as described above. Figure 5.6 shows the horizontal displacement of the

144

beam spot on the phosphor screen and the fitted sine function. The fractional part of the radial betatron frequency calculated from the fit was 0.142, very close to the predicted value. The radial tune calculated in the TOSCA field was 1.143. The value of the radial tune calculated using the measured magnetic field was 1.140.
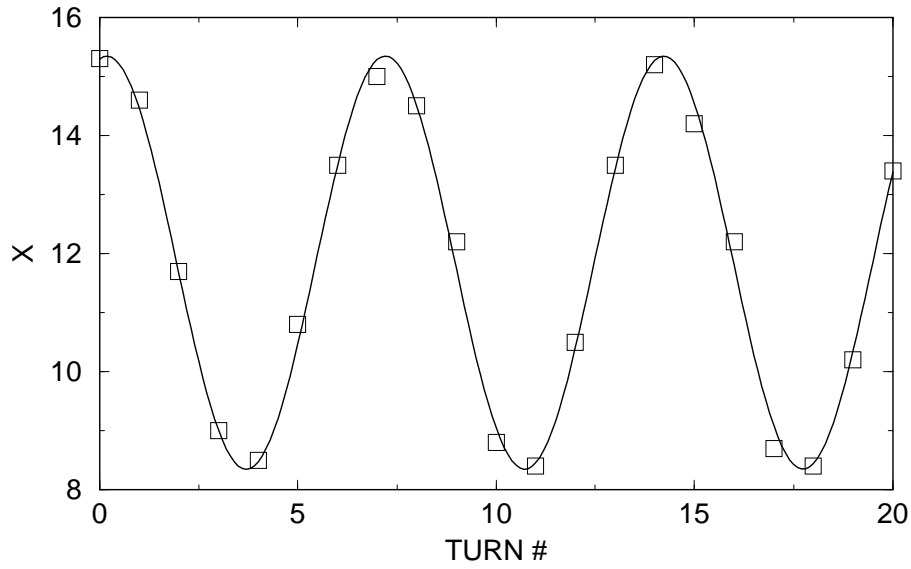
Figure 5.6: The horizontal position of the beam spot on the phosphor screen vs. turn number. The solid line shows the fitted sine wave. The period of the fitted sine wave is almost equal to 7 turns. The graph shows the beam displacement on the phosphor screen. The actual amplitude of the beam oscillations on the phosphor screen was approximately 10 mm.

To measure the vertical tune, we have minimized the amplitude of the radial oscillations and displaced the beam coming from the injected line vertically. Figure 5.7 shows the vertical excursion of the beam spot on the phosphor screen and the fitted sine curve. The vertical tune calculated from the fit was 1.11. This value coincides with the betatron frequency calculated using the measured magnetic field, but is lower than the frequency of 1.128 calculated in the TOSCA field.
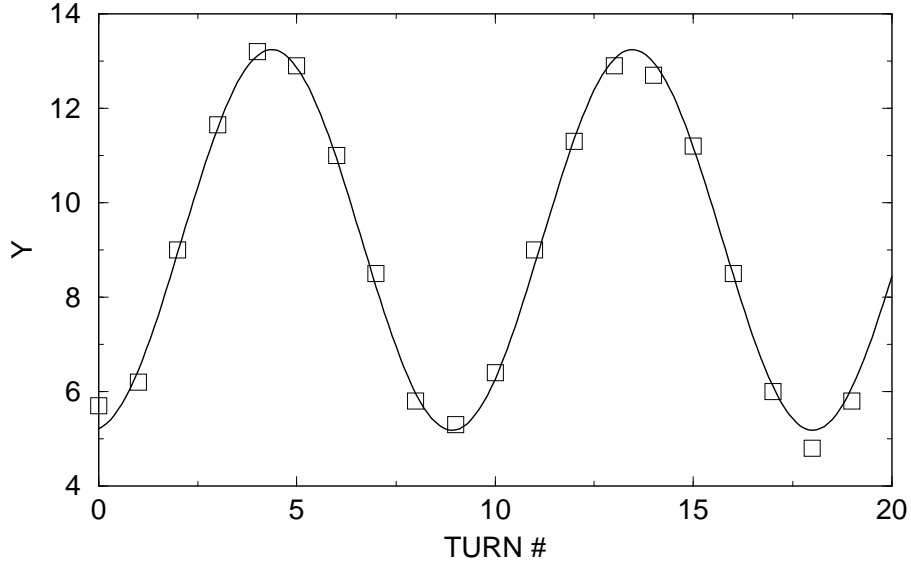
Figure 5.7: The vertical position of the beam spot vs. turn number. The solid line shows the fitted sine wave. The period of the fitted sine wave is almost equal to 9 turns. The graph shows the beam displacement on the phosphor screen. The actual amplitude of the vertical betatron oscillations was 12 mm.

5.4 Test of scanning wire monitors

5.4.1 DC regime

To test the scanning wire monitors, we injected a DC 4.5 μA H_2^+ beam in the ring. The voltage on the chopper and inflector plates was not pulsed. Using the vertical and horizontal scanning wire monitors situated in the straight section S2, we measured the beam profile. Figures 5.8 and 5.9 shows the measured vertical and horizontal beam profiles. After increasing the voltage on the inflector plates by 1.8% (35 V), the beam moved up by approximately 4.1 mm at the location of the vertical monitor in the S2 drift (see figure 5.8). The analytically estimated value of the shift under this conditions was equal to 4.4 mm.

The other two wire monitors situated in the straight section S3 were tested to
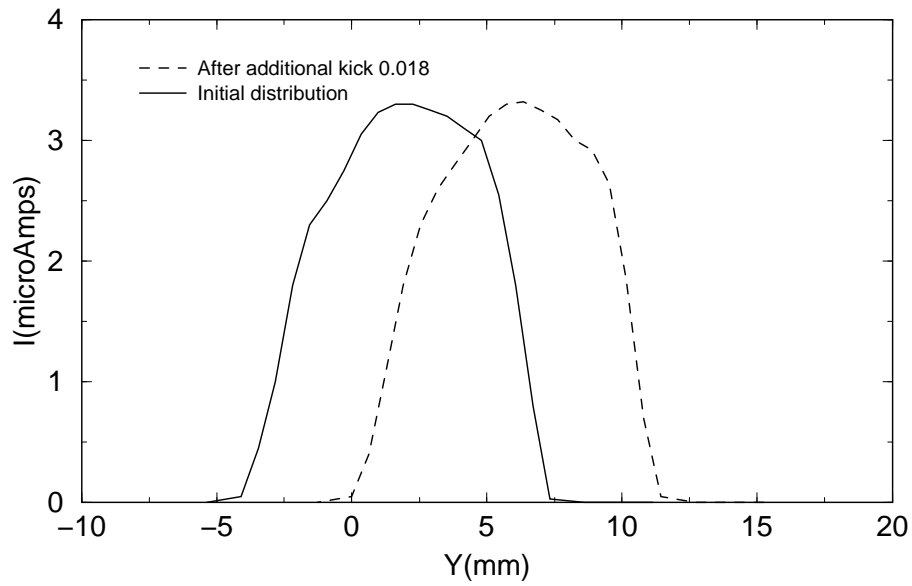
Figure 5.8: Two vertical profiles of the 4.5 μA DC beam measured by the vertical scanner situated in the S2 drift. We have changed the voltage on the inflector by 35 V (1.8%) to modify the vertical position.
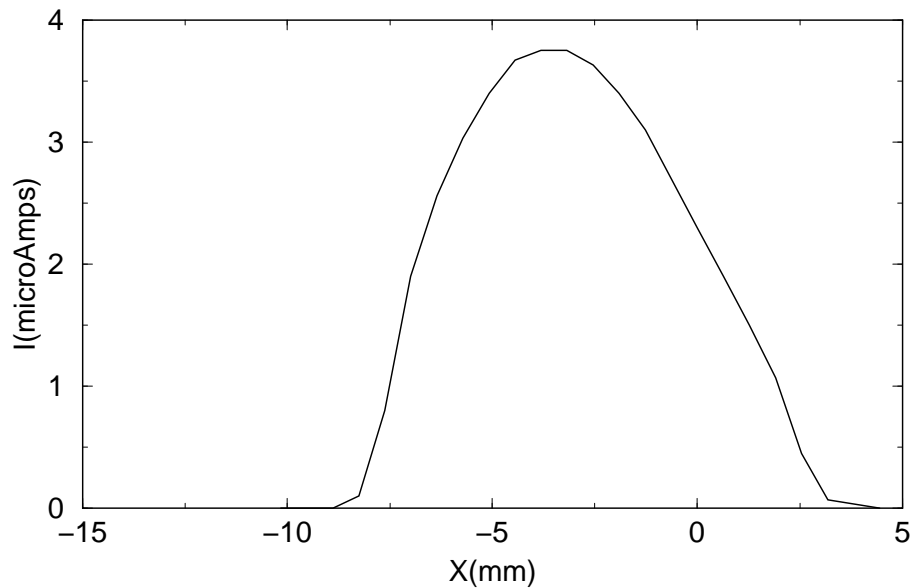
Figure 5.9: The horizontal profile of the 4.5 μA DC beam measured by the horizontal wire scanner situated in S2 drift.

ensure their functionality

The wire monitors can be used to adjust the injection of the beam in the ring in the DC mode. By adjusting the voltage on the inflector and the deflector plates in the injection line and monitoring the vertical beam displacement with the wire scanners, we can set the trajectory of the injected beam in the median plane. Horizontally centering the first turn trajectory requires using the phosphor screen in the section S1 after the first turn. The third observation spot is required because there are three parameters (three variables) in the horizontal plane: horizontal injection angle, horizontal injection coordinate, and the magnetic field field of the ring. Thus, we need three points of observation (three equations) to adjust the first turn trajectory.

5.4.2 Pulsed mode

Although setting the first turn trajectory to calculated parameters is a good first approximation, it does not guarantee placing the beam on the equilibrium orbit. The equilibrium orbit in the ring (the closed solution of the equations of motion) can be different from the predicted one because of errors in the magnetic field. The scanning wire monitors can be used to monitor the position of the closed orbit. Moreover, they can be used to monitor the amplitude of the residual betatron oscillations after injection.

Figure 5.10 shows two current profiles measured by the vertical wire scanner situated in the straight section S2. The beam was injected in the pulsed mode. The length of the bunch was 1 μsec, the peak current was 4.5 μA, and the injection repetition rate was 1 kHz. The beam was not deflected from the ring. The beam current

intercepted by the wire scanner was read by a picoammeter. Because of picoamme-
ter's slow response the current was integrated to obtaing the average DC current at
a given position.

First, we injected the beam with the amplitude of the vertical betatron oscillations
equal to approximately 10 mm. (Before measuring the profile, we changed the voltage
on the inflector to induce vertical oscillations. We monitored the amplitude of the
oscillations on the phosphor screen in the S3 drift. After adjusting the inflector
voltage, we turned off the extraction deflector, and let the beam rotate in the ring
and made the scans.) The solid-line curve shows the current profile of the mismatched
beam. This curve has a plateau in the region $y \approx 0.0\pm8$ mm. The coordinate of the
plateau center is the coordinate of the equilibrium orbit and the width of the plateau
is the amplitude of the betatron oscillations of the beam centroid.

The vertical position of the beam measured at a given azimuth oscillates between
coordinates $z_{eq} - a_z$ and $z_{eq} + a_z$, where z_{eq} is the the coordinate of the equilibrium
orbit and a_z is the amplitude of the betatron oscillations of the beam centroid. If the
beam is not on a resonance, it will eventually pass through all the points between
$z_{eq} - a_z$ and $z_{eq} + a_z$. Thus, the scanner wire located anywhere between $z_{eq} - a_z$ and
$z_{eq} + a_z$ will eventually intercept all the particles of the beam. If the wire displacement
from the equilibrium orbit is larger than a_z but the beam still touches the wire, the
wire will intercept only a fraction of the beam. The remainder of the beam will be
lost because of collisions with molecules of the residual gas or will be removed by
following injection pulses. Finally, if the wire is far enough from the equilibrium orbit

to clear the beam, the current read by the wire will be zero. The finite life-time will manifest itself as a non-flat plateau. In the case of infinite life-time, the plateau must be flat.

The dashed curve of figure 5.10 shows the current profile of the beam with small vertical betatron oscillations. We have minimized the amplitude of the vertical oscillations before measuring the current profile. (For this, we have adjusted the voltage on the inflector and monitored the position of the beam spot of the extracted beam on the phosphor screen in the drift S3.) The coordinate of the center of the dashed curve is the coordinate of the equilibrium orbit. According to the previous paragraph, both curves should have the same height. Finding an explanation for this disagreement requires additional work. The main challenge is an accurate measurement of the intensity of the mismatched beam.
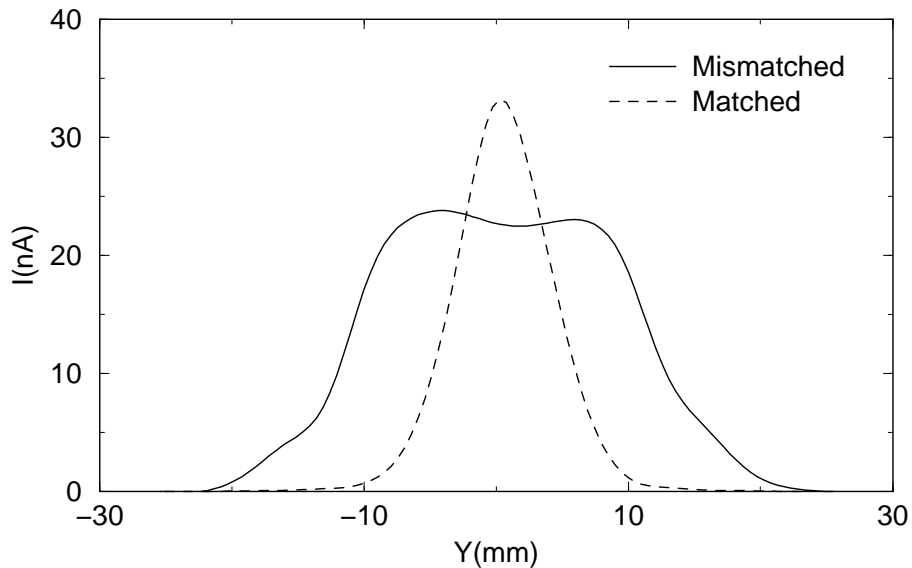
Figure 5.10: Current profiles measured by the vertical wire scanner in the S2 drift. The solid curve shows the profile of the beam with larger amplitude of vertical oscillations. The dashed curve shows the profile of the beam with smaller vertical oscillations.

5.5   First indication of space charge effects

By increasing the arc discharge current in the multi-cusp ion source, the beam peak current was increased to 20 μA. The chopper produced one-microsecond-long bunches out of the DC beam. The bunches were injected into (and extracted from) the ring with a frequency of 1 kHz. The figure 5.11 shows the beam spot on the phosphor screen in the straight section S3 for different extracted turns. The radial beam size increases with the turn number. The beam spot also shows a tilt with respect to the horizontal plane. Together these two effects are indicative of a rapid increase in the energy spread of the beam.

The vertical angle produced by the extraction deflector depends on the particle energy. The dependence of the deflection angle on the energy causes particles with different energies to hit the phosphor at different heights. The difference in the height can be described by the formula

$$\delta y = \delta\alpha\, l = -\alpha\frac{\delta E}{E}l = -y_0\frac{\delta E}{E} \tag{5.1}$$

where δE is the energy deviation from the equilibrium energy E, α is the deflection angle of the equilibrium particle with $\delta E/E = 0$, l is the distance between the deflector and the phosphor screen, and y_0 is the vertical coordinate of the equilibrium particle hitting the screen. In calculating δy, we assumed that the deflection angle α is small so that $\tan(\alpha) \approx \alpha$.

The orbit of a particle with the energy deviation equal to $\delta E/E$ is horizontally displaced from the orbit of the equilibrium particle by
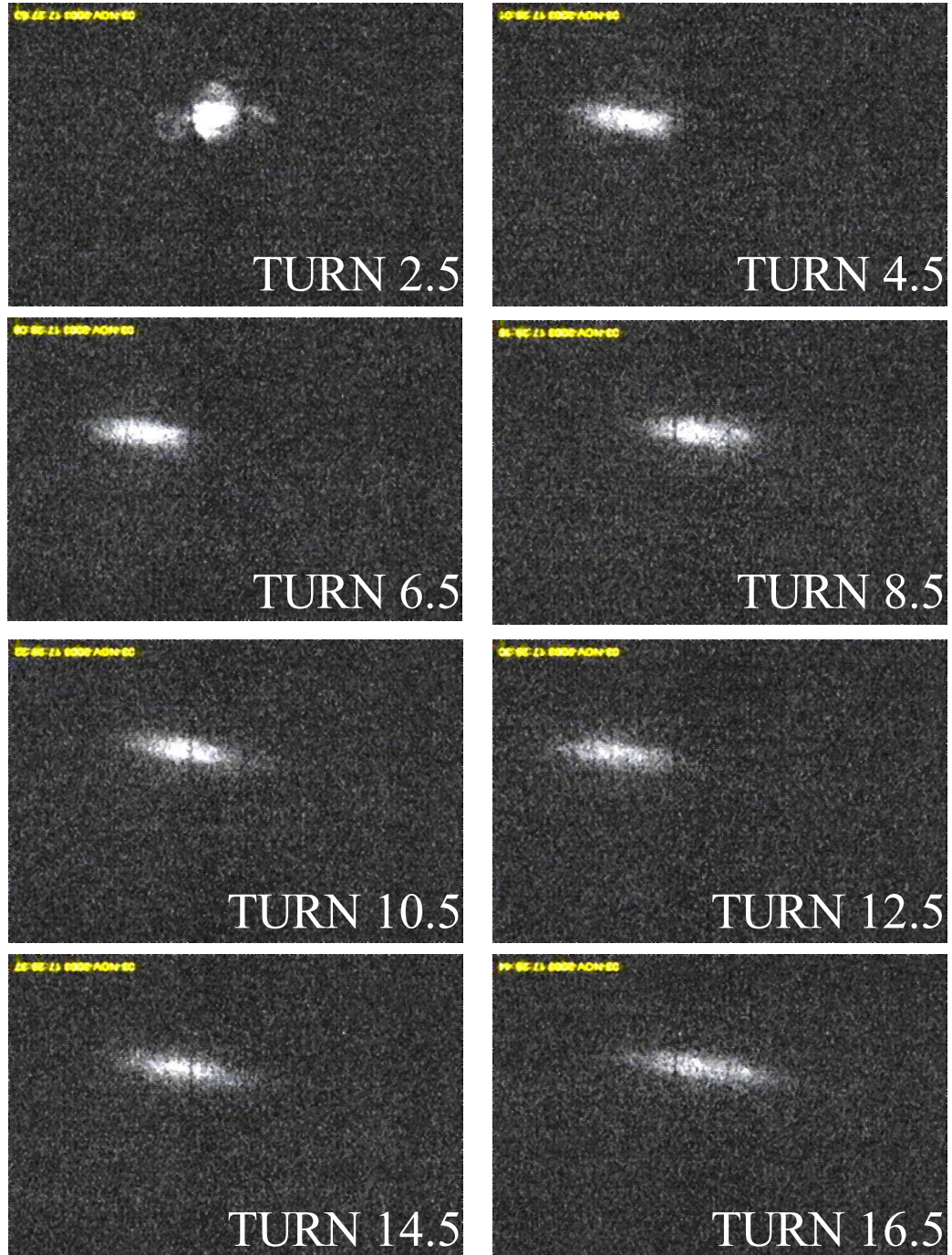
Figure 5.11: Beam spot produced by extracted H_2^+ beam on the phosphor screen situated in the straight section S3. The peak beam current was approx 20 μA, beam energy 17 keV, and a pulse length 1 μsec. Each frame is approximately 83 mm by 56 mm.

$$\delta x = \eta \frac{\delta p}{p} = \eta \frac{\delta E}{2E} \tag{5.2}$$

where p is the momentum and η is the dispersion function.

The correlation between the vertical displacement δy and the horizontal displacement δx manifests itself as a tilt of the spot of the extracted beam. The tangent of the tilt angle is

$$\tan(\theta) = \frac{\delta y}{\delta x} = -2\frac{y_0}{\eta} \tag{5.3}$$

The vertical displacement y_0 on the phosphor screen is approximately 58 mm and η is equal to 932 mm (see section 3.2.2), yielding a tilt angle of approximately 7.1°. A possible error in this analysis comes from the uncertainty of the position of the vertical beam orbit before the beam was deflected onto the phosphor screen. This error could be several millimeters. The error in the phosphor screen alignment did not exceed ±0.5°.

Figure 5.12 shows the spot of the beam extracted after 16.5 turns (the last turn in the figure 5.11). The visible width of the beam spot is approximately 34 mm. The line going through the spot is rotated by 7.1°, approximately the same tilt as the bunch, implying that the beam size grows primarily because of energy spread growth. If the beam size growth was due to the beam emittance dilution, the beam spot of the extracted beam would not be tilted.

We can estimate the energy spread within the beam expressing the beam size as a sum of the emittance related term and the energy related term:
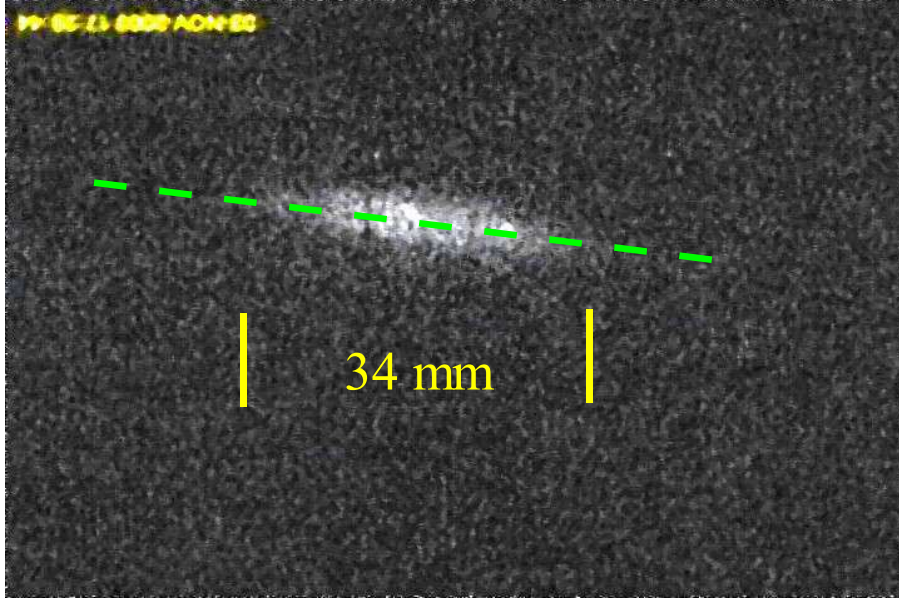
Figure 5.12: The beam spot of the beam extracted after 16.5 turns. The width of the beam is approximately 34 mm. The tilt of the beam spot is approximately 7.1°.

$$x = x_\beta + \eta \frac{\delta E}{2E} \tag{5.4}$$

The emittance related term, x_β, is estimated from the first frame of the figure 5.11 (turn 2.5) as 10 mm. Thus, the last equation yields an estimate of the energy spread in the last turn equal to

$$\frac{\delta E}{E} = 2 \frac{x - x_\beta}{\eta} = 2 \frac{24}{932} = 5\% \tag{5.5}$$

Here we assumed that the emittance related term does not substantially grow in 16 turns.

Using the program MATHCAD [35], we obtained the horizontal (radial) distribution of the beam spot intensity on the phosphor screen pictures and compared the measured distribution to that predicted by CYCO. The left column of figure 5.13

154

shows the beam spot after turns 2.5, 6.5, 10.5, and 14.5 and is identical to the left column of figure 5.11. The right column shows the digitized horizontal distribution of intensity of corresponding pictures of the left column. The digitized distribution on the right pictures was centered and the horizontal scale of the pictures was reduced from 83 mm to 60 mm. The pictures of the right column also contain the radial beam distribution predicted by CYCO. The experimental and simulation results qualitatively agree with each other. This can be considered as another indication of the strong longitudinal-radial space effect that induces a rapid increase in the energy spread of the beam.
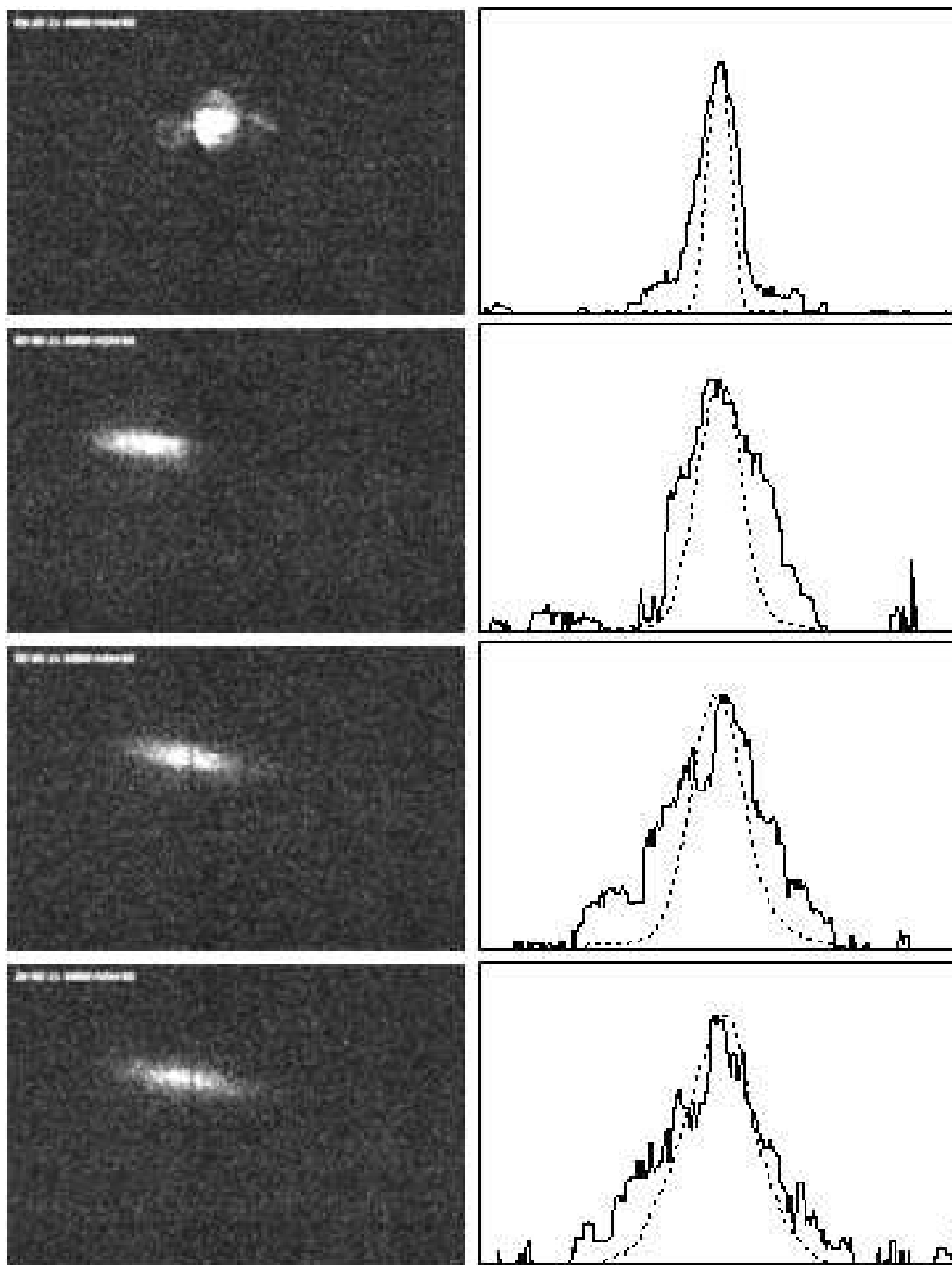
Figure 5.13: LEFT COLUMN: pictures of the beam spot on the phosphor screen after turns 2.5, 6.5, 10.5, and 14.5. The horizontal size of the pictures is 83 mm. RIGHT COLUMN: The measured (solid curve) and simulated (dashed curve) horizontal beam profiles for turns 2.5, 6.5, 10.5, and 14.5. The measured beam profile was obtained by digitizing corresponding pictures of the left column. The measured distribution was centered. The scale of the pictures was reduced to 60 mm. The simulated distribution was calculated by CYCO.

Chapter 6

CONCLUSION

6.1 Code CYCO

The program CYCO has been developed. Developing the code, we paid special attention to a realistic treatment of the beam dynamics:

- The code tracks particles in a calculated or measured 3D magnetic map, solving the complete system of the six equations of motion.

- The code realistically treats acceleration, modeling the RF system as a set of infinitely thin accelerating gaps. The gaps are not limited to any specific shape and are provided in a file by a user as a tabulated function of $R(\theta)$. Each gap can have its own voltage, frequency, and initial phase.

- CYCO uses the Particle-in-Cell method to calculate the space charge field of the beam. Solving the Poisson equation, the code includes the effect of the image charges induced on the vacuum chamber.

- The code includes the effect of the neighboring bunches.

The tracking part of the code was tested and the results were compared to SPI-RALGAP. The field solver was extensively used for simulations of the space charge effects in SIR. We are eager to compare the results of the simulations to experimental data that we expect to collect at SIR. Additional validation efforts through a comparison to other programs are required.

A first-priority upgrade of the code can include development of a space charge field solver that would be able to include the relativistic effects.

6.2   The Small Isochronous Ring

The Small Isochronous Ring has been developed. Almost all the main subsystems of the ring, including the dipole magnets, quadrupole and steering correctors, wire-scanners, phosphor screens, injection-extraction system, and the vacuum chamber have been tested. We have injected the beam in the ring and measured such important parameters as betatron tunes and the beam life-time. The measured values of the betatron tunes were very close to predicted values. The measured beam life-time was 120 turns.

The beam with a peak current of 20 μA has shown a fast growth of the radial beam size. This fast size growth is indicative of a strong longitudinal space charge effect that increases the energy spread within the bunch. To further investigate the longitudinal space charge effects we need to install the fast Faraday cup in the ring.

The other near-term plans include the improvement of matching between the injection and the ring and installation of an image-intensifying camera in the S3

drift.

Appendix A

SCALING LAWS FOR SPACE CHARGE

EFFECTS

As shown by M. Gordon [6], Space Charge (SC) forces induces a vortex motion in the beam. The longitudinal component of the SC force increases/decreases the energy of head/tail particles. This causes the beam to tilt. The transverse component of the force shifts the particle radius but does not change its velocity. This causes the particle to slip in phase. Thus, the beam is continuously involved in a vortex motion.

A.1 Radius change due to energy deviation induced by the longitudinal component of the space charge force

In isochronous cyclotrons, the dispersion function deviates little from its average value. For example, η deviates from its average value by $\pm 5\%$ in SIR. For the sake of simplicity, we assume that the dispersion function does not vary along a particle trajectory displacement and is equal to its average value.

The rate of particle radius change can be expressed as

$$\frac{dx}{d\theta} = \eta \frac{dp/p}{d\theta} \qquad (A.1)$$

where θ is generalized azimuthal angle.

The derivative of particle momentum over time is

$$\frac{dp}{dt} = qE_{||} \qquad (A.2)$$

Dividing both parts of Equation A.2 by the angular frequency of particle rotation

we get

$$\frac{dp}{d\theta} = \frac{qE_{||}}{\omega} \qquad (A.3)$$

In the isochronous regime, the slip factor, $(p\,dT)/(T\,dp)$, where T is the revolution

period, is equal to zero.

$$\frac{p}{T}\frac{dT}{dp} = \frac{p}{T\,dp}\frac{v\,dC - C\,dv}{v^2} = \frac{p}{dp}\left(\frac{dC}{C} - \frac{dv}{v}\right) = 0 \qquad (A.4)$$

where C is the circumference of the trajectory and v is the particle velocity.

$$\frac{dC}{C} = \frac{1}{C}\int ds \frac{\eta}{\rho}\frac{dp}{p} = \frac{\eta}{R}\frac{dp}{p} \qquad (A.5)$$

where R is an average radius of the trajectory, ds is the path along the trajectory.

dv/v is

$$\frac{dv}{v} = \frac{1}{\gamma^2}\frac{dp}{p} \qquad (A.6)$$

Substituting Equations A.5 and A.6 in Equation A.4 we obtain

$$\eta = \frac{R}{\gamma^2} \tag{A.7}$$

Using the expression for the momentum $p = \gamma m R \omega$ and Equations A.3 and A.7 we rewrite Equation A.1 as

$$\frac{dx}{d\theta} = \frac{1}{\gamma^3} \frac{qE_\|}{m\omega^2} \tag{A.8}$$

The longitudinal component of the space charge field is proportional to the total charge of the bunch:

$$E_\| = g_\| \frac{Q}{\gamma^2} = 2\pi g_\| \frac{I}{\gamma^2 h \omega} \tag{A.9}$$

where I is total beam current and h is the harmonic number. The geometrical factor $g_\|$ includes dependence on the bunch shape, bunch charge distribution, and particle position within the bunch. Using Equation A.9 for the longitudinal component of the field, we finally obtain the rate of radius change due to energy deviation induced by the space charge force

$$\frac{dx}{d\theta} = 2\pi g_\| \frac{qI}{\gamma^5 m h \omega^3} \tag{A.10}$$

A.2 Longitudinal slip induced by the radial component of the space charge force

The equilibrium orbit of a particle with deviated energy is shifted radially relatively to the center of the bunch. Thus, an average value of the radial component of the

space charge force affecting the particle is different from zero. The radial component of the space charge force changes the equilibrium radius of a particle trajectory. To calculate an average displacement of the trajectory we use the equation of particle oscillations with the focusing force substituted by its average value over a turn:

$$\ddot{x} + \nu^2\omega^2 x = \frac{F_\perp}{\gamma m} \qquad (A.11)$$

The transverse force consists of the electric part and the magnetic part. The magnetic part of the force decreases the effect of the electric part. The net force can be written as

$$F_\perp = \frac{qE_\perp}{\gamma^2} \qquad (A.12)$$

This yields Equation A.11 in the form of

$$\ddot{x} + \nu^2\omega^2 x = \frac{qE_\perp}{\gamma^3 m} \qquad (A.13)$$

The equilibrium solution of this equation is

$$x = \frac{qE_\perp}{\gamma^3 \nu^2 m \omega^2} \qquad (A.14)$$

As in the previous paragraph, we express the transverse electric field through the total charge of a bunch

$$E_\perp = g_\perp Q = 2\pi g_\perp \frac{I}{h\omega} \qquad (A.15)$$

163

where the geometrical factor $g_\perp$ depends on the beam shape, bunch charge distribution, and radius of equilibrium orbit relative to the center of the bunch.

Replacing $E_\perp$ from Equation A.15 into Equation A.14, it yields

$$x = 2\pi g_\perp \frac{qI}{\gamma^3 \nu^2 mh\omega^3} \tag{A.16}$$

The transverse force shifts the particle off the equilibrium orbit but does not change the particle energy and velocity. This causes the particle with displaced orbit to slip in phase. The separation between a particle on the equilibrium orbit and a particle on the shifted orbit will grow as

$$ds = (R + x)\, d\theta - R\, d\theta = x\, d\theta \tag{A.17}$$

This yields the rate of longitudinal slip under the transverse space charge force

$$\frac{ds}{d\theta} = 2\pi g_\perp \frac{qI}{\gamma^3 \nu^2 mh\omega^3} \tag{A.18}$$

In isochronous cyclotrons, the radial betatron tune is approximately equal to the relativistic factor γ. Substituting γ for ν we obtain

$$\frac{ds}{d\theta} \approx 2\pi g_\perp \frac{qI}{\gamma^5 mh\omega^3} \tag{A.19}$$

A.3   Laslett tune shift in long bunches

The transverse space charge electric field in a long bunch with a round cross-section is

$$E = \frac{\lambda x}{2\pi\epsilon_0 a^2} \tag{A.20}$$

where λ is the linear charge density, x is a radial displacement of a particle in the bunch, and a is the radius of the bunch.

The magnetic field reduces the net transverse force

$$F = \frac{q\lambda x}{2\pi\epsilon_0 a^2 \gamma^2} \tag{A.21}$$

The equation of betatron oscillations, with the focusing force averaged over a turn, can be written as

$$\frac{d^2 x}{d\theta^2} + \left(\nu^2 - \frac{1}{2\pi\epsilon_0 a^2} \frac{q\lambda}{\gamma^3 m\omega^2} \right) x = 0 \tag{A.22}$$

Assuming that the tune shift is small we can write

$$\frac{\delta\nu}{\nu} \approx \frac{1}{4\pi\epsilon_0 a^2} \frac{q\lambda}{\gamma^3 \nu^2 m\omega^2} \tag{A.23}$$

The linear charge density is proportional to the total charge of the bunch

$$\lambda = g_\lambda Q \tag{A.24}$$

The geometrical factor g_λ depends on the longitudinal beam profile and particle position. g_λ is $1/l$ for a rectangular distribution of length l and $(1 - |\xi|/d)/d$ for a triangular distribution of total length of $2d$, where ξ is longitudinal position of the particle.

Using Equation A.24 and expanding Q as $2\pi I/h\omega$, we can write the Laslett tune shift as

$$\frac{\delta\nu}{\nu} = \frac{g_\lambda}{2\pi\epsilon_0 a^2} \frac{qI}{\gamma^3\nu^2 m h\omega^3} \qquad (A.25)$$

Again, using the approximate equality $\nu \approx \gamma$ we can rewrite Equation A.25

$$\frac{\delta\nu}{\nu} \approx \frac{g_\lambda}{2\pi\epsilon_0 a^2} \frac{qI}{\gamma^5 m h\omega^3} \qquad (A.26)$$

Appendix B

ISOCHRONOUS CONDITION FOR

LOW-ENERGY RINGS CONSISTING OF

FLAT-FIELD DIPOLE MAGNETS WITH THE

EDGE FOCUSING

Let's assume that a ring consists of N flat-field dipole magnets with the edge focusing. Figure B.1 shows a half of a period of the ring.

Let's assume that a particle with the equilibrium energy has the radius R in the magnet. The half-drift length for the particle is L. Let's assume that a particle with deviated energy has the radius R_1 and the half-drift L_1. The condition of isochronism can wrtitten as

$$\frac{R\frac{\pi}{N} + L}{v} = \frac{R_1\frac{\pi}{N} + L_1}{v_1} \tag{B.1}$$

Using the formula for the radius of the particle trajectory in the magnetic field (in CGS)

$$r = \frac{pc}{qB}$$
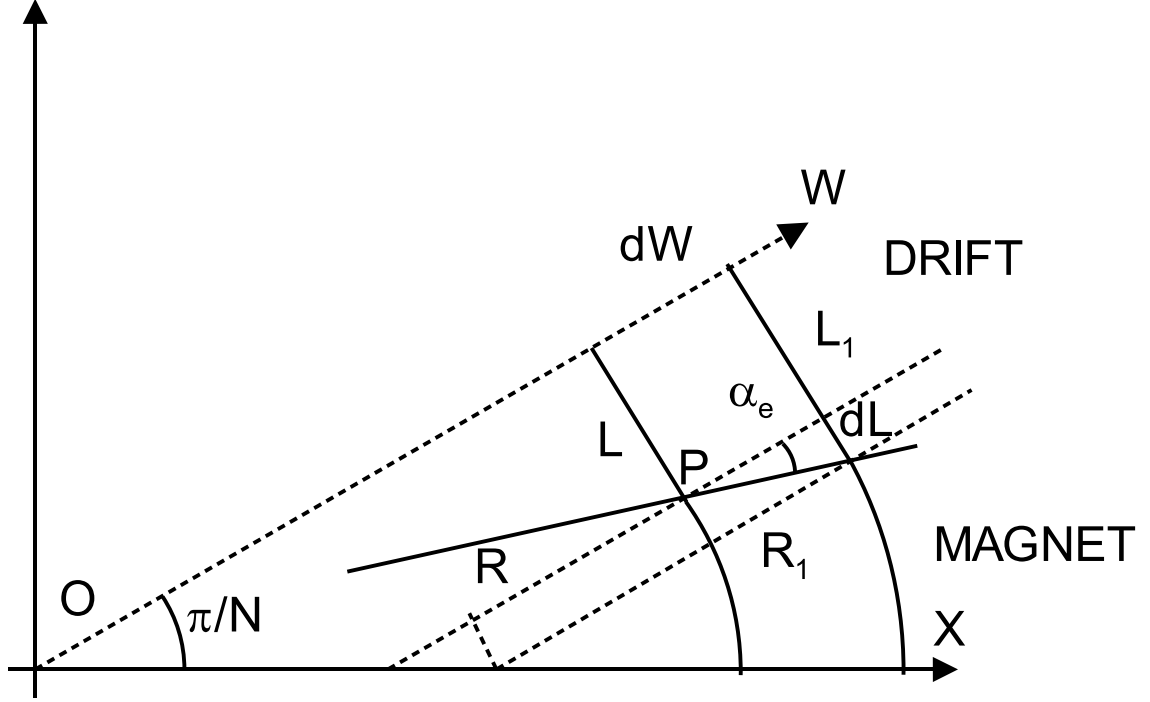
Figure B.1: A half of a period of a low-energy ring consists of a half of a magnet and half of a drift. The ring center is shown by the point O. The line X connects the center of the ring and the center of the magnet. The line W points from the center of the ring to the center of the drift.

in the low-energy limit, we can rewrite Equation B.1 as

$$\frac{R\frac{\pi}{N} + L}{R} = \frac{R_1\frac{\pi}{N} + L_1}{R_1} \tag{B.2}$$

After using some elementary algebra, we can write Equation B.2 as

$$LR_1 = L_1 R \tag{B.3}$$

L_1 and R_1 can be expressed via L and R as

$$L_1 = L + dL \tag{B.4}$$

$$R_1 = R + dW - \frac{dL}{\tan\left(\frac{\pi}{N}\right)} \tag{B.5}$$

where dW is the trajectory shift in the drift between magnets. Plugging Equations B.4 and B.5 in Equation B.3 we obtain, after some algebra,

$$\tan\left(\alpha_e\right) = dL/dW = \frac{L}{R + \dfrac{L}{\tan\left(\frac{\pi}{N}\right)}} \tag{B.6}$$

The angle between the line W and the line connecting the machine center O and the point P, where the equilibrim particle leaves the magnet, is equal to

$$\operatorname{atan}\left(\frac{L}{R + \dfrac{L}{\tan\left(\frac{\pi}{N}\right)}}\right)$$

Thus, the angle between W and P and the edge angle α_e are equal. This means that the edge of the magnet at the point P points at the center of the ring O. Since the point P was an arbitrary choice, the previous statement will be true for all points of the magnet edge. Thus, we conclude that a low energy ring consisting of flat-field magnets with the edge focusing is isochronous if the edges of its magnets point at the center of the ring.

If L denotes the whole drift, Equation B.6 has to be changed to

$$\tan\left(\alpha_e\right) = \frac{L/2}{R + \dfrac{L/2}{\tan\left(\frac{\pi}{N}\right)}} \tag{B.7}$$

Appendix C

COMPENSATION OF THE TUNE

CHROMATISM

Sextupoles, if inserted in the ring, can substantially reduce the tune spread caused by an energy spread. Figure C.1 shows the tune diagram for a beam with energy spread ± 1 keV under the condition of no sextupole in the ring and when a single electrostatic sextupole is inserted in the middle of one of the straight sections. The sextupole strength was 4.56 V/cm^3; the length of the sextupole was 5 cm. The tune shift produced by the sextupole was estimated as

$$\delta \nu_{x,y} = \pm \frac{\beta_{x,y}}{4\pi} \frac{qL}{2E} S \eta \frac{\delta p}{p} \tag{C.1}$$

where q is the particle charge, E is the particle energy, L is the length of the sextupole, S is the strength of the sextupole, and $\delta p/p$ is the particle momentum deviation.

It is better to use four identical sextupoles situated in four sections of the ring. This scheme has a smaller impact on the optical functions of particles with non-zero energy deviation. A more complicated scheme with four sextupoles located in the middle of the straight sections and four other closer to the dipoles would compensate the tune chromatism even better.
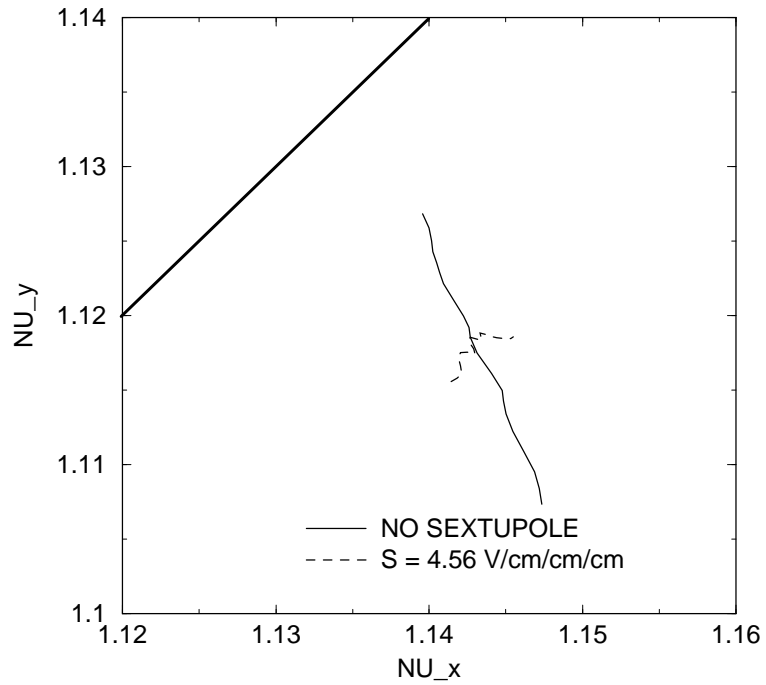
Figure C.1: A footprint of the beam on the tune diagram without sextupole and with a sextupole inserted in one of the straight sections. The beam energy spread is equal to ± 1 keV. The strength of the sextupole was 4.56 V/cm and the effective length was 50 mm. The line in the left upper corner shows the $\nu_x - \nu_y = 0$ resonance.

Appendix D

RAW DATA FOR THE 0-130-0A HYSTERESIS

LOOP

All measurements were done in the injection dipole. The field was measured by an NMR probe situated inside the magnet. The magnetic field was cycled 10 times from 0 to 130 A and back to 0 before the field was measured. The table D.1 contains field measurements taken on the 11th and 12th cycles.

Table D.1: Raw data for the 0-130A hysteresis loop.

CYCLE 11				CYCLE 12			
DOWN		UP		DOWN		UP	
I(A)	B(G)	I(A)	B(G)	I(A)	B(G)	I(A)	B(G)
130.39	727.42	129.605	723.02	130.371	727.36	129.483	722.29
127.134	710.35	127.163	709.41	127.200	710.67	127.127	709.23
124.359	695.52	124.433	694.29	124.413	695.78	124.443	694.37
122.108	683.38	121.988	680.71	121.930	682.41	122.034	680.98
119.045	666.78	119.668	667.82	119.667	670.12	120.217	670.89
117.104	656.27	117.672	656.73	116.969	655.51	117.223	654.24
114.588	642.56	114.378	638.43	114.558	642.36	114.542	639.33
111.992	628.36	112.212	626.38	111.747	626.96	112.893	630.19
108.997	611.92	109.473	611.15	109.177	612.86	109.526	611.47
106.920	600.55	106.982	597.31	107.224	602.19	106.934	597.05
104.253	585.86	104.511	583.56	104.628	587.88	104.879	585.6
101.659	571.58	102.803	574.11	101.587	571.11	101.882	568.93
99.695	560.75	100.461	561.09	99.840	561.5	100.038	558.74
94.653	532.92	94.924	530.24	94.579	532.47	94.616	528.47
89.080	502.00	89.611	500.59	89.397	503.75	89.366	499.23

Appendix E

ANALYTICAL MODELS FOR VACUUM

CALCULATIONS

There are two sources of residual gas in SIR: the gas flow from the ion source and outgassing from the vacuum chamber. We present an analytical model used for calculation of the gas flow from the ion source in the first section of the appendix. In the second section, we calculate pressure in the ring due to outgassing from walls of the vacuum chamber.

E.1 Gas flow from the ion source

Figure E.1 shows a lumped-element model equivalent to the system shown in Figure 4.31. C1 is the conductance of the hole in the plasma electrode

$$C1 = \frac{v\,A}{4} \tag{E.1}$$

where A is the area of the hole and v is thermal velocity of gas atoms or molecules.

Conductance C21 includes the pipe (570 mm, Ø6") from the ion source to the analyzing magnet and the rectangular aluminum pipe in the magnet. To calculate

conductance of the circular piece we used the empirical formula devised by Clausing

$$C_{pipe} = R\left(\frac{L}{D}\right) \cdot \frac{v\,A}{4} \tag{E.2}$$

where $R(L/D)$ is a dimensionless coefficient that depends on a ratio of the pipe length and diameter. The coefficient, tabulated as a function of L/D, can be found, for example, in [30]. The formula correctly takes into account effects related to finite length of circular pipes. To calculate conductance of the rectangular vacuum chamber in the dipole we used the Equation E.2 for circular pipes assuming $A = ab$ where a and b are real dimensions of the rectangular pipe (L=1000 mm, a=114 mm, b=48 mm).

C22 includes the rest of the injection line and the piece that connects the straight section of the injection line and the ring (L=1062 mm, Ø6" and L=410 mm, Ø47.8 mm respectively). The conductance of the piece of the injection line from the emittance measurement box to the piece that goes down to the ring was multiplied by 0.5 to include the effect of the electrostatic triplet.

C3 is the conductance of the vacuum chamber of the ring, from the injection section to the extraction section. In estimating C3, we have not included the straight sections assuming their conductance is much higher than the conductance of aluminum rectangular pipes in the dipoles. The empty vacuum chamber in the straight section has an area of 160x250 mm^2. This is approximately eight times as large as the area of the aluminum curved sections. The vacuum chambers in the straight sections are also shorter than the bent sections: 600 mm vs. 1000 mm. The fully assembled

vacuum chambers of the straight sections have in-vacuum hardware (quadrupoles, deflectors, supports, etc.) that reduces the conductance of the sections. Though an accurate estimate of the effect of these elements on the conductance is difficult because of the complicated shape, we expect the effect to be small. Along the straight sections, the internal elements only occupy from 1 to 15% of the vacuum chamber cross-section.

As an example, Table E.1 lists calculated values of the conductances for deuterium at the room temperature.

To find $P1$, $P2A$, $P2$, and $P3$ one has to solve the system of linear equations:

$$(P0 - P1) \cdot C1 \;=\; S1 \cdot P1 + S2 \cdot P2A + S2 \cdot P2 + P3 \cdot S3 \tag{E.3}$$

$$(P1 - P2A) \cdot C21 \;=\; S2 \cdot P2A + S2 \cdot P2 + P3 \cdot S3 \tag{E.4}$$

$$(P2A - P2) \cdot C22 \;=\; S2 \cdot P2 + P3 \cdot S3 \tag{E.5}$$

$$(P2 - P3) \cdot C3 \;=\; P3 \cdot S3 \tag{E.6}$$

The average pressure in the ring is

$$P_{av} = \frac{(P2 + P3)}{2} \tag{E.7}$$

The system was solved for hydrogen and deuterium and two diameters of the ion source hole: 1 mm and 2 mm. Results of the calculations were presented in 4.7
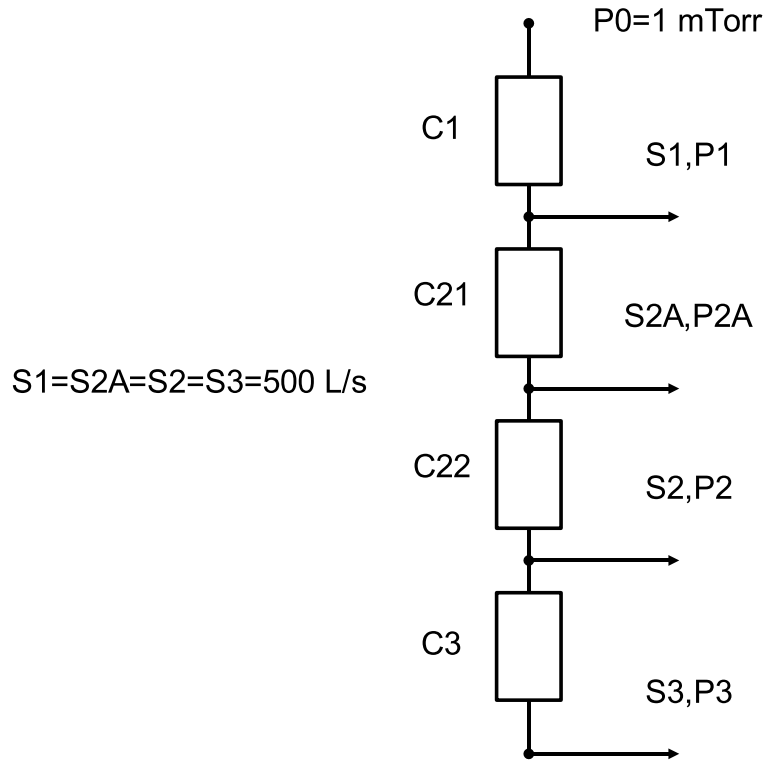
Figure E.1: Graphical representation of the analytical model of the vacuum system shown in Figure 4.31. Pi and Si correspond to pressure and pumping speed in i-th point in Figure 4.31

Table E.1: Calculated gas conductances of the injection line and the ring, given in L/sec, for deuterium at the room temperature. The conductance of the plasma electrode diaphragm (C1) was calculated for a Ø2 mm hole.

C1	1.0
C21	145
C22	61
C3	162

E.2 Outgassing in the ring

In estimating the gas pressure in the ring due to outgassing, we completely neglect gas flow to/from the injection line. Because the conductance of the straight sections is much larger than the conductance of the vacuum chamber in the dipoles, outgassing from the straight sections and outgassing from the vacuum chamber in the dipoles can be considered separately. Gas pressure in the injection and extraction sections (sections with pumps) created by the gas flow from all the straight sections is

$$P_1^s = \frac{2Q}{S} \tag{E.8}$$

where Q is the flux from each straight section and S is the pumping speed, equal to 500 l/sec. Partial pressure in the straight sections without pumps due to outgassing in the straight sections is equal to

$$P_2^s = \frac{Q}{C}\left(\frac{1}{2} + 2\frac{C}{S}\right) \tag{E.9}$$

where C is the conductance of a 90° piece of the vacuum chamber in the dipoles. Details on calculation of the conductance C can be found in the first section of this appendix. The average pressure in the ring due to outgassing from the straight sections is

$$P_{av}^s = \frac{P_1^s + P_2^s}{2} \tag{E.10}$$

In estimating the gas pressure due to outgassing from the vacuum chamber in the dipoles, we used the model shown in Figure E.2. The model assumes an infinite

chain of equidistantly separated pumps connected by a rectangular pipe of an area of 114x48 mm^2. The separation between the pumps is equal to the double length of the 90° section of the vacuum chamber in the dipole magnets.
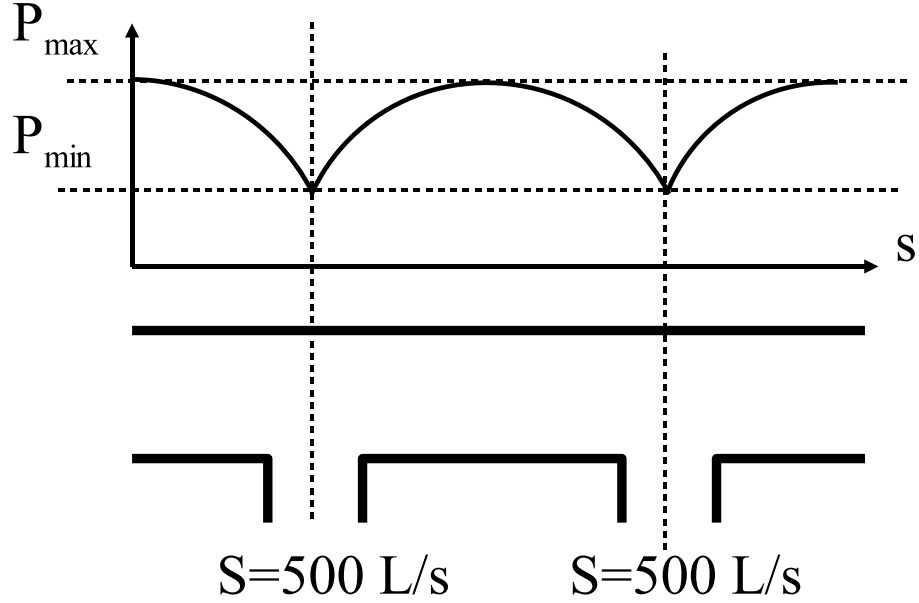
Figure E.2: In calculating pressure due to outgassing in the ring, we have used an infinite chain of pumps connected by a rectangular vacuum chamber.

Pressure in the system shown in Figure E.2 is a parabolic function of the distance x from one of the pumps (solution of this standard problem can be found, for example, in [33])

$$P^b(s) = 2(a+b)q \left(\frac{Ls - s^2}{w} + \frac{L}{S} \right) \tag{E.11}$$

where a and b are the width and the height of the vacuum chamber, L is the length of the pipe between pumps, q is the outgassing rate, w is the specific molecular conductance of the rectangular pipe, and S is the pumping speed.

The average pressure in the system is

$$P_{av}^b = 2(a + b)q \left(\frac{L^2}{6w} + \frac{L}{S} \right) \qquad \text{(E.12)}$$

The model described above is mathematically identical to the vacuum chamber of SIR if we neglect the curvature of the aluminum sections in the ring dipoles. In both cases, the pressure distribution is described by the formulas

$$Q(s) = w\frac{dP}{ds}$$
$$\frac{dQ(x)}{dx} = 2(a + b)q \qquad \text{(E.13)}$$

when combined these two equations yield the equation

$$w\frac{d^2 P}{dx^2} = -2(a + b)q \qquad \text{(E.14)}$$

The solution of the last equation is a parabola. All three parameters that define the parabola have to be the same in both cases for the systems to be identical. The coefficient in front of x^2 is the same in both cases: $2(a+b)q/w$. The maximum of the pressure distribution is in the middle point between the pumps in both cases. Thus, the second coefficient is also the same. The third coefficient is just a constant. It is the pressure at the location of the pumps. This pressure is equal to the gas flux outgassed from the wall divided by the pumping speed of the pumps: $2(a + b)/S$. This number is the same in both cases too. Thus, we can conclude that the infinite system of pumps is mathematically identical to the vacuum chamber of our ring. We neglected the curvature of the SIR vacuum chamber.

Assuming $q = 1.0 \cdot 10^{-9}$ (Torr l s^{-1} cm^{-2}) and using SIR values in Equations E.8, E.9, E.10, and E.12, one can easily calculate pressure of water vapor in SIR due

to outgassing from the walls of the vacuum chamber

$$P_{av} = P_{av}^s + P_{av}^b = 1.6 \cdot 10^{-8} + 3.9 \cdot 10^{-8} = 5.5 \cdot 10^{-8} \text{ Torr} \qquad \text{(E.15)}$$

BIBLIOGRAPHY

[1] S.Adam, 14th Int. Cycl. Conf. (Cape Town, 1995), p.446, World Scientific, Singapore.

[2] Th. Stammbach et al., "The 0.9 MW Proton Beam at PSI and Studies on a 10 MW Cyclotron", Proc. 2nd Int. Conf. on Accelerator-Driven Transmutation Technologies, Kalmar 1996, p.1013

[3] Y. Alenitsky et al., "The High Current Cyclotron Complex for an Electro-nuclear Way of Production of Energy", Proc. 16th Int. Conf. on Cyclotrons and Their Applications, East Lansing 2001, p.434

[4] G.Kim, D. May, P. McIntyre, A. Sattarov, "A Superconducting Isochronous Cyclotron Stack as a Driver for a Thorium-Cycle Power Reactor", Proc. 16th Int. Conf. on Cyclotrons and Their Applications, East Lansing 2001, p.437

[5] T. Welton, "Sector focused Cyclotrons", Nucl. Sci. Ser. Report No. 26, NAS-NRC-656, (192, Washington D.C., 1959)

[6] M.Gordon, 5th Int. Cycl. Conf. (Oxford, 1969), p.305, Butterworth, London.

[7] W.Joho, 9th Int. Cycl. Conf. (Caen, 1981), p.337, Les editions de physique, Les Ulis Sedex.

[8] Th. Stammbach, "Experience with the high current operation of the PSI cyclotron facility", Proc. 13th Int. Cycl. Conf. (Vancouver 1992)

[9] E. Pozdeyev, "A fast code for simulation of the longitudinal space charge effect in the isochronous cyclotrons", 16th Int. Cycl. Conf. (East Lansing, 2001), p.411, AIP Conference Proceedings V. 600, Melville, New York

[10] R.Mueller and R.Mahrt, Nucl. Inst. Meth., 86, 241, (1971)

[11] W.Joho, Particle Accelerators, V.6, 41, (1974)

[12] M.Gordon, 10th Int. Cycl. Conf. (East Lansing, 1984), 279, IEEE 84CH1996-3, New York

[13] R.Hockney, J.Eastwood, "Computer Simulations Using Particles", Adam Hilger, Bristol, 1988

[14] E.Pozdeyev, Proc. of PAC2001 (Chicago), p.3549

[15] E. Pozdeyev, R. Fontus, D. Lawton, F. Marti, J. Rodriguez, D. Sanderson, R. York, A. Zeller, R. Zink, "Progress Report on the Small Isochronous Ring Project at NSCL", Proc. of PAC 2003 (Portland)

[16] P. O'Shea, "The University of Maryland Electron Ring," Procs. of PAC2001 (Chicago), p. 159

[17] SPIRALGAP, NSCL, MSU, East Lansing, USA

[18] M. Gordon, "Effects of spiral electric gaps in superconducting cyclotrons", NIM A, Elsevier (Holland), Volume 169, Issue 3 , 1980, p. 327-336

[19] M.Reiser, "Theory and design of charged particle beams", John Wiley and Sons, Inc., New York (1994).

[20] W.Press, S.Teukolsky, W.Vetterling, B.Flannery, "Numerical Recipes in C", Cambridge University Press, (1992).

[21] S. Gradshteyn and I. M. Ryzhik, "Table of Integrals, Series and Products", 5th ed., Academic Press, San Diego, 1994.

[22] R.V.Servranckx, et. al. "User's Guide to the Program DIMAD", SLAC Report 285 UC-28 (May 1985).

[23] Users Guide for the POISSON/SUPERFISH Group of Codes, LA-UR-87-115, Los Alamos Accelerator Code Group, Copyright 1998, by the University of California.

[24] TOSCA, Vector Fields Inc., England

[25] GENSPEO, NSCL, MSU, East Lansing, USA

[26] J.A. Rodriguez' dissertation, in progress.

[27] E. Pozdeyev, F. Marti, J. Rodriguez, R. York, "Small Isochronous Ring Project at NSCL", Proc. of EPAC 2002 (Paris), p. 1395-1397.

[28] J. Rodriguez, E. Pozdeyev, F. Marti, "Injection Line of the Small Isochronous Ring", Proc. of EPAC 2002 (Paris), p. 1401-1403.

[29] SIMION, BECHTEL BWXT IDAHO, LLC. For contact information visit http://www.inel.gov/env-energyscience/chemistry/simion-software.shtml

[30] J. F. O'Hanlon, "A user's guide to vacuum technology", John Wiley & Sons, Inc., 1980

[31] J.H. Moore, C.C. Davis, M.A. Coplan, "Building scientific apparatus", Second edition, Perseus Book Publishing, L.L.C., 1991

[32] H. Tawara, "Cross sections for charge transfer of hydrogen beams in gases and vapors in the energy range 10 eV - 10 keV", Atomic Data and Nuclear Data Tables, V. 22, 491 (1978)

[33] O. Grobner, "Vacuum systems", CERN Genral Accelerator School, (Gif-sur-Yvette, Paris, Farnce, 1984), CERN 85-19, 1985

[34] J. Rodriguez, F. Marti, E. Pozdeyev, "Initial Experimental Results of the Small Isochronous Ring (SIR)" Proc. of PAC 2003 (Portland)

[35] MATHCAD, Mathsoft Engineering & Education, Inc. 101 Main Street Cambridge, MA 02142-1521